Corso di Laurea Magistrale in Ingegneria Energetica e Nucleare

Master Degree Thesis

Experimental study and model validation of Li-Ion battery nail penetration test

Supervisor
prof. Papurello Davide

Candidate
Beatrice Braghiroli

Luglio 2023

Abstract

Lithium Ion Battery (LIB) are widely used in our everyday life due to their higher operating voltage, specific energy (in terms of weight and volume) and longer life with respect to other battery types. However, safety concerns have arisen and, as their usage is still expected to grow in the next years, research has focused on finding strategies to improve their safety. Thermal Runaway (TR) is the worst event that can happen to a battery as consequence of mechanical, electrical or thermal abuse. TR consists of a chain of exothermic chemical reactions that increases the battery temperature and can lead to fire ignition and explosion of the battery itself. Herein, the state-of-the-art battery structure and materials are presented, along with recent advances related to the prevention and suppression of the occurrence of TR .

To better understand the battery response to abuse, different tests can be carried out. This thesis focuses on the nail penetration test, both experimentally and through modelling. Nail penetration tests have been performed on two different 18650 cylindrical batteries using the Accelerating Rate Calorimeter (ARC) provided with the Nail Penetration and Crush Option (NPCO). As the experiments can be costly and time consuming, a model will be developed to predict the thermal behaviour of a LIB after nail penetration test. The experiments are then used to validate the model.

Overall, the aim of this thesis is to contribute to the ongoing effort to improve the safety of LIB and ensure their growth and adoption in various application.

Contents

List of Figures

List of Tables

Acronyms

ARC Accelerating Rate Calorimeter ii, 48–52, 81

BEV Battery Electric Vehicle 22, 23, 83

BMS Battery Management System 25, 40

DEC Diethyl Carbonate 12

DMC Dimethyl Carbonate 12

EC Ethylene Carbonate 12

EDS Energy-Dispersive X-ray Spectroscopy 43

EMC Ethyl Methyl Carbonate 12

EV Electric Vehicle 1, 2, 5, 9–11, 27, 83

GNL General Non-Linear 37

GPE Gel Polymer Electrolyte 13, 14

ICE Internal Combustion Engine 1, 22

ICP-AES Inductively Coupled Plasma Atomic Emission Spectroscopy 43

IL Ionic Liquid 13

ISC Internal Short Circuit vi, 20, 24, 28, 31, 33, 34, 51, 52, 74

KMC Kinetic Monte Carlo 39

LCO Lithium Cobalt Oxide 8, 9

LFP Lithium Iron Phosphate 8, 9, 28, 30

LIB Lithium Ion Battery ii, vi, ix, 1–3, 5, 7, 8, 11–13, 15–18, 20, 23, 25, 26, 31, 39, 83

List of Symbols

Symbol	Unit	Description	Page List
α	-	Charge transfer coeffiecient	63
α_r	-	Degree of conversion	66, 77
η	V	Surface over potential	63, 64
ϕ_l	V	Liquid phase potential	59, 62–64, 71
$\phi_{s,i}$	V	Electrode potential	59, 61–64, 71
ρ_i	$\mathrm{kg\,m^{-3}}$	Density	64, 74–76
σ_i	$\mathrm{S\,m^{-1}}$	Electric conductivity	71
$\sigma_{s,i,eff}$	$\mathrm{S\,m^{-1}}$	Effective conductivity	61, 62
σ_l	$\mathrm{S\,m^{-1}}$	Electrolyte conductivity	62
$\varepsilon_{b,i}$	-	Binder phase volume fraction	70
$\varepsilon_{l,i}$	-	Electrolyte porosity (liquid phase volume fraction)	61, 70, 71
$\varepsilon_{s,i}$	-	Solid phase volume fraction	60–62, 70, 71
$c_{p,i}$	$\mathrm{J\,kg^{-1}\,K^{-1}}$	Heat capacity at constant pressure	64, 74, 76
A	$\mathrm{s^{-1}}$	Frequency factor of the reaction	65, 66, 77
A_{cell}	$\mathrm{m^2}$	Plate area	62
$a_{s,i}$	$\mathrm{m^2\,m^{-3}}$	Surcace area per unit volume	60, 63
c^*	-	Normalized reactant concentration	65, 66, 77

Symbol	Unit	Description	Page List
c_l	$\mathrm{mol\,m^{-3}}$	Concentration electrolyte	59, 61–63, 71
$c_{s,i}$	$\mathrm{mol\,m^{-3}}$	Concentration of solid particles	59, 60, 63, 64
$c_{s,i,max}$	$\mathrm{mol\,m^{-3}}$	Concentration of solid particles	63
$D_{l,eff}$	$\mathrm{m^2\,s^{-1}}$	Effective electrolyte diffusivity	61
$D_{s,i}$	$\mathrm{m^2\,s^{-1}}$	Solid phase diffusion coefficient	60
E	$\mathrm{J\,mol^{-1}}$	Activation energy	65, 66, 77
E_{eq}	V	Electrode equilibrium potential	63, 64
f_i	-	Mean molar activity coefficient	62, 63
H	$\mathrm{J\,kg^{-1}}$	Specific energy realeased by the reaction i	65, 66, 77
i_0	$\mathrm{A\,m^{-2}}$	Exchange current density	63, 71
i_{app}	A	Total applied current	62
i_l	$\mathrm{A\,m^{-2}}$	Current density in the liquid phase	60, 62, 64
i_s	$\mathrm{A\,m^{-2}}$	Current density in the solid phase	63, 64
j_i	$\mathrm{mol\,m^{-2}\,s^{-1}}$	Pore wall mass flux	60, 64
j^{Li}	$\mathrm{A\,m^{-3}}$	Reaction current	60, 61, 63, 64
k_i	$\mathrm{W\,m^{-2}\,K^{-1}}$	Heat transfer coefficient	64, 74, 76
L_{cell}	m	Total cell thickness (given by the sum of the different component)	61, 62, 69, 76, 78, 79
L_{neg}	m	Negative electrode thickness	62, 69
$L_{neg,cc}$	m	Negative current collector thickness	61, 62, 69
L_{pos}	m	Positive electrode thickness	62, 69
L_i	m	Thickness of the component i	76
$L_{pos,cc}$	m	Positive current collector thickness	61, 62, 69
L_{sep}	m	Separator thickness	69
q_{irrev}	$\mathrm{W\,m^{-3}}$	Reaction heat generation rate, irreversible component	64
q_j	$\mathrm{W\,m^{-3}}$	Joule heat	64
q_{mix}	$\mathrm{W\,m^{-3}}$	Heat of mixing	64

Symbol	Unit	Description	Page List
q_{react}	$\mathrm{W\,m^{-3}}$	Reaction heat generation rate	64
q_{rev}	$\mathrm{W\,m^{-3}}$	Reaction heat generation rate, reversible component	64
R	$\mathrm{s^{-1}}$	Reaction rate of the i reaction	65, 66
$r_{p,i}$	m	Particle Radius	60, 71
t_+	-	Transference number of Li^+	61, 62
W	$\mathrm{kg\,m^{-3}}$	Volume-specific active material content	65, 66, 77
z	-	Dimensionless measure of the SEI layer thickness	65, 66, 77

Chapter 1

Introduction

Lithium Ion Batteries (LIBs) have become one of the most popular energy storage technologies in recent years, powering a wide range of devices and applications, from Portable Electronic Devices (PEDs) to Electric Vehicles (EVs). In addition to this two applications, Power Supply Systems (PSSs) are expected to drive the market growth in the near future. Even though these are the three main application LIBs are also used in other application such as aerospace, medical devices, and many more.

PEDs include numerous devices that are of common use in our everyday life such as phones, laptops, tablets, gaming consoles and toys among others. The market for PEDs has been the primary one for decades, and it is still expected to grow as more devices became available (such as smartwatches and smart glasses) [1], and as smartphone penetration continues to grow in different part of the world [2]. In fact, as emerging economies continue to develop, technology use is likely to grow. A key aspect in the growth of the market of LIBs for PEDs has been the aim to increase the specific energy in order to achieve progressively smaller and lighter devices. Additionally, consumers have been demanding shorter charging times and longer battery life, further driving the market growth.

EVs are defined, according to the Standard IEC 61851-1 [3], as "any vehicle propelled by an electric motor drawing current from a rechargeable storage device, intended primarily for use on public roads" and the main rechargeable storage systems taken into account are LIBs. The market increase is linked to the ongoing clean energy transition. In fact, with the possibility of using renewable energy to charge EVs, even locally, and the zero emissions during operation, EVs are seen as a viable way to substitute conventional Internal Combustion Engine (ICE) vehicles. Moreover, EVs are characterized by up to four times higher energy efficiency than ICE vehicles [4], which is also possible to further increase by using regenerative braking.

Finally, the use of stationary PSSs is emerging, both off-grid and grid-connected. When it comes to off-grid systems, the aim is to couple the battery with Renewable

Energy Sources (RESs) so that when power generation is lower than user demand, it is possible to store it and use it when needed. The purpose is to meet the demand and to be self-sufficient. For grid-connected systems, the same concept applies, but with the added option of utilizing energy from the grid in order to meet the demand. Another stationary application consists of grid stabilisation. In fact, RESs production is not constant as it is inherently dependent on environmental conditions. Energy storage integration is essential as a direct connection to the grid can cause instability or even failure of the utility network. Despite that, this last end-use is expected to remain marginal in most markets until 2030 [5].

An overview of the market share (expressed in GWh/y) of the different applications in the past and the predictions for the future is reported in Table 1.1. As it is possible to see PEDs where the only application driving the market in 2010 and before, but are now surpassed by the EVs sector. Moreover, the PSS application is still untapped and the demand is expected to nearly triple every five years. As a result, the fast-growing market is driving the total global demand growth to roughly double every five years [6].

Table 1.1. Market share in GWh/y in different years (past, present and future) [6]

	2010	2015	2020	2025	2030
PEDs	21	31	45	66	100
EVs	0	13	76	137	245
PSSs	0	0	2	10	30
Other applications	1	1	2	7	15
Total	22	45	125	220	390

Along with the high demand increase, there have been a relevant decrease in prices. However, a trend reversal happened for the first time in 2022, with a 7% rise with respect to the previous year that leads to a price of 151 $/kWh [7]. This increase was caused by the rising prices of raw materials and the soaring inflation. Almost the same price is expected in 2023.

As the use of batteries has increased, a greater demand has been placed on their safety and management. Whether the application, safety of batteries is of paramount importance to manufacturers and integrators, especially in the event of external mechanical stress or Thermal Runaway (TR). Abuse testing is a crucial aspect of LIBs safety and reliability, as it helps to understand battery failure mechanism, identify potential hazards and improve safety measures. Abuse tests are divided into mechanical, electrical and thermal. Among different abuse tests, nail penetration one is a common mechanical test that consist in the penetration of the battery by means of a sharp object, the nail. The consequence of the test is a mechanically induced short circuit. This test provides valuable information on the thermal and

electrical behaviour of the battery under mechanical stress, as well as its thermal stability and potential for TR. To reduce the number of experimental tests, as they are destructive and that can be expensive, it is important to model the abuse process. Moreover this can help in developing a predictive capability for battery TR response to mechanical insult and to, as a consequence, develop prevention and mitigation approaches to ensure the safety of the battery system.

For the reasons stated above, this thesis will first analyse LIBs literature in general in Part I, investigating the literature in terms of materials and the future perspective (2). Moreover, focus is placed on safety issues, mainly related to mechanical abuse and testing, with emphasis on nail penetration test in Chapter 3. The literature review is concluded with an analysis on the battery models (Chapter 4).

Then, the experimental part II related to the nail test will be reported and modelled in Part III.

Part I

Literature Review

Chapter 2

Lithium Ion Batteries

A battery is an electrochemical device that stores energy in a chemical form and releases it on command in the form of electricity, undergoing spontaneous reactions. Batteries are composed by multiple electrochemical cells connected in series and/or in parallel to provide the required voltage and capacity respectively. Each cell is composed of a positive and a negative electrode separated by an electrolyte, usually a solution containing dissociated salts to allow ion transfer between the two electrodes. Once the electrodes are connected externally, the chemical reaction proceeds, liberating electrons and providing current to the user.

There are four main types of rechargeable batteries:

1. Lead-acid

2. Nickel-Cadmium (Ni-Cd)

3. Nickel-Metal Hydride (Ni-MH)

4. Lithium-Ion (Li-Ion)

The key characteristics of these four types of batteries are compared in graphically in Figure 2.1 on the next page, from which it is possible to evidence that Lithium Ion Battery (LIB) technology is characterized by higher operating voltage, cycle life and speed of charge while having a relatively low self-discharge. However, the characteristic that has attracted the most interest since Sony's introduction to the market in 1991, is the high energy density, both in term of volume and weight, when compared with existing rechargeable batteries as presented in Figure 2.2 on the following page. Due to this, LIBs are the most used technology in Portable Electronic Devices (PEDs) and for Electric Vehicles (EVs) where weight and volume are very relevant. In the case of renewable storage, however, implementing a LIB may mostly be seen under the angle of gain in lifespan as storage space may not be a challenge.
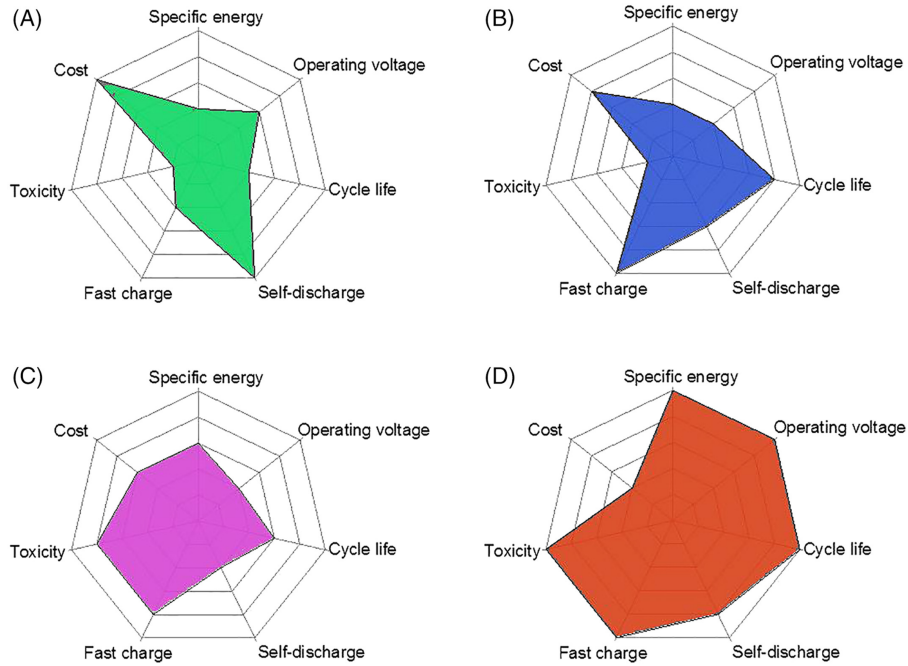
Figure 2.1. Main performance parameter comparison for A) Lead-acid, B) Nickel–Cadmium, C) Nickel-Metal Hydride, and D) Lithium Ion Batteries [1]
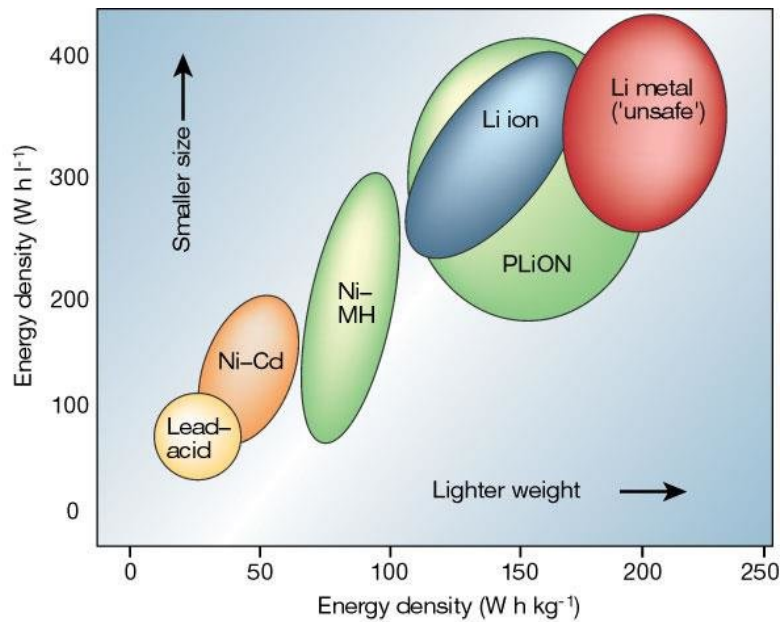
Figure 2.2. Comparison of the different battery technologies in terms of gravimetric and volumetric energy density, on the abscissa and ordinate respectively [8]

6

2.1 Li-ion batteries working principle

The electrochemical reactions in LIBs are based on the intercalation and deintercalation of lithium ions, i.e., the insertion and removal of lithium ions within the crystal structure of the electrodes. In particular, lithium ions move from the anode (negative electrode) to the cathode (positive electrode) during the discharge process and come back during the charge process, as represented in Figure 2.3. It is important to remark that the anode (negative electrode) is the reductant, which means that it looses electrons while the cathode (positive electrode) is the oxidant, so it receives the electrons. This represent reality only during the discharge phase as during the charging process the positive electrode works as anode and the negative one works as cathode. However, it is common use to refer at the electrodes with the name they have during discharge phase even if it can be misleading. This originates from lithium primary battery nomenclature as they are not rechargeable (and so characterised only by a discharging process).
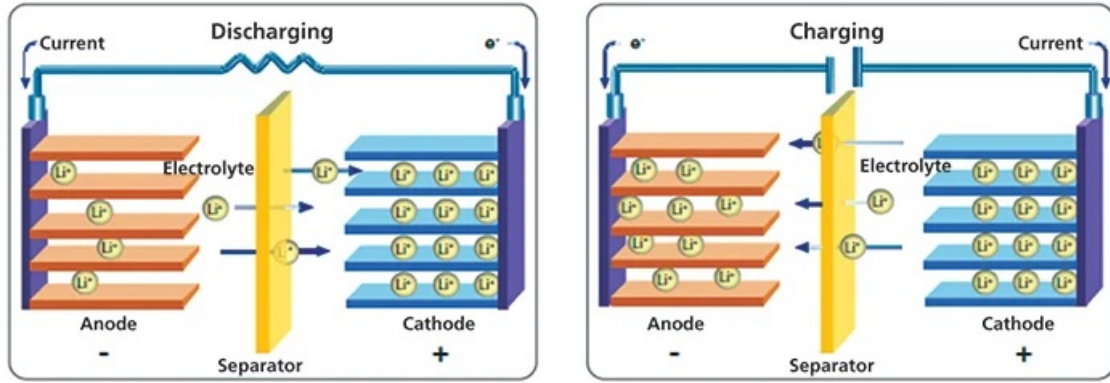
Figure 2.3. Schematic illustration of LIB during charge and discharge [9]

The reaction happening at the negative electrode is the following:

$$\text{Li}_x\text{C} \xrightleftharpoons[\text{charge}]{\text{discharge}} \text{C} + x\text{Li}^+ + x\text{e}^- \tag{2.1}$$
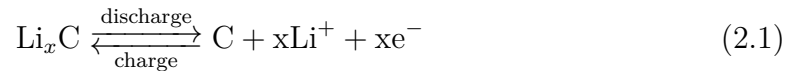
while the reaction happening at the cathode is:

$$\text{Li}_{1-x}\text{MO}_2 + x\text{Li}^+ + x\text{e}^- \xrightleftharpoons[\text{charge}]{\text{discharge}} \text{LiMO}_2 \tag{2.2}$$
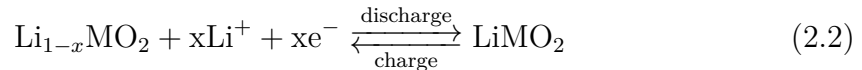
where with M it is denoted a metal. The overall reaction is:

$$\text{Li}_x\text{C} + \text{Li}_{1-x}\text{MO}_2 \xrightleftharpoons[\text{charge}]{\text{discharge}} \text{LiMO}_2 + \text{C} \tag{2.3}$$

2.2 Materials

The main components of a LIB cell are the cathode, anode, electrolyte, separator and current collector. They influence the overall performance of the battery: in particular, anode material is responsible of the capacity of the battery, while cathode one is responsible of the potential difference as represented in Figure 2.4. The materials of LIB components are analysed in the following sections.
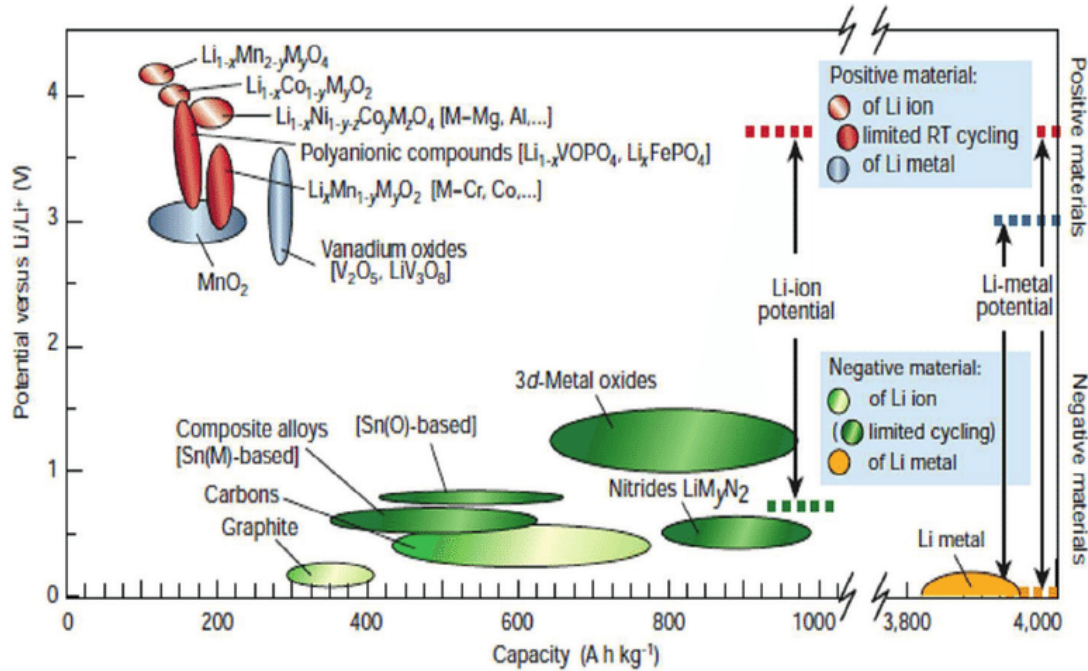
Figure 2.4. Potential vs. Capacity for typical or under development LIBs anodes and cathode materials [10]

2.2.1 Cathode

The typical cathode is a lithium metal oxide compound in the form of powders, the most known are: Lithium Cobalt Oxide (LCO), Lithium Manganese Oxide (LMO), Lithium Iron Phosphate (LFP), Nickel Cobalt Aluminium Oxide (NCA) and Nickel Manganese Cobalt Oxide (NMC). Using a different material means different battery characteristics that are summarised in Table 2.1 on the next page.

LCO was the first material implemented by Sony when LIBs where first commercialised, for this reason it is a very mature technology [6] and the market share in the meantime has stabilized [11]. However, due to the presence of cobalt, it is quite costly (resource scarcity) and not sustainable (high toxicity) [14]. Beside that, LCO is characterised by high specific energy and a cycle life of few years [6]. The

Table 2.1. Comparison of the different cathode materials. Data taken from [6, 11, 12, 13]

	LCO	LMO	LFP	NCA	NMC
Nominal voltage (V)	3.6	3.7-3.8	3.2	3.6	3.7
Specific energy (Wh/kg)	150-200	100-150	90-140	200-250	150-220
Durability (full cycles)	500-1000	1000-2000	3000	2000+	2000+
Cost (-)	mid-high	low	low	mid	mid-high
Thermal runaway (°C)	150	250	270	150	210
Safety (-)	poor	good	excellent	poor	good
Applications (-)	PED	E-bike Power tools Medical EV	E-bike EV PSS	EV Medical	EV PED Power tools Medical

main disadvantage is the low thermal stability, that can lead to Thermal Runaway (TR) already at low temperatures [6, 11]. As a consequence, LCO batteries are a common choice for PEDs while the EV sector shows no interest, both because of safety issues and the limited lifecycle [6].

In order to substitute cobalt to reduce cost and intrinsic toxicity, different strategies have been followed. One of them consists in using LMO cathode. Thanks to higher thermal stability of manganese oxide, LMO batteries are inherently safer and Thermal Runaway occurs at higher temperature as reported in Table 2.1. The drawbacks are related to the lower capacity (in terms of specific energy) that leads to a limited growth potential, unless mixed with NMC [11].

Another possibility is LFP. The biggest advantage is their durability as LFP batteries last up to 3000 full cycles [13]. On the other hand, they are characterised by relatively low specific energy and the elevated self discharge [11]. The LFP battery has been used in the e-bike sector and it is expected to be used in Power Supply System (PSS), both off-grid and grid-connected [6, 13].

NCA cathodes typically use a blend of 80% nickel, 15% cobalt and 5% aluminium, and therefore the dependence on cobalt is moderate when compared with LCO batteries. NCA batteries have an outstanding specific energy as well as high specific power granting them a decent growth potential. The main problem is linked to the low temperatures leading to TR and the consequent poor safety. NCA batteries are used in EV, and there are projections for grid-connected use (e.g. backup and loadshift).

Compared to NCA, the NMC battery has lower energy density while presenting a longer cycle life. The proportions of nickel, manganese and cobalt could vary:

increasing the share of nickel favours the specific energy aspect, while increasing the share of manganese increases specific power. However, increasing Ni content turns out in structural and thermal instability. Although the NMC battery was first commercialized as late as 2004, it dominates in EV application, both hybrid and full electric, while also being used in PED, power tools and medical devices [6, 11, 13]. Being the favourite chemistry for many uses, it is the dominant cathode chemistry and the market share is increasing.

Said compounds are characterised by low conductivities and diffusion coefficients, problem that is overcame using conducting agents such as carbon based materials in form of powders (e.g., Nmethyl-2-pyrrolidone) [6]. The conventional fabrication process also uses a binder (e.g., Poly Vinylidene Flouride) to shape the cathode as it is possible to see in Figure 2.5. These additives don't contribute directly to the capacity of the battery, but they increase the weight of it and so compensate partially the increase of energy density provided. For this reason, research is focused in developing free-binder cathodes [15].
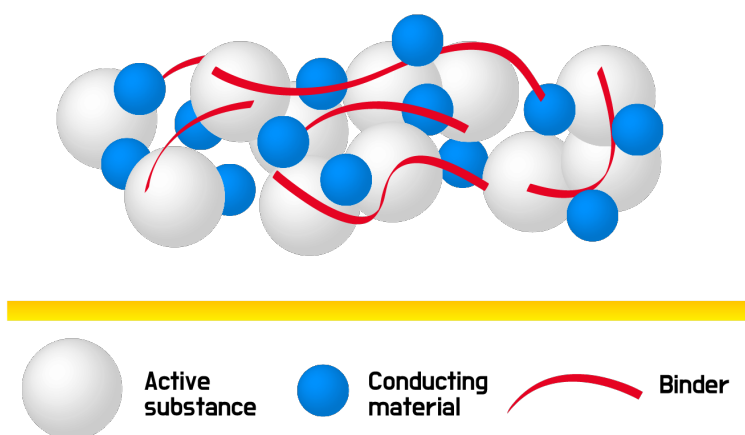
Figure 2.5.   Conventional fabrication of cathode consists of the (cathode) active material, conducting material (carbon based) and a binder [16]

2.2.2   Anode

The capacity and performance of the battery depends largely on the intrinsic characteristics of the anode material and on its morphology [17]. The actual dominant material is graphite because of the low cost, abundant availability, low delithiation potential vs Li, high Li diffusivity, high electrical conductivity, and relatively low volume change during lithiation/delithiation [14]. However, graphite based anodes are limited in achieving higher energy densities due to their low theoretical specific and volumetric capacities [18].

In order to achieve higher capacity, different lithium-metal alloys has been considered, in particular lithium-tin and lithium-silicon. One of the major issues, which has in fact so far hindered their commercialization, is the large volume change occurring during Li^+ insertion and extraction. Using silicon this volume change can be up to 400% of the original volume [19]. This problem can be addressed by using suitable nanostructures, such as nanowires, nanotubes, hollow particles, and, particularly, carbon-based, Sn-C and Si-C nanocomposites [20].

To further increase energy density, it would be necessary to use lithium metal due to its extremely high theoretical specific capacities and the lowest negative electrochemical potential [18], as it is also possible to see from Figure 2.2 on page 6 and Figure 2.4 on page 8. However, lithium metal is highly reactive leading to several unresolved issues that make such systems difficult for concrete employment. Indeed, it readily reacts with most electrolytes and, in particular, with liquid organic solutions commonly adopted in LIBs, experiencing dendritic growth upon charging with associated serious safety concerns [21]. To ensure safe operation, solid electrolytes that form a barrier to dendrite have been studied and will be analysed in the following section.

Another possibility is the use of Lithium Titanate Oxide (LTO) batteries whose characteristics are reported in Table 2.2. LTO battery offers longer cycle life at the expense of specific energy, which is lower than all other types of LIBs [13].

Table 2.2.   LTO batteries characteristics[13]

	LTO
Nominal voltage (V)	2.7
Specific energy (Wh/kg)	70
Durability (full cycles)	5000+
Cost (-)	very-high
Thermal runaway (°C)	270
Safety (-)	excellent
Applications (-)	PED EV

2.2.3 Electrolyte

The electrolyte is not an influential component on the battery performance in terms of specific capacity, power density and so on as those figures of merit depends mainly on the electrodes. However, the electrolyte is the primary responsible of the battery durability and safety. The state of the art consist in using liquid electrolytes that

are composed of three main components [22]:

- **Li$^+$ conducting salt**: The most common are $PF_6{}^-$, $BF_4{}^-$. These anions are characterised by a high radius so that the interaction due to the Coulomb force is lower and Li$^+$ ions are freer to move.

- **Organic solvent**: it must be aprotic to avoid the development of hydrogen. Suitable materials are ethers and esters, including organic carbonates. However, organic carbonates are highly flammable and they can generate highly flammable gases when LIBs are overheated with consequent safety issues [21, 23]. Cyclic carbonates, such as Ethylene Carbonate (EC) and Propylene Carbonate (PC) are commonly used for they electrochemical performances [24]. On the other hand, high viscosity and melting point hinders ion transport, so usually linear carbonates, such as Dimethyl Carbonate (DMC), Diethyl Carbonate (DEC) and Ethyl Methyl Carbonate (EMC) are mixed to the cyclic ones [24]. A summary of the state of the art organic solvents properties are reported in Table 2.3.

Table 2.3. Organic solvents properties. +, High; -, Low; o, Medium. Color code has been added: green, pro; red, cons. [24]

Solvent	EC	PC	DMC	DEC	EMC
Structure	Cyclic	Cyclic	Linear	Linear	Linear
Dielectric constant	+	+	-	-	-
Viscosity	+	+	-	-	-
Volatility	-	-	+	+	+
Boiling temperature	+	+	-	-	-
Flash point	+	+	-	-	-
Melting temperature	+	-	o	-	-
Construction to SEI	+	-	-	-	-
Anodic stability	+	+	o	o	o
Safety	+	o	-	-	-

- **Additives**: these are 1-5% in mass of the whole electrolyte formulation. They are used to achieve an increase in safety and performance. In particular, they are useful to optimize the Solid Electrolyte Interface (SEI) layer formation (thin, compact, permeable to Li ions) as the quality of the SEI greatly influences the cycling stability, service life, power, and safety of lithium-ion cells [22]. SEI layer is built during the first cycles (usually the first three) on the negative electrode, preventing the direct contact of electrode and solvent,that can lead to their degradation [22].

In order to reduce the flammability and to improve the safety of LIBs, it is possible to add flame-retardants components to delay the occurrence of fires. This can by done by substituting the common flammable organic solvents or by introducing flame retardant additives. For example, the first being studied have been organic phosphates that can be used both as non flammable solvents or additives in electrolytes. Other possibilities are fluorides-based solvents, fluorinate phosphszenes and deep eutectic solvents [25]. Moreover Ionic Liquids (ILs) are under research as replacement for the organic solvent. ILs are characterised by improved performances in terms of toxicity, thermal and electrochemical stability and flammability [26, 27].

Another option to improve safety, as already seen analysing lithium metal as anode material, is to use a Solid Electrolyte (SE). Ionic conductivity in a SE is achieved through a mechanism of lithium hopping obtained thanks to the presence of oxygen, as represented in Figure 2.6. The conductivity realised with this mechanism is lower than in the liquid.
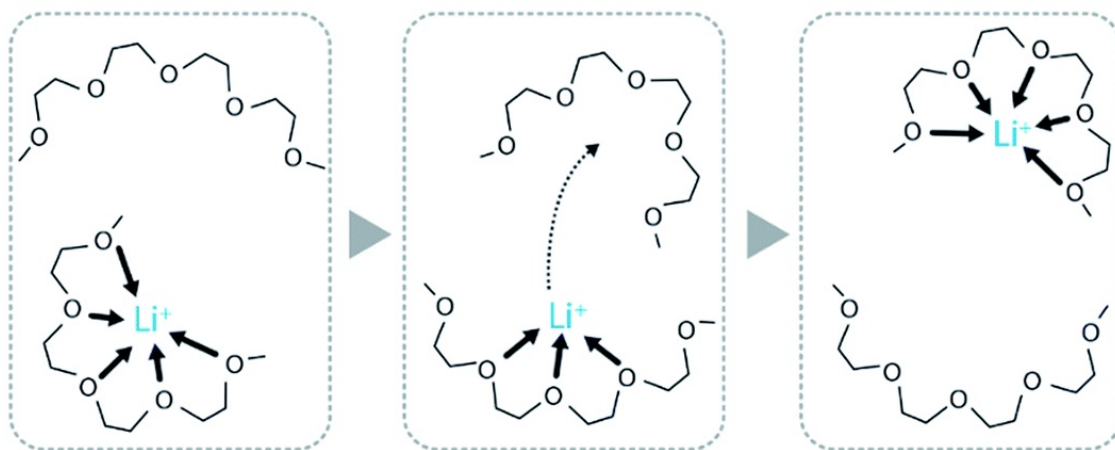
Figure 2.6.   Hopping mechanism that enhance lithium ion conductivity. Modified from [21]

Going into more detail, it is possible to divide SE into polymeric and inorganic as reported in Figure 2.7 on the next page.

Polymeric electrolytes have drawn considerable attention as a replacement for liquid electrolytes due to their intrinsic properties. They can be divided into all-solid (solvent free) Solid Polymer Electrolyte (SPE) or Gel Polymer Electrolyte (GPE) if liquid is added.

SPEs are usually made of a polymeric matrix, such as polyethylene oxide (PEO), in which lithium salts are dissolved to provide ionic conductivity [21, 23]. They are characterised by some important advantages with respect to liquid electrolytes such as intrinsic higher safety, non-volatility, free-standing flexibility, lightweight, mechanical properties and ease of fabrication [23]. Naturally, there are also disadvantages,
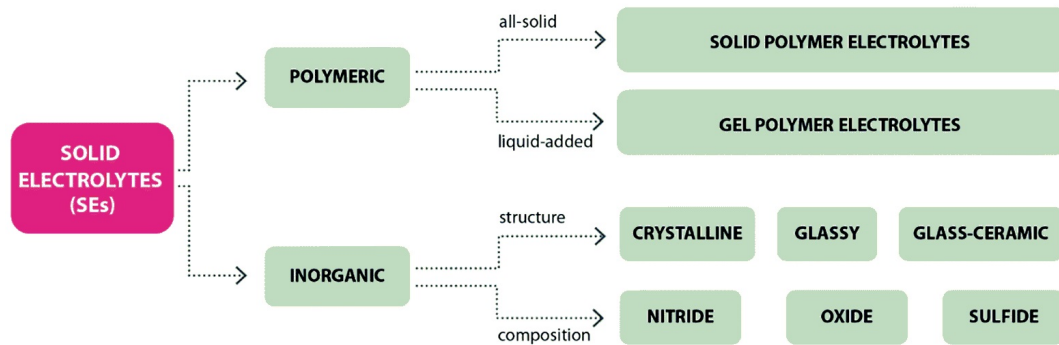
Figure 2.7. A possible classification of solid electrolytes. Image adapted from [21]

like a poor electrochemical stability, the interfacial contact electrolyte-electrode is limited on the actual area of contact and, the already mentioned, lower ionic conductivity.

A possible way to target the ionic conductivity issue, while keeping satisfactory mechanical property, relies on the addition of liquid organic solvents as in the liquid electrolytes, leading to GPE [21]. In this case the liquid part is contained in a polymeric matrix so that the risk of leakages is reduced. GPEs electrochemical properties depend on the combination of different liquid and possible added plasticiser component, while safety and mechanical properties are addressed by the polymeric matrix [23]. Also in this case it is possible to add flame retardants components, combining the already seen advantages offered with the "quasi-solid" nature of GPEs.

Finally, as seen in Figure 2.7, there is under studying the possibility of using Solid Inorganic Electrolyte (SIE), such as the one based on garnet, perovskite or sulphide among others [25] . Most SIEs are inherently non-flammable, but they often have low ionic conductivity and poor interface contact [25].

2.2.4 Separator

Battery separators are porous materials situated between the positive and negative electrodes of a battery cell. Their function is to act as physical barrier to prevent physical contact between the two electrodes and, therefore, short circuits. At the same time, they must enable ions transport within the electrolyte. To achieve this, separators are usually porous flat designs filled with an electrolyte. Separators are not directly involved in any cell reaction but they have an impact on several battery performance parameters, including cycle life, energy and power density, and safety.

There are different parameters that impact on the ability of separators to fulfil their task, such as thickness, porosity (and pore size and distribution, stability (chemical, dimensional, thermal) and many other properties [28]. The general requirements are reported in Table 2.4 on the next page.

Table 2.4. General requirements for LIB separators [28, 29]

Parameter	Requirement
Chemical and electrochemical stability	stable for a long period of time
Wettability	wet out quickly and completely
Mechanical property	$>1000 \, \mathrm{kg/cm}$
Thickness	<25 µm
Pore size	<1 µm
Porosity	40-60%
Permeability (Gurley)	$<0.025 \, \mathrm{s/µm}$
Dimensional stability	no curl up and lay flat
Thermal stability	$<5\%$ shrinkage after $60 \, \mathrm{min}$ at $90 \, °\mathrm{C}$
Shutdown	effectively done at elevated temperatures

The separators may be woven, molded, non-woven, bonded, micro porous, paper-based, or laminated types. In case of liquid electrolyte LIB, the separator is in most of the case composed by a single layer of polyolefin, such as Polyethylene (PE) or Polypropylene (PP)). The problem is their flammability and thermal instability. As for organic solvents in electrolytes, research is focused in developing flame-retardant separators. The aim is to prevent efficiently the battery TR induced by the redox reaction between the cathode and the anode [30]. They can be non-flammable polymer separators, ceramic/polymer composite separators or separators with flame retardant additives [30].

Batteries that utilize SPEs or SEs in general lack a separator [19]. However, also in this case flame retardant separators exists [30].

2.2.5 Current collectors

In order to obtain a complete cell, current collectors are necessary as they bring the current to the external circuit. The material used for anode and cathode current collector are different and in particular aluminium foil is used for the cathode and copper foil in the anode case. The current collectors influence different important performance parameters of LIBs, such as electrical conductivity, cycle stability, capacity rate, and contact and corrosion resistances [19].

2.3 Packaging formats

The battery is then made connecting in series or in parallel different cells, to increase the voltage potential and the capacity (Ah) respectively.

To complete the battery it is necessary to add a metal case in order to prevent the entry of moisture, as it would cause the hydrolysis of the conducting salt in the electrolyte into hydrogen fluoride, and to prevent the loss of solvent by means of diffusion [31]. Metal, usually aluminum or stainless steel, is used as it is the only material able to fulfil these tasks [31].

The final geometry can vary based on the specific requirements of the device they are being used in. The most common are coin, cylindrical, prismatic and pouch as represented in Figure 2.8.
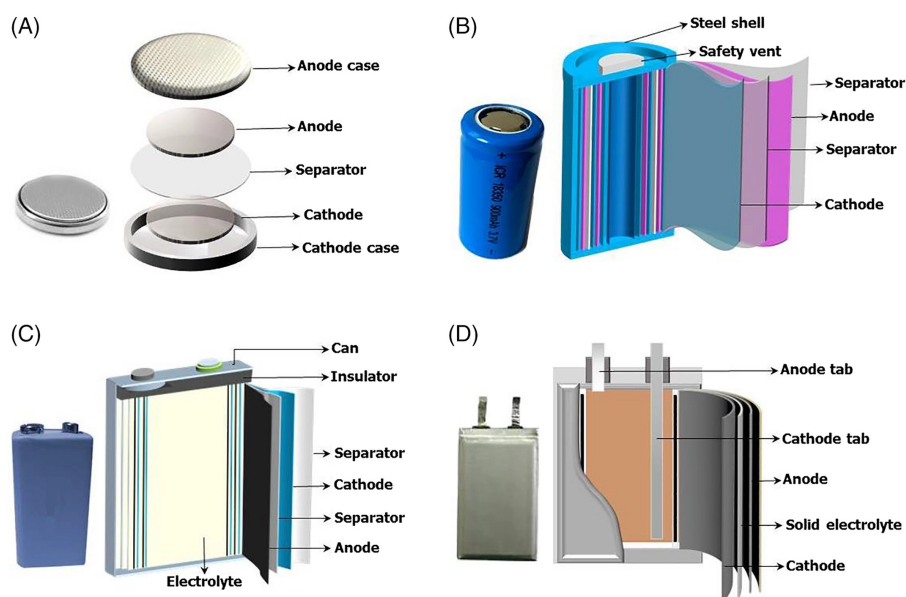
Figure 2.8.   Schematic illustration of typical rechargeable battery configurations: A, coin, B, cylindrical, C, prismatic, and D, pouch shapes [1]

Coin ones are compact cells commonly used in small devices such as calculators and hearing aids .Most of the coin cells available in the market are non-rechargeable but are used in those application because they are easy to replace and have a long shelf life.

Cylindrical LIBs are one of the most widely used packaging type. They are commonly used in small electronic devices and are known for their high energy density, long cycle life, and good performance. Cylindrical cells are made by rolling the stacked layers of anode, cathode, current collectors and separator, into a jelly roll configuration and then packing it into a solid cylindrical enclosure [32]. This also grants a good mechanical stability [32, 33]. They are also relatively easy to manufacture and cheap to produce. Among cylindrical batteries, the most common format is the 18650 which means the diameter measures 18 mm and the height 65 mm. This battery standard is quite common and used in a variety of applications, from PEDs to e-bikes. A new format, the 21700, is catching on, characterized by a

higher energy density, both in terms of weight and volume [34].

Prismatic LIB as the cil, but they have a rigid enclosure. They are available in both more compact or larger formats depending on the applications. Prismatic batteries are also relatively expensive to produce compared to cylindrical and pouch batteries, but they offer a high energy-to-weight ratio, making them ideal for applications where weight is a concern.

Pouch cells are similar to the prismatic one, but differently from the other geometries the case is soft. Pouch thin, flexible and lightweight, making them ideal for use in portable devices where space is limited. The main problem is linked to swelling due to gassing, they can grow up to 8-10% in volume over cycling [33].

Chapter 3

Safety issues and prevention strategies

3.1 Thermal runaway

Thermal Runaway (TR) is triggered by the rapid increase of temperature and pressure of a cell resulting from a series of exothermic chemical reactions, whose heat of reaction is not dispersed [35, 36]. These exothermic reactions are triggered by different types of abuse leading to temperature rise and to the decomposition of the SEI, triggering other side reactions, with possible melting of the separator, internal short-circuiting and eventually TR [19], as it is possible to see from Figure 3.1 on the next page.

During TR, all the energy stored in the battery is rapidly released, which means the more energy stored, the more energetic the reactions will be [35]. The consequence is that the battery may explode and catch fire. The severity of the TR event can depend on the State Of Charge (SOC), charging/discharging rate, the ambient environmental temperature, the electrochemical design of the cell (cell chemistry) and the mechanical one (cell size, electrolyte volume, etc.) [37].

TR can be caused by poor design and manufacturing defect, but mainly by three different types of abuse, electrical, mechanical and thermal, better represented in Figure 3.2 on the following page.

Going into more detail:

- **Thermal abuse**: LIBs are generally allowed to operate within a specific temperature range, if the temperature of the battery exceeds these limit values, several side reactions occur, initiating additional exothermic reactions, finally resulting into TR.

- **Electrical abuse**: there are different ways to electrically abuse LIBs, the most common are:
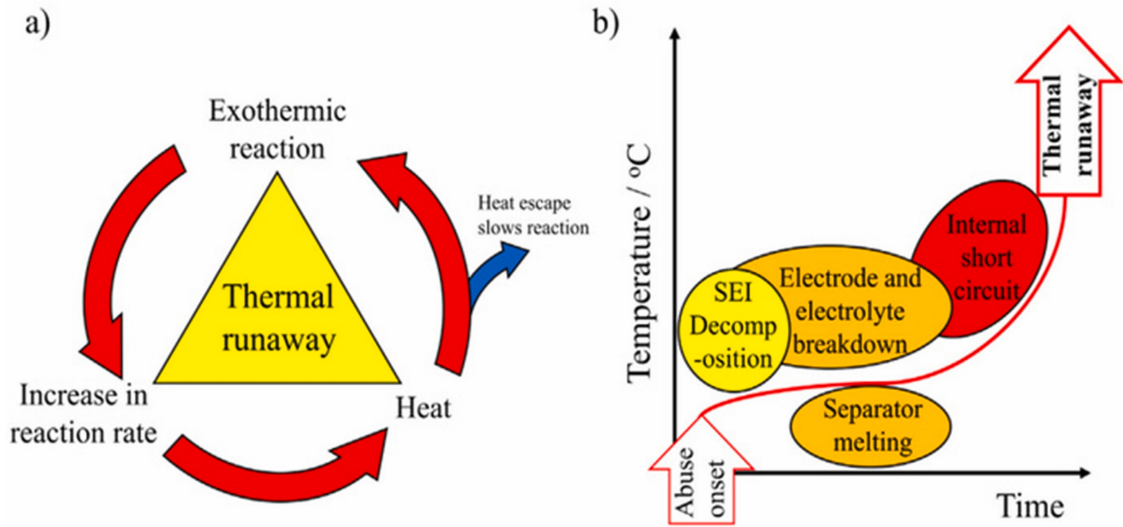
Figure 3.1.   Schematic representation of thermal runaway process [19]
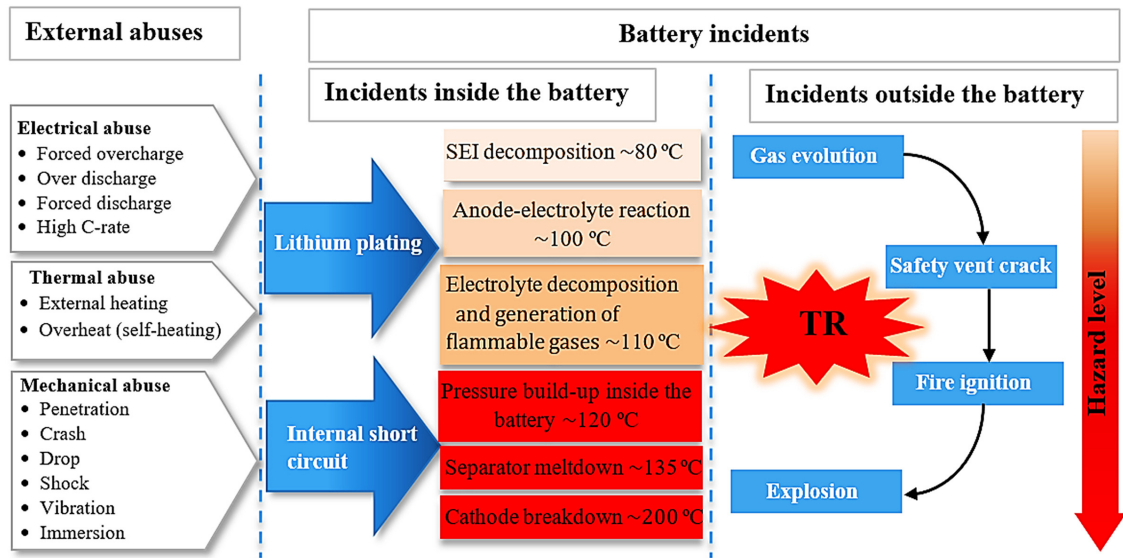
Figure 3.2.   TR mechanism [38]

– Overcharging: it can be caused by exposing the cell to too high voltage, too high current density (locally) or due to design/manufacturing defects [35]. The consequences it can cause degradation of the electrodes, in particular anode plating can happen and cause dendrite formation [35, 36].

– External short circuit: due to high rate charging/discharging it is possible to cause resistive heating within cells at points of high impedance.

19

- **Mechanical abuse**: it consists in any mechanical damage to the battery due to external action (impact, fall, penetration, etc.). If the separator breaks, contact forms between the anode and cathode electrodes, resulting in an Internal Short Circuit (ISC).

As it is possible to se from Figure 3.1 on the previous page and Figure 3.2 on the preceding page, after abuse different reactions happen inside the battery. Firstly, the decomposition of the SEI layer that starts at around $80\,°C$, or lower for some electrolytes [38]. The SEI decomposition can be modelled through the following Arrhenius equation when the temperature is higher than the onset temperature of the SEI decomposition ($T > T_{onset,SEI}$) [39]:

$$\frac{dc^d_{SEI}}{dt} = A_{SEI} \cdot c_{SEI} \cdot exp\left(-\frac{E_{a,SEI}}{RT}\right)$$

where c_{SEI} is the normalised concentration of SEI, A_{SEI} is the pre-exponential factor, $E_{a,SEI}$ is the activation energy and R is the ideal gas constant. This is followed by the anode-electrolyte reaction around $100\,°C$. In fact, as the SEI layer has been the composed, the anode and the electrolyte came in contact, causing an exothermal reaction further increasing the temperature in the battery. In particular, the lithium embedded in the negative electrode reacts with the organic solvent in the electrolyte to release combustible gas and heat, further affecting the temperature. At this point, the separator melts and exothermic reactions starts to happen at the cathode. Eventually, due to the exothermic reaction and the resulting gas pressure, the temperature rises rapidly, turning the battery into a pressure vessel [38]. Therefore, battery rupture, fire and explosion are inevitable if the pressure and gas are not properly released.

3.1.1 Gas evolution and release

Once a LIB experiences the critical event of TR, caused by one or a combination sources of abuse previously seen, different fire hazards begin to develop. One of the most relevant is the formation of toxic and flammable materials, that needs to be released to prevent the explosion of the battery [19]. In order to release properly the gas produced during TR event, different safety devices are installed in the battery, some of them will be analysed in the following sections.

Going into more detail, a combination of organic and inorganic gaseous products, such as CO, CO_2, CH_4, C_2H_4, C_2H_6, C_2H_5F, H_2 and hydrogen fluoride (HF) can be produced and contribute significantly in a fire event [40]. Even if correctly released, those gases are significantly flammable and can ignite due to the high temperature reached during TR event. Ignition of these gases within their range of flammability may result in fire and explosion scenarios, posing significant risk to surrounding life and property.

The challenge is that the species concentration of each gas is not equal for all chemistries and is impacted by several physical, electrical, chemical properties and by ambient conditions. Baird et al. [40] analysed different literature studies considering different chemistries, SOC and tests. Comparing the gas concentrations in each of them as reported in Figure 3.3, it is clear the gas mixture is influenced by the battery chemistry and by the SOC of the battery tested.
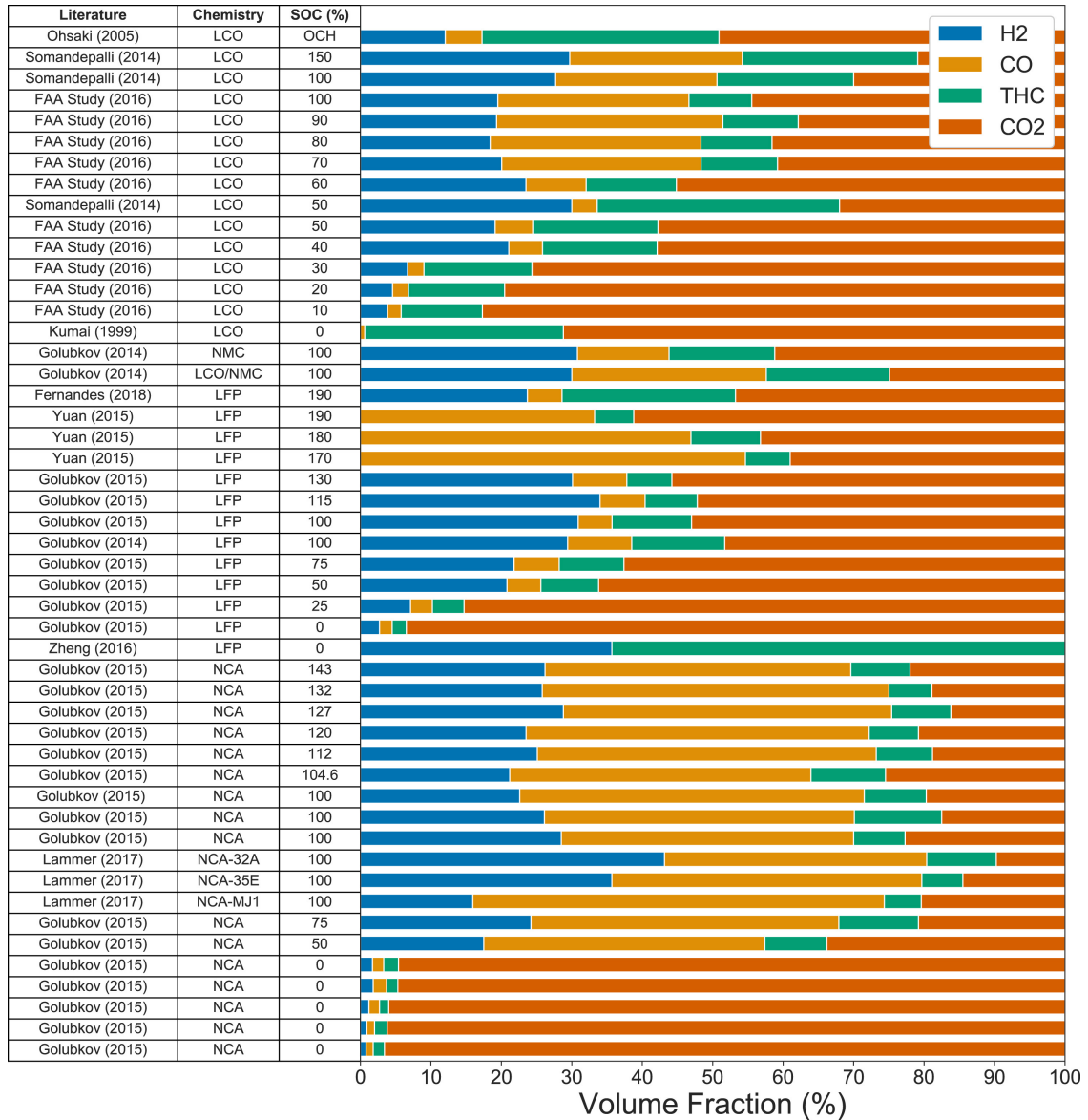
Figure 3.3. Battery vent gas species compositions from literature. Major species shown are hydrogen (blue), carbon-monoxide (orange), total hydrocarbons (green), and carbon-dioxide (red) [40]

21

Königseder [41] analysed in his thesis the gas production during TR in different cylindrical 18650 batteries, analysing the composition at different timing as reported in Figure 3.4. In particular, point 1,2, and 3 are around the first battery venting (slightly before, during and two minutes after), point 4 at the beginning of the TR event, point 5 at the temperature peak and points 6,7 and 8 after TR. As it is possible to see, gas volume starts rising around 8800 s causing the first battery venting. Then, the bigger production is caused by the rapid temperature rise due to TR. Analysing the composition at the different timing, Königseder [41] found that before TR (1-4) the gas composition is primarily N_2. From point 5 on, the production of CO, CO_2 and H_2 became relevant.
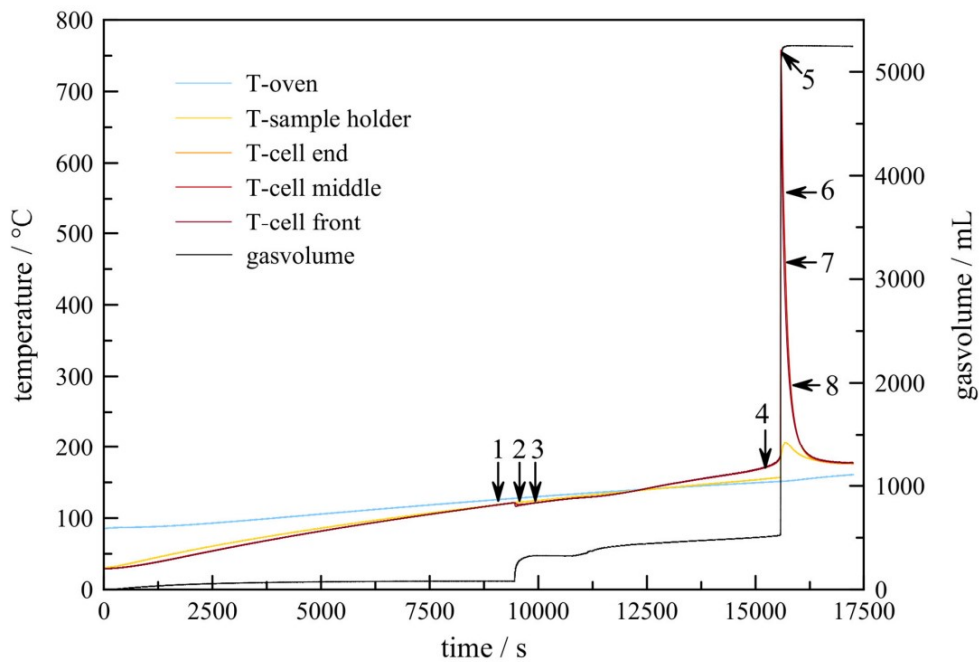
Figure 3.4. Temperature vs time on the left axis, and gas evolution on the right axis [41]

Gas releases affect surrounding targets differently. Gases can corrode equipment present nearby. People could be poisoned or even suffer asphyxiation due to the gases [36].

The problem of gas release is of major interest in regards of Battery Electric Vehicles (BEVs). In particular, the heat release and the gas composition are of critical interest in the understanding of BEV fire consequence, especially in closed environments (underground roads, garages, road tunnels) [42, 43]. The differences in the gas composition between BEV and Internal Combustion Engine (ICE) vehicle fire changes the chemical and toxicological risks, both for the people in immediate vicinity and for the firefighters. Moreover, careful handling of firefighting and

22

cooling water is needed [44]. The water used, in fact, is highly contaminated (higher concentration of heavy metals and HF) at levels that exceed current thresholds for discharge into the sewerage and so proper pretreatment are needed [44].

It is important to mention that no changes in the thermal hazards and in incident response procedures are identified among BEV and conventional vehicles fires [45].

3.1.2 Prevention and suppression strategies

In order to reduce the hazard of TR, three strategies can be carried out, as reported in Figure 3.5. Passive defence design it is necessary to reduce the secondary damage under abuse condition. Intrinsic safety consists in building the battery with materials that are prone to avoid and prevent TR. Lastly, it is necessary to avoid or limit the propagation in the battery pack.
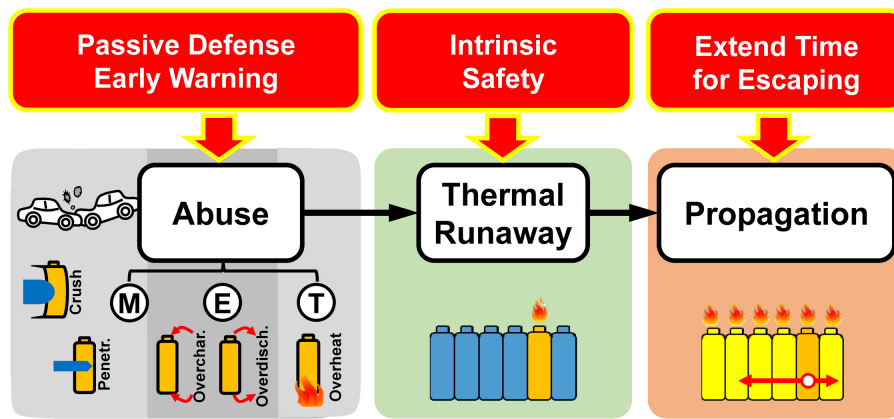
Figure 3.5. The three strategies to prevent and/or mitigate the effects of TR [39]

In order to suppress the occurrence of TR, there are different adoptable strategies [38], some of which already covered analysing the cell materials. In particular, it is possible to follow different strategies:

- **Improving cell materials**: it is a way to improve the intrinsic safety of the battery, as LIB's safety is linked to the materials of the different components, as seen in the previous sections. Summarizing the possibilities according to the component:

  - *Cathode*: it is possible to improve the cathode thermal performances through two primary techniques. The first one is element substitution, that consists in substituting transition metals present in the cathode (like Co, Ni and Mn) with Al. This permits to stabilize the crystal structure of layered oxide cathodes obtaining better thermal performances [38]. The second one is the use of surface coating made by different chemical or

thermal inert, to create a thin layer that prevents side reactions by avoiding the direct contact with the electrolyte [39, 38].

– *Anode*: as previously seen, SEI is crucial in terms of battery safety and performance. Researchers are studying the possibility of producing artificial SEI layers by coating the graphite with AlF_3 or Al_2O_3 is considered promising [38]. Alternatively, novel anode materials (as the already discussed LTO) are considered promising.

– *Separator*: in case of temperature rise the separator may reach its melting point causing the so-called "separator shutdown". To avoid the occurrence of ISC during this process, it is necessary to minimize separator shrinkage and collapse. This is achieved with new separators designs, such as triple-layered (PP-PE-PP)) separators, or using novel materials.

– *Electrolyte*: in this case, different additives are used. Some example are:

  * SEI supporting additives: used to mitigate SEI decomposition. In literature vinylene carbonate (VC) and vinyl ethylene carbonate (VEC) have been proposed [39].

  * Overcharge protection additives: they are able to stop the charging process at a defined voltage. These redox additives are effective at low current overcharge [38].

  * Flame retardant additives: they are used to improve the thermal stability of the organic solvents. They can be divided into chemical, if they terminate free radical linear reaction by capturing hydrogen radicals, or physical, if they dilute combustible components using flame-retardant vapour [24].
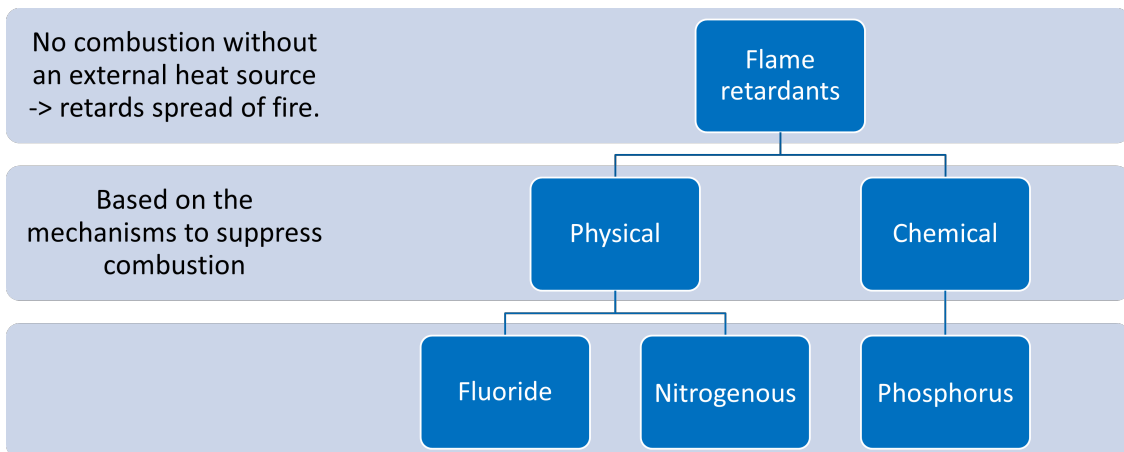
Figure 3.6.   Flame retardants classification based on the way of suppressing combustion

- **Safety devices**: different devices can be added to the battery to improve its safety, some of which are analysed in the following.

  - *Thermal Fuse*: this is a component that will melt due to Joule heating if short-circuit current flows through it, causing the shutdown of the battery [38].

  - *Positive temperature coefficient*: it protects the LIB against overcurrent and over-temperature, by increasing its resistivity after fault and, hence, inducing Joule heat and opening the load circuit. The device is made up of a ceramic and a composite of polymer and conducting materials.

  - *Current interrupting device*: it is used to protect the battery by interrupting the battery circuit when undesired excessive internal pressure emerges inside a Lithium-ion battery.

  - *Safety Vent*: it is used to release the gases produced during the TR event, so that when the pressure inside the steel can is too high, to avoid its rupture, the safety vent is opened. The safety vent is usually made of an aluminium alloy and can be in different forms (foil, edge, seam, or score) [38]. A typical safety vent in a cylindrical battery is reported in Figure 3.7.
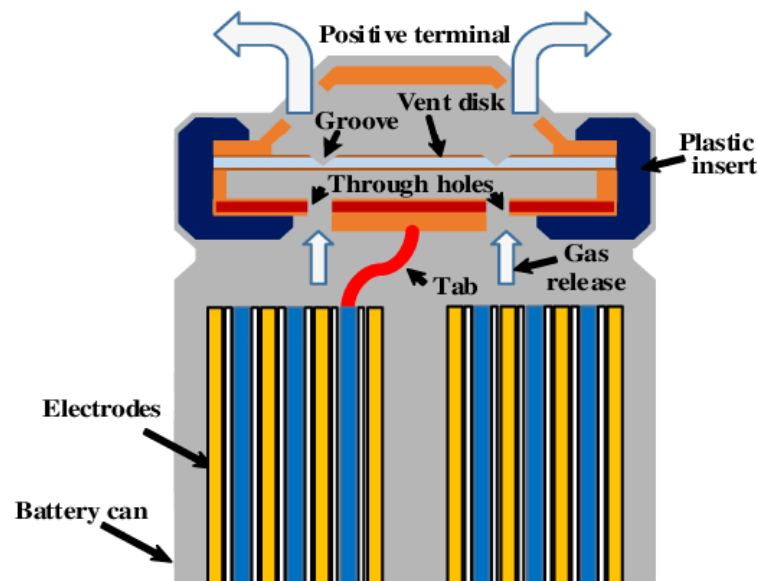
Figure 3.7. Typical safety vent in a cylindrical battery [46]

- **Battery Management System (BMS)**: it is equipped in the battery to protect it from overcharging and over-discharging. It also monitors the battery SOC (both at cell and pack level). Advanced system are equipped with fault

diagnosis function that compares the state of the single cell with the mean state of the battery pack to find the faulted cell [39].

- **Battery Thermal Management System**: it regulates the temperature within the battery pack in high and low-temperature environments to prevent overheating and improve the electrochemical performance of the battery.

Finally, mitigate the propagation of TR in the battery pack is crucial to reduce the hazard. As propagation is linked to heat transfer proper heat dissipation is required. Moreover, the use of phase changing materials is investigated.

3.2 Abuse testing

To ensure LIB safety, standards and test method are developed. LIBs must pass a series of safety tests to be certified for use in a particular application. These tests are performed to better understand the failure mechanism, considering both causes and consequences.

A variety of test exist, as report in Table 3.1, with the aim of inducing short circuit, internally or externally depending on the specific test performed. Tests are regulated by different standards developed by different national and international organizations (IEC, UN, ISO, etc.).

Table 3.1.   Possible tests depending on the type of abuse performed

Type of abuse	Possible tests
Mechanical	Nail penetration
	Heavy impact
	Drop
	Vibration
	Crush
Thermal	Thermal stability
	High and low temperature cycling
	Extreme temperatures
	Fire exposure
Electrical	Overcharge/Overvoltage
	Over discarge/voltage reversal
	External Short circuit

In the EVs sector these can be compared using the EUCAR[1] scale [37] reported in Table 3.2.

Table 3.2.   EUCAR severity of outcome levels

Hazard level	Description	Criteria for severity classification & severity
0	No Effect	No effect. No loss of functionality
1	Reversible Loss of Function	No defect; no leakage; no venting, fire, or flame; no rupture; no explosion; no exothermic reaction or thermal runaway. Cell reversibly damaged. Repair of protection device needed.
2	Irreversible defect/damage	No leakage; no venting, fire, or flame; no rupture; no explosion; no exothermic reaction or thermal runaway. Cell irreversibly damaged. Repair needed.
3	Leakage Δ_{mass}<50%	No venting, fire, or flame; no rupture; no explosion. Weight loss $<50\%$ of electrolyte weight (electrolyte=solvent+salt).
4	Leakage $\Delta_{mass} \geq$50%	No fire or flame; no rupture; no explosion. Weight loss $\geq 50\%$ of electrolyte weight. Heavy smoke (electrolyte=solvent+salt).
5	Fire or Flame	No rupture; no explosion (i.e. no flying parts)
6	Rupture	No explosion but flying parts of the active mass.
7	Explosion	Explosion (i.e. disintegration of the cell).

The final aim of these tests is to identify potential battery weak points and vulnerabilities so that the producer can build safer battery helping to reduce TR hazard. In this way, it is also possible to know what would happen in case real-life accidents, such as a car crash or thermal shock. Once the test is performed, it is possible to model the battery behaviour and predict the behaviour of the battery

---

[1]European Council for Automotive R&D

without running the tests that are mostly disruptive and can be costly in case of big battery packs.

3.2.1   Nail penetration test

This thesis focuses on the nail penetration test through experimental and numerical studies. The nail penetration test is an industry standard method to simulate an ISC in a cell. It is performed using an electrically conductive sharp rod to perforate the battery perpendicularly. The typical nail diameters range from 3 mm to 8 mm, depending on the standard considered, and the penetration speed is typically 8 cm/s. The test is considered successful if the cell does not explode or combust.

The variables in the nail penetration test are:

- Cell SOC

- Chemistry of the cell

- Geometry of the cell

- Nail speed

- Penetration depth

- Penetration position

- Nail material

- Nail diameter

- Tip shape

- Cell orientation

The influence of this variables have been studied by researcher in the last years. Huang et al. [47] studied the effect of SOC, penetration speed, penetration depth, penetration position and nail diameter on the behaviour of a LFP 18650 battery. The conclusion regarding the SOC effect is that the higher the SOC the bigger the battery response, in terms of higher overall and peak temperature. Regarding the nail speed, an higher speed generally meant an higher temperature. Moreover in terms of voltage a faster decrease to zero happens using higher nail speed. In terms of penetration depth, a more peculiar behaviour was found: below a certain threshold value of penetration depth (pd_{cr}) no TR happened. Above this value instead the TR triggers. The authors also analysed the influence of the penetration position comparing a near the poles (negative and positive) and at the centre founding a higher average temperature when the penetration happens near the poles of the battery. Finally, the using different nail diameters were tested founding that the

smaller nail caused the highest temperature. This has been explained considering the lower heat release performed by the small nail.

Other researcher analysed the influence of SOC in the nail penetration test all leading to the same conclusion even using other battery chemistry or geometry, such as Wang et al., Mao et al., Perea et al., Wang et al. [27, 48, 49, 50]. Same results were also obtained in terms of penetration depth [48]. Mao et al. [48], however, have come to another conclusion regarding the penetration position: using a NMC cylindrical 18650 battery, they found a more severe TR when the battery has been penetrated at the centre.

Wang et al. [50] not only tested different SOC state and two different nail diameters but also compared the result obtained with a tungsten nail with a polyformaldehyde one. In the case of polyformaldehyde nail both recovery (the voltage increase to a value sightly lower than the initial) and non-recovery mode (the voltage can have a slight recover but then drops to zero) have been observed, while only non recovery mode in the case of tungsten nail. In the first case (recovery mode) higher temperature are observed in the tungsten nail, while in the second case, the opposite is observed. A summary of the articles analysed is reported in Table 3.3 on the following page.

Table 3.3. Result comparison of conclusions in literature

	Huang et al.[47]	Wang et al.[27]	Mao et al.[48]
Chemistry	LFP	NMC	NMC
Geometry	18650 (cylindrical)	21700 (cylindrical)	18650 (cylindrical)
SOC	Higher SOC higher TR risk	same conclusion	same result
Speed	Higher speed higher temperature	Not analysed	same result
Depth	If higher than threshold, TR triggers	Only two depth considered, higher depth higher temperature	depends
Nail diameter	Lower d causes overall higher T	Not analysed	Not analysed
Penetration position	worst near the poles	Not analysed	worst at the centre

3.2.2 Short-circuit modes

When nail penetration happens, it triggers ISC in the LIB cells. According to Santhanagopalan, Ramadass, and Zhang [51], there are four main ISC modes as reported in Figure 3.8: the short circuit can happen between the active material of the anode and the one of the cathode (An-Ca, Figure 3.8 (a)), between the two current collectors (Al-Cu, Figure 3.8 (b)), between the positive current collector and the anode active material (An-Al, Figure 3.8 (c)) and lastly between the negative copper current collector and the cathode (Ca-Cu, Figure 3.8 (d)) .
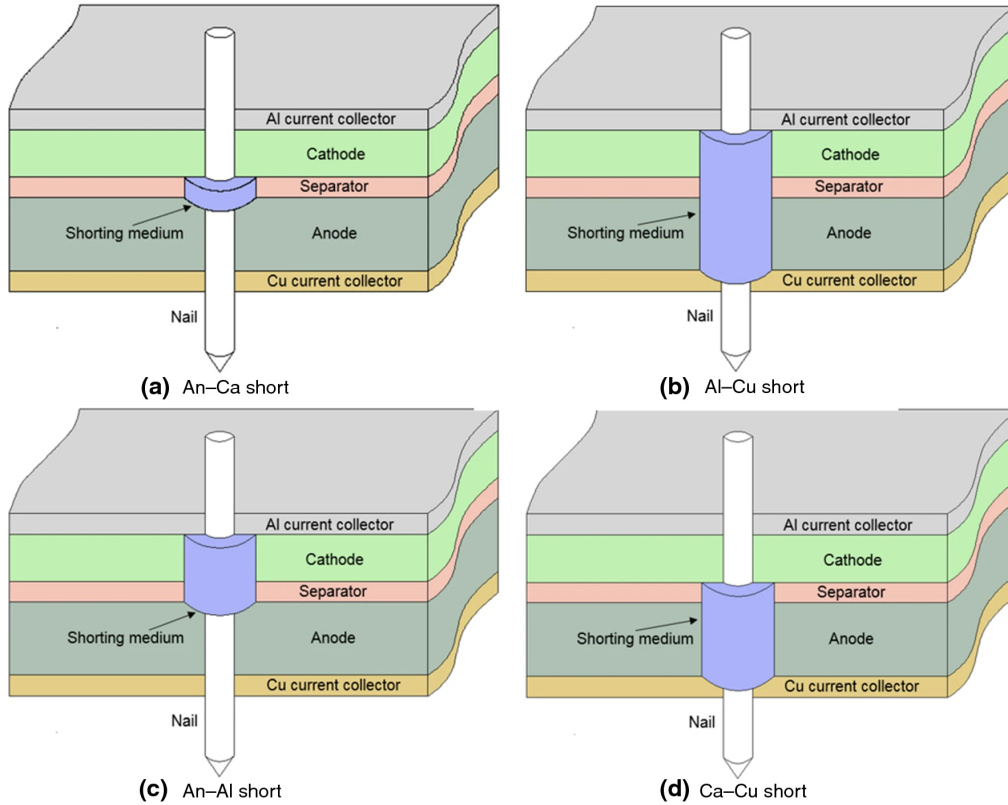
Figure 3.8. Illustration of the four main possible ISC modes [50]

In any of the above cases, the electrical resistivity of the short is calculated as the maximum of the resistivity of the two elements associated with the short. Thus, the conductivity of the (σ_{short}) is in essence, the minimum of the individual conductivity of the components involved in the short [51].

Going into more detail:

(a) An-Ca: it is the most common short circuit scenario [52, 51]. This is due to the much lower electric conductivity of the cathode with respect to the other components (anode and current collectors) [52]. However, it is one of the least

dangerous [52, 53]. As reported in Figure 3.9, the heat generation is almost the same as the Cu-Ca one and the temperature rise is limited to a few degrees above the ambient temperature [53].

(b) Al-Cu: this is similar to an external short circuit. The heat generated is quite high, even though not the highest, but thanks to the high thermal conductivity of the current collectors, the temperature rise is limited [51].

(c) An-Al: this short circuit mode is the most dangerous as the power generated increases sharply in the first few seconds as it is possible to see in Figure 3.9. Moreover, the temperature at the beginning increases in a similar way to the Al-Cu short, but then has a rapid increase. This runaway behaviour is caused by three main factors [51]; firstly anode material is characterised by low electrical resistivity, leading to a high power generation. In addition to this, the reactions at the anode are activated at lower temperatures than the one at the cathode. Lastly, the heat transfer on the anode side is inadequate [51].

(d) Ca-Cu: due to design of the battery, this short mode is the less likely to happen [51]. The power generated is usually not enough to reach the onset temperature for the chemical reaction to be triggered.
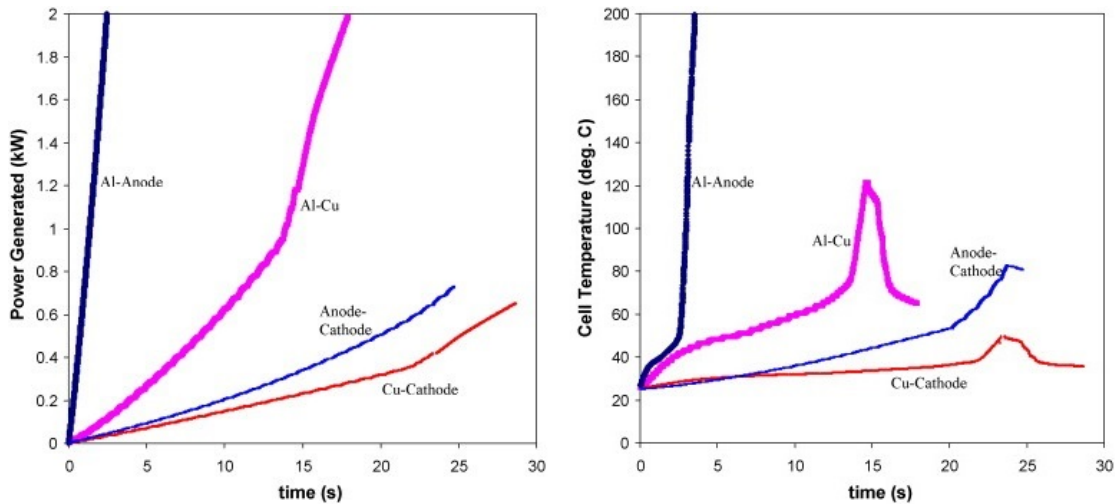
Figure 3.9.   On the left, power generated in the 4 main modes, on the right local temperature reached [51]

Among these, the An-Ca short circuit mode is highly investigated during nail penetration tests due to the fact that the foreign object (the nail) is usually made of an electrical conductor material so that when the separator is perforated it connects the two electrodes and the electrons flow through the nail from the anode to the cathode, where they undergo the lithiation reaction [53].

According to Zhang, Ramadass, and Fang [54], the number of possible kinds of ISC mode is 7, taking into account if it happens at the centre or at the end of the winding. These differences are better described in Table 3.4.

Table 3.4.   Summary of the 7 short circuit modes according to Zhang, Ramadass, and Fang [54]

Case	Type (location)	Power	Chemical reaction	TR possibility
1	An-Al (inside)	High	Yes	Very high
2	An-Al (edge)	High	Depends on Li amount	Low (small Li content)
3	Al–Cu (inside)	High	Yes	Can be high (depends on cell size and design)
4	Al–Cu (edge)	High	No	Very low
5	Ca–Cu (inside)	Low	Yes	Very low
6	Ca–Cu (edge)	Low	Depends on cathode material	Very low
7	An-Ca (inside)	Low	Yes	Can be low (depends on cell size and design)
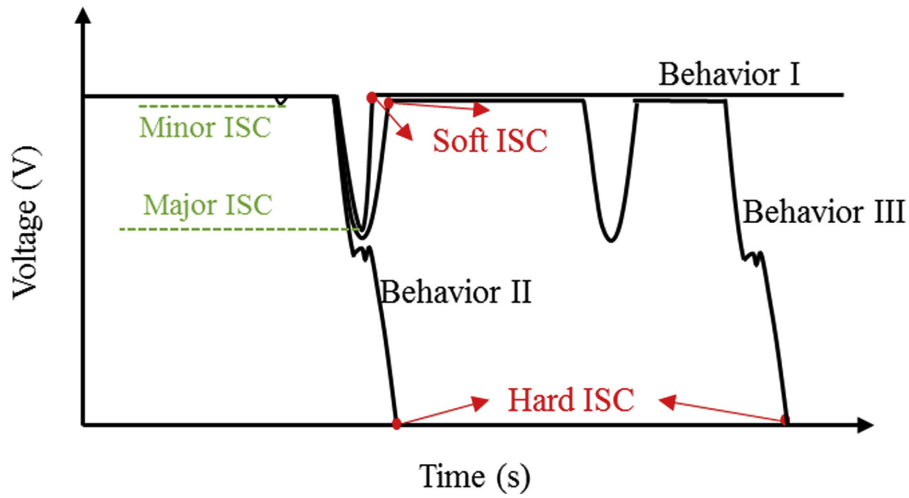
Figure 3.10.   Different voltage behaviours under penetration and some definitions [55]

Even though these ISC scenarios have been widely analysed, the real ISC behaviour is more complicated [53]. In particular, Liu et al. [55], identified different behaviour according to the evolution of voltage over time as reported in Figure 3.10. According to the initial voltage drop, ISC is categorized into minor ISC (low drop, lower than 0.05 V) and major ISC (drop higher than 0.1 V). Subsequently, there

can be hard ISC (unrecoverable, voltage drops to zero) and soft ISC (voltage is recovered at a constant value). In particular, after major ISC three behaviour can be identified:

- Behaviour I: corresponds to a soft ISC in which the voltage is recovered within seconds and kept to a constant value

- Behaviour II: a hard ISC where the voltage drop to a null value within one second

- Behaviour III: voltage is subject to several fluctuations of drop and recovery, but finally reaches a null voltage.

Chapter 4

Battery models

4.1 Model classification

A battery model is a set of mathematical equations that tries to explain the behaviour and performance of the battery under study. Due to the complexity of battery devices, it is necessary to deeply study the phenomena and kinetics of the electrochemical reactions taking place in them with the aim to be able to develop better and safer batteries.

Battery models can be done at different levels depending on the final goal as reported in Figure 4.1. In particular, the atomistic/molecular level is used for material selection and innovation. This is achieved through quantum mechanical models that are limited to very small length scales and short time scales [56, 57]. Electrode one is useful for electrode design and manufacturing process. The battery level is used to simulate battery charge and discharge curves, safety under abuse condition and swelling of the cell. Package level is used to design the thermal management. Finally, system level is used for system coupling and integration.

Molecular level	Electrode level	Cell level	Pack level	System level
Material innovation Material selection	Electrode layout Manufacturing process Life	Charging, discharging profiles Heating Swelling deformation	Thermal management BMS Logic Durability Safety EMI/EMC	System integration
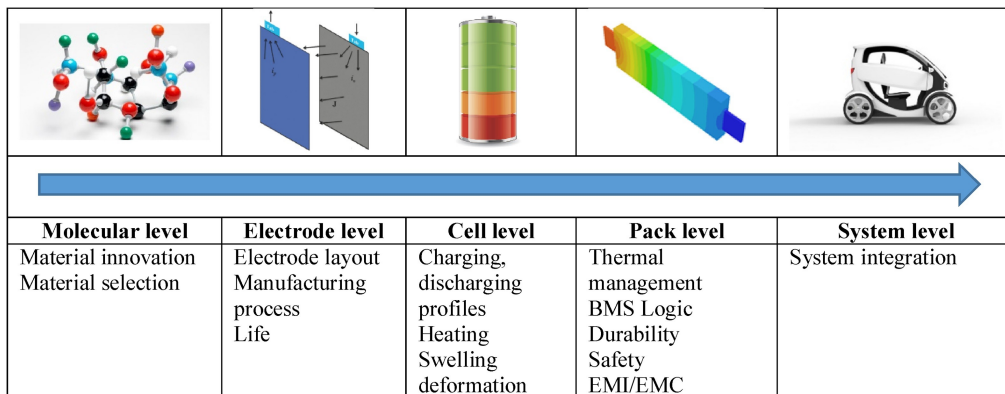
Figure 4.1. Different levels of battery model precision and their possible final goal [58]

Battery models can also be grouped according to Figure 4.2.
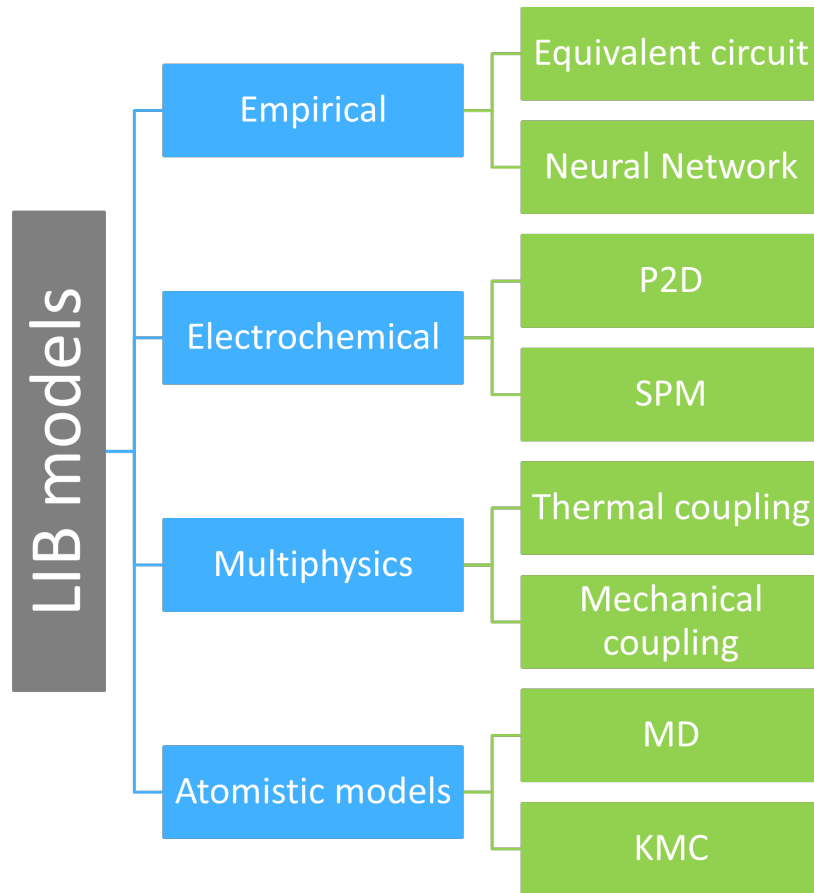
Figure 4.2.   Classification of different models

 Going into more detail of each category:

- **Empirical models**: the equations parameter are fitted using battery history and the experimental data through polynomial, exponential, power laws, logarithmic, and trigonometric functions [57, 59]. In this way it is possible to predict the battery future states.

  – Equivalent circuit models: it is a phenomenological approximation of the behaviour of the cell obtained trough electrical equivalent circuits. The circuit elements (resistors, capacitors, etc.) are not used to describe how the cell is made, but to mimic its behaviour [60]. They don't include descriptions of battery physics and they are classic black box models. These models are widely used due to their robustness and simplicity [60]. They, in fact, satisfy the balance between complexity and accuracy achieving high calculation speed, allowing easy implementation of these models in

the microprocessor of control systems even for real-time results [61]. Their major drawback is that not being based on the physical behaviour of the battery, it is not possible to evaluate physics-based parameters [62]. Moreover, the battery characteristics are not updated over time (e.g., it is not possible to model the battery ageing). Common equivalent circuit models include the Rint model, Thevenin model, Partnership for a New Generation of Vehicle (PNGV) model, and General Non-Linear (GNL) model as reported in Figure 4.3.
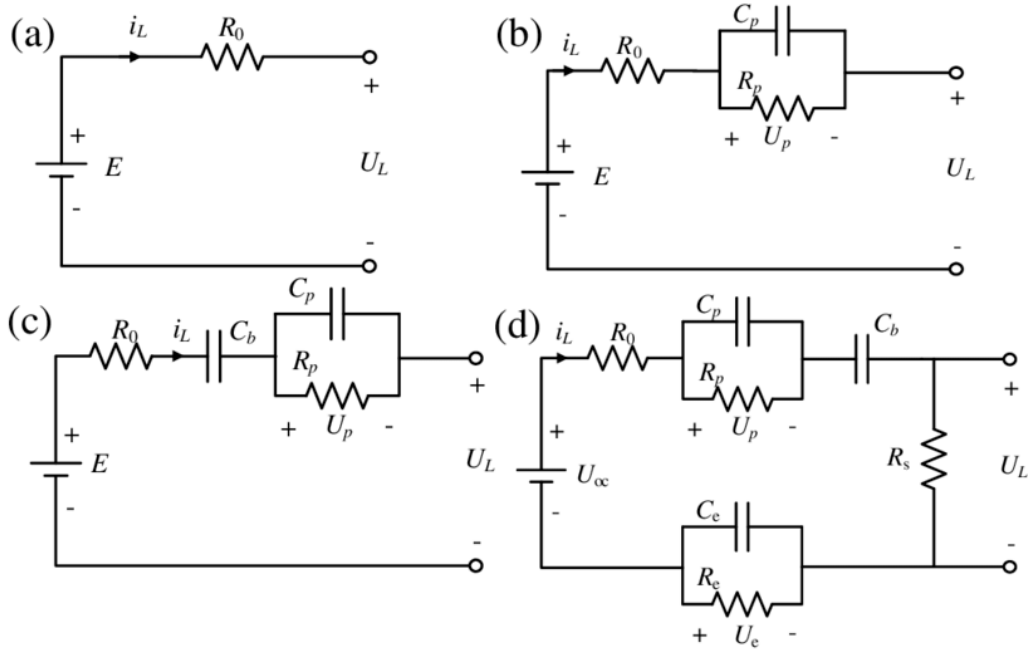
Figure 4.3.   The equivalent models of Li-ion battery (a) Rint model (b) Thevenin model (c) PNGV model (d) GNL model [63]

 – Artificial Neural Networks: they are models inspired by biological synaptic connections; the artificial neuron are connected one with the others and each of them is associated to a weight and a threshold. If the output is above the threshold the data is sent to the next artificial neuron, otherwise no data is sent. These model are composed of three layers as reported in Figure 4.4 on the following page: the first one takes the input (in the battery case it can be voltage, current and temperature) and the last one produces the outputs (SOC or the State of Health). The layer in the middle is called hidden layer as it has no direct connection with the external. The network is trained using a back-propagation algorithm based on experimental results [64].
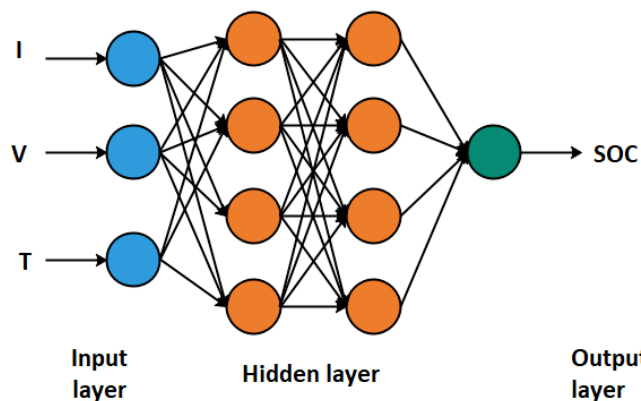
Figure 4.4.   Scheme of an Artificial Neural Network (NN) for SOC estimation [65]

- **Electrochemical models**: aim at describing the battery fundamental physical phenomena such as mass balance, energy balance, heat transfer relations, and so on using partial differential equations coupled together, so that an increase of computational effort is made and numerical solutions techniques are required [61]. The two most important electrochemical models are:

  - Pseudo-two-dimensional (P2D) model: so called for the presence of two disparate but connected 1D dimensions, x and r. Along x, in the macroscopic scale, the processes in the electrolyte are represented. While r, in the microscopic scale, describes the normal direction to the surface of each electrode particle [66]. It is also known as the Doyle-Fuller-Newman (DNF) model after the name of its inventors [67].
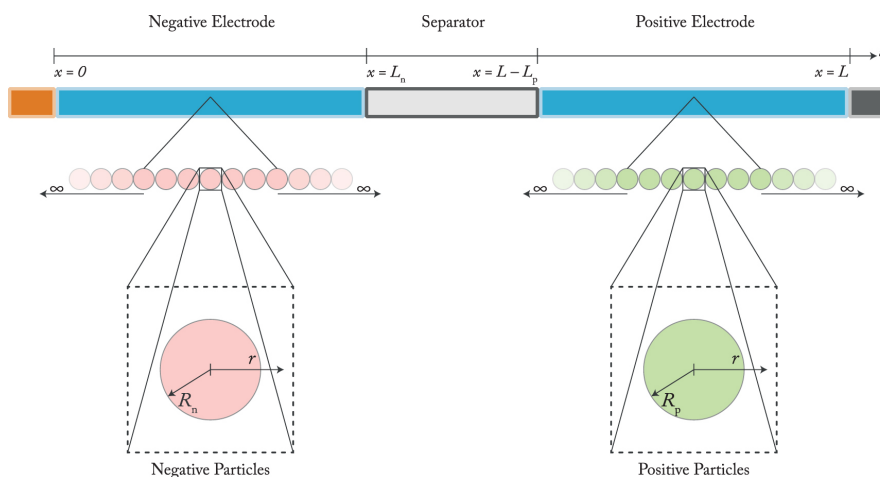
Figure 4.5.   P2D battery model scheme [57]

– Single Particle Model (SPM): it is a simplified P2D based on the assumptions that the battery applied current is small and the conductivity of the electrolyte is large. As a consequence, each electrode is described as a single spherical particle as represented in Figure 4.6. Thanks to this simplification the model is easier to implement (lower computational effort). Its main drawback is that it must be fine-tuned according to the electrolyte properties for thick electrodes and at high discharge rates [62].
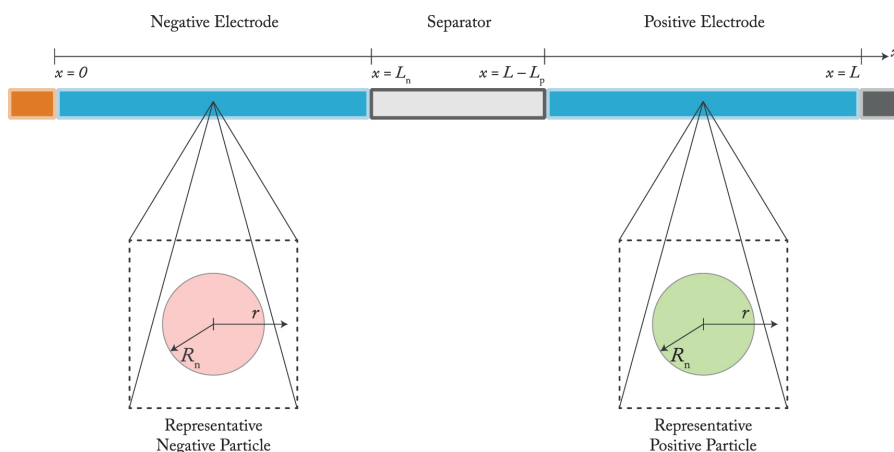
Figure 4.6. SPM battery model scheme [57]

- **Multiphysics models**: these are necessary to better describe phenomena occurring during LIB operation, in particular in case of high power/energy applications [68]. This is mainly done by coupling the electrochemical models (e.g., P2D) with thermal, stress models or even combination of the two (as done by Liu, Yin, and Xu [69] to model a nail penetration test).

- **Atomistic models**: under this name a range of different length and time scales are represented. Among the most important, it is possible to identify:

  – Molecular Dynamic (MD): it shows the dynamic evolution of a system over time. It can be divided into *ab initio* and potential-based MD wheter the potential energy surface is described by solving Schrödinger equations or using parametrised interatomic potentials. The latter can reach longer time and length scales at the cost of not being able to capture some details [70]. It has been used to simulate of the initial growth of the passivating SEI film at the interface of the solvent and graphite anode and for the initial transport of lithium ions through a polycrystalline cathode [68].

  – Kinetic Monte Carlo (KMC): is the most advanced battery model consisting of a powerful dynamic simulation technique that allows simulating longer time scales, without losing configurational atomistic details [71].

Each of these categories is different in term of complexity, computational speed and accuracy, as represented in Figure 4.7. Including more detail in a battery model can improve its predictions but at a cost of increased computational requirements [68]. For this reason, empirical models that are the easiest to implement are widely used in the BMS where thanks to their high computational speed an almost immediate response is given. [57, 62]. Electrochemical models are widely used among literature due to their compromise between computational speed and accuracy. However, as many of the electrochemical processes occurring within a battery are strongly temperature dependent, it is oftens required to couple the electrochemical models with a thermal one to capture this behaviour, obtaining multiphysics models. This can greatly increase the computational requirements. Lastly, the highest predictive accuracy is given by atomistic models. They can be used to predict new behaviour not currently accessible by experiment, for quantifying and evaluating trends in experimental data, explaining structure-property relationships, and informing materials design strategies and libraries [70].
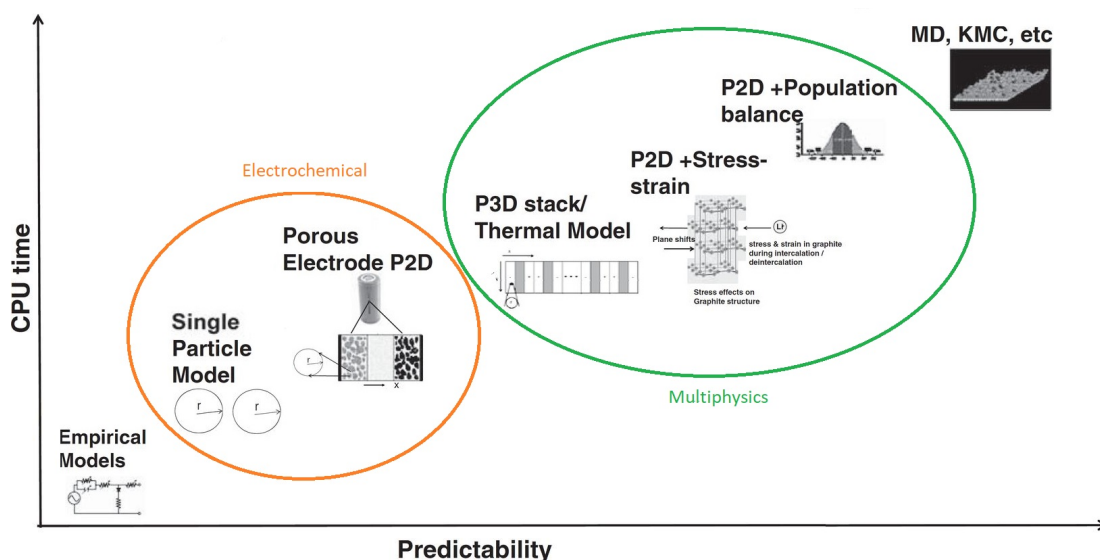
Figure 4.7. Computational demand (CPU time) vs accuracy of the model [68]

4.2 P2D parameters

Even though P2D model can be significantly more complex than other continuum models, it is the most used among researchers as it captures the necessary features to represent the battery behaviour in an extremely broad range of operating conditions [57, 68]. The P2D is based on the porous electrode theory, the concentrated solution theory and the kinetic equations [62]. In particular, the electrodes are considered as

a porous matrix and their behaviour is modelled with particles, usually spherical, surrounded by the electrolyte [62]. As a consequence, it is described by a set of non linear partial differential equation (see Section 6.1 on page 59 for more details). A full analytical solution is unavailable for those equations, so Finite Difference Methods (FDM), Finite Volume Methods (FVM) and Finite Elements Methods (FEM) are implemented (e.g.,COMSOL Multiphysics® has this model implemented in the Battery Design Module) [62, 66].

As the model that will be implemented in Chapter 6 on page 59 is based on the P2D model, a focus on the required parameter is given here. In order to solve the P2D electrochemical model, in fact, an extensive list of parameters is required as input. These parameters give an insight in the physical, chemical and electrochemical phenomena involved in the cell [72] as summarized in Figure 4.8. In particular, they describe the cell geometry, thermodynamic and kinetic.
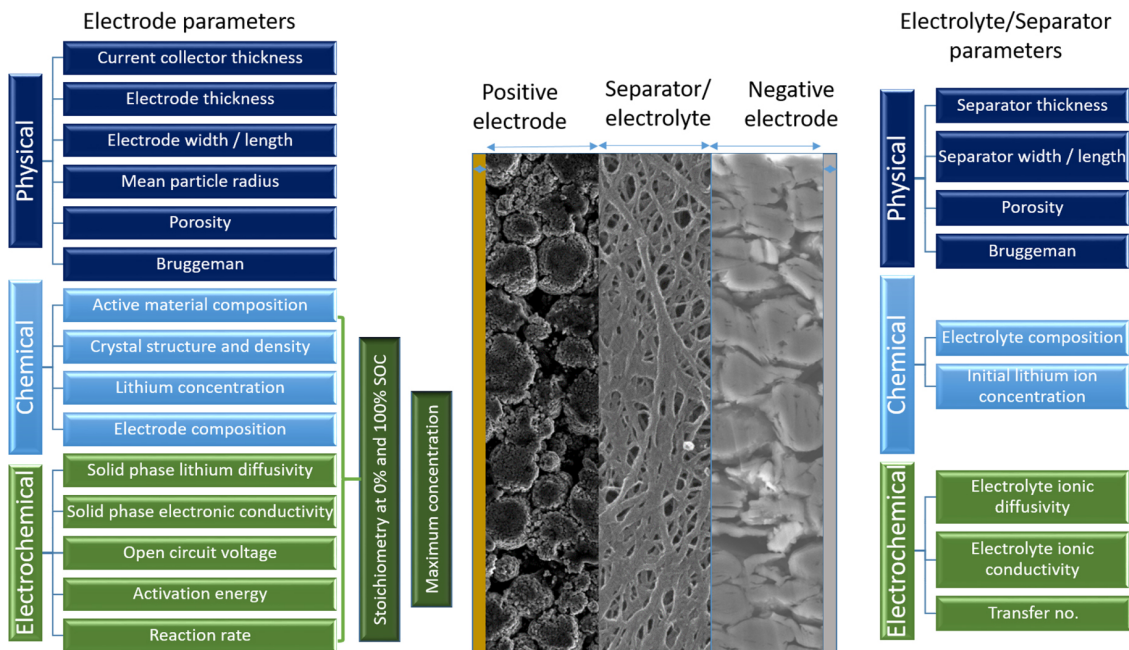
Figure 4.8. Summary of the different model parameters required to as input to solve P2D model [72]

The main problem is linked to obtaining and setting these values. In fact, even though this can be challenging, it is required in order to produce a reliable model. The different feasible strategies to obtain suitable values are [72]:

- **Literature review**: in this case parameters from literature are used. However, many problems can occur due to inconsistencies among sources, different material composition among batteries (two batteries may have the same cathode material but properties changes among manufacturer, for example) and so on.

Falconi [73] studied different sources to analyse how the different values were obtained as reported in Figure 4.9. As it is possible to see most of them are either obtained from other sources or not explicated, meaning that it is not easy to trace their origin.

	D_e	σ_-	σ_+	d_-	d_e	d_+	R_-	R_+	$D_{s,-}$	$D_{s,+}$	β_-	β_e	β_+	t_+	C^*	$Cs_{max,-}$	$Cs_{max,+}$	$\varepsilon_{s,-}$	ε_-	ε_e	$\varepsilon_{s,+}$	ε_+	$k_{0,+}$	$k_{0,-}$	κ_e
Albertus_2008 [161]	L	A	A	F	A	F	L	L	L	L	L	L	L	L	L	L	L	L	L	L	L	L	A	A	L
Albertus_2009 [162]	L	L	L	A	A	A	A	A	L	L	L	L	L	L	A	L	L	A	A	A	A	A	L	L	L
Awarke_2013 [81]	L	A	A	L	L	L	L	L	F	F	F	L	L	L	L	L	L	A	A	A	A	A	F	F	L
Christensen_2013 [107]	L	A	A	A	A	A	A	A	A	A	A	A	A	A	A	A	A	A	A	A	A	A	A	A	L
Cobb_2014 [156]	L	A	A	A	A	A	A	A	A	A	A	A	A	L	A	A	A	A	A	A	A	A	A	A	L
Darling_1997 [154]	L	L	L	A	A	A	A	A	A	A	A	A	A	L	A	A	A	A	A	A	A	A	A	A	L
Darling_1998 [80]	L	L	L	A	A	A	A	A	F	F	A	A	A	L	A	A	A	A	A	A	A	A	F	F	L
Ecker_2015 [88], [142]	M	M	M	M	M	M	F	M	L	L	M	M	M	L	M	M	M	M	M	M	M	M	F	F	M
Ferrese_2012 [112]	L	L	L	M	M	M	L	L	L	L	L	L	L	L	L	L	L	L	L	L	L	L	L	L	L
Ferrese_2014 [99]	L	L	L	M	M	M	L	L	L	L	L	L	L	L	L	L	L	L	L	L	L	L	L	L	L
Fu_2014 [163]	A	A	A	A	A	A	A	A	A	A	A	A	A	A	A	A	A	A	A	A	A	A	A	A	A
Guo_2013 [103], [104]	L	A	A	A	A	A	A	A	A	A	A	A	A	L	A	A	A	A	A	A	A	A	A	A	L
Jsari_2011 [114]	F	L	L	L	L	L	F	F	L	L	L	L	L	L	L	L	L	F	F	F	F	F	A	A	F
Ji_2013 [105]	L	L	L	M	M	M	A	A	L	L	L	L	L	L	M	L	L	L	M	M	L	M	F	F	L
Kim_2014 [92]	L	L	L	L	L	L	L	L	L	L	L	L	L	L	L	L	L	L	L	L	L	L	L	L	L
Kumaresan_2008 [164]	L	L	L	A	A	A	A	A	F	L	F	F	F	F	A	A	A	A	A	A	A	A	F	F	L
Zhang_2014 [93]	F	A	A	A	A	A	F	F	F	F	A	A	A	F	A	A	F	F	F	F	F	F	F	F	F
Legrand_2014 [95]																									
Martínez-Rosas_2011 [72]	L	L	L	L	L	L	L	L	L	L	L	L	L	L	L	L	L	L	L	L	L	L	L	L	L
Ning_2004 [165]	A	A	A	A	A	A	A	A	A	A	A	A	A	A	A	A	A	A	A	A	A	A	A	A	A
Nyman_2010 [73]	L	L	L	L	L	L	L	L	L	L	L	L	L	L	L	L	L	L	L	L	L	L	L	L	L
Barai_2015 [84]	L	L	L	L	L	L	L	L	L	L	L	L	L	L	L	L	L	L	L	L	L	L	L	L	L
Prada_2013 [166]	L	A	A	M	M	M	M	M	A	L	L	L	L	L	A	L	L	A	A	A	A	A	A	A	L
Ramadass_2003	A	A	A	A	A	A	A	A	A	A	A	A	A	A	A	A	A	A	A	A	A	A	F	F	L
Ramadass_2004	A	A	A	A	A	A	A	A	A	A	A	A	A	A	A	A	A	A	A	A	A	A	A	A	L
Sikha_2004 [145]	A	A	A	A	A	A	A	A	A	A	A	A	A	A	A	A	A	F	F	F	F	F	A	A	L
Stephenson_2007 [116]	A	A	A	A	A	A	A	A	A	A	A	A	A	A	A	A	A	A	A	A	A	A	F	F	L
Suthar_2015 [86], [158]	L	L	L	A	A	A	A	A	L	L	A	A	A	L	L	L	L	L	L	L	L	L	L	L	L
Lin_2013 [108]	A	A	A	A	A	A	A	A	A	A	A	A	A	A	A	A	A	A	A	A	A	A	A	A	A
Zavalis_2012 [110]	L	A	L	L	L	L	L	L	L	L	L	L	L	L	L	L	L	L	L	L	L	L	L	L	L
Zhao_2015 [87]	L	L	L	L	L	L	L	L	L	L	L	L	L	L	L	L	L	L	L	L	L	L	L	L	L

Figure 4.9. P2D model parameters and how they are obtained in different sources: in blue (L) if the authors take the value from another article, in yellow (A) if they are assumed either by the author or they are not explicated, in red (F) if values are fitted by the author, in green (M) if they are measured by the author [73]

- **Experimental identification**: this can be a good way to obtain more accurate values but different characterization methods are necessary, and some of the tests are destructive. Chen et al. [72] analysed the way through which it is possible to obtain some of the parameters. Here a summary is reported:

  - Physical parameters: they can be generally obtained through the tear-down of the battery. In particular:
    * Dimensions (thickness and width): measured after tear down and after been dried to remove electrolyte residues.
    * Mean particle radius: it can be obtained analysing Scanning Electron Microscope (SEM) images.
    * Porosity: different imaging techniques can be used to obtain this property: X-ray tomography and electron microscopy. The presence of carbon based binders can be difficult to identify in graphite and graphite based electrodes (due to their similarity).

42

- Chemical parameters: active electrode material can be evaluated using Inductively Coupled Plasma Atomic Emission Spectroscopy (ICP-AES) and Energy-Dispersive X-ray Spectroscopy (EDS). The choice depends on the materials involved (e.g., ICP-AES is used for NMC cathodes but cannot be used for silicon based electrodes).

- Electrochemical parameters: parametrization can be performed using two-electrode full cells, half cells (with lithium as counter electrode) and three-electrode configurations. All methods have limitations, and therefore a combination is preferred.

- **Parameter identification**: this method consists in evaluating the parameters by using only the model response [74], which means by fitting experimental curves. It is not totally clear if regular tests enough to identify the parameters or if new data should be produced: in some publication this problem has been addressed formulating an input trajectory optimization problem as done by Park et al. [75]. Research is focused in this area as the previously mentioned strategies are not reliable or invasive and based on destructive experiments. A summary of different studies and the strategy followed to set the parameters' value is reported in Table 4.1.

Table 4.1. Parameter identification studies for P2D models. The number of estimated parameters and the strategy used to obtain them is reported, along with the experimental data used for validation. Used abbreviation: NN

Reference	Identified parameter	Strategy	Experimental data
Rajabloo et al. [76]	8	Genetic algorithm	C-rate tests
Kim et al. [77]	6	Bayesian NN	C-rate tests
Chun et al. [78]	6	Recurrent NN	Dynamic tests
Laue, Röder, and Krewer [79]	10	Levenberg-Marquardt	C-rate tests, dynamic tests, impedance spectroscopy
Xu et al. [74]	14	Deep learning algorithm and genetic algorithm	C-rate tests, dynamic tests
Vazquez-Arenas et al. [80]	18	Fitting and analysis of variance	C-rate tests
Masoudi et al. [81]	4	Homotopy optimization	Discharge curve
Jin et al. [82]	5 (+11)	Levenberg-Marquardt	C-rate tests, pulsed discharge inputs

Problems of parameter identification are that parameter sensitivity varies under different operational conditions and also that the identification problem can be time-consuming [74].

4.2.1 Influence of design parameters

The influence of parameter on the P2D is studied both through numerical modelling and through sensitivity analysis. In the first case, parametric sweep has been performed to analyse their impact on discharge curves.

In the second case, parameter sensitivity analysis is performed to determine the change in the model output due to parameter changes. This is important as it helps to reduce the size of the identification problem by focusing on high-sensitivity parameters. Different sensitivity analysis method can be used, divided into local sensitivity analysis if the value is changed around its nominal value, or global if it is varied across all the feasible values. Due to the non-linearity of the P2D governing equations and the consequent complexity of the model, global sensitivity analysis is preferred and the Elementary Effect Test (EET) is one of the most used methods [74]. Through sensitivity analysis, Xu et al. [74] evaluated that there are 14 high sensitivity parameters, mainly the one linked to geometry (electrodes thickness) and to the lithiation state of the electrodes. Same results has been obtained by Li et al. [83] as reported in Figure 4.10. It is however important to understand that those conclusion are specific of the cell under study and can vary among other chemistries, model and manufacturers.

Previous studies have revealed that some of the P2D model parameters are unidentifiable because they have little impact on the model output when their values are changed [75, 79].
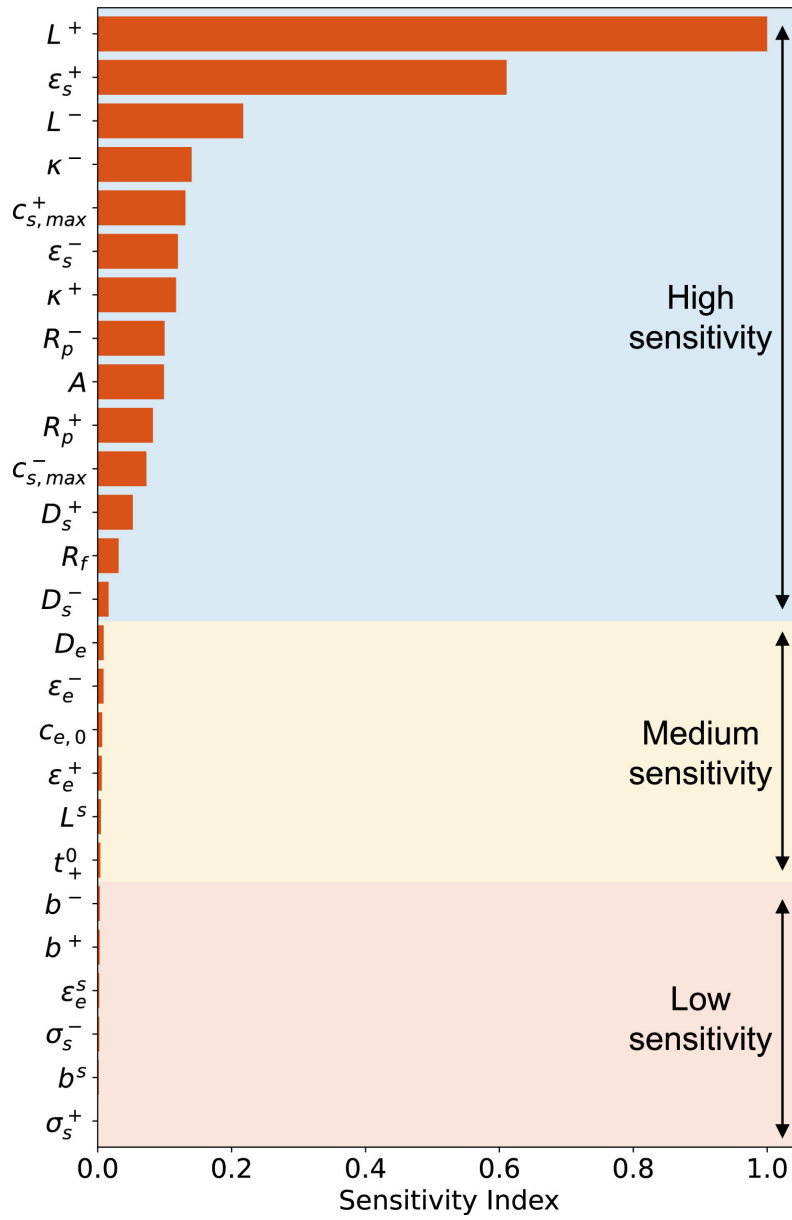
Figure 4.10.   Results of the sensitivity analysis performed by Li et al. [83]

Part II

Experimental section

Chapter 5

Nail penetration experiments

5.1 Materials and methods

5.1.1 Battery samples

Two different batteries have been used to perform the test, the ICR18650-26H and INR18650-29E models produced by Samsung SDI Co.,Ltd., whose characteristics are reported in Table 5.1.

Table 5.1. Specification of the two batteries used to perform the tests

Specification	ICR18650-26H	INR18650-29E
Type (-)	Cylindrical	Cylindrical
Diameter (mm)	18	18
Height (mm)	65	65
Nominal capacity (mAh)	2600	2850
Nominal voltage (V)	3.63	3.65
Charging voltage (V)	4.2 ± 0.05	4.2 ± 0.05
Charging method (-)	CC-CV	CC-CV
Charging current (mA)	1300 (Standard) 2600 (Rapid)	1375 (Standard)
Charging time (hours)	3 (Standard) 2.5 (Rapid)	3 (Standard)
Discharge Cut-off Voltage (volt)	2.75	2.5
Cell weight (g)	47	48
Operating temperature (°C)	Charge: 0–45 Discharge: -20–60	Charge: 0–45 Discharge: -20–60

The two batteries are both 18650 cylindrical batteries. As already said, the 18650

standard is very common and widely used in different applications. In particular, the 26H model is used for laptops, power banks and both of them are used in battery packs for e-bikes [84].

The chemical composition is reported in Table 5.2. In both cases the cathode is made of Nickel Manganese Cobalt Oxide (NMC) coated onto aluminium current collector, and the anode is made of graphite coated onto copper current collector. The electrolyte is liquid and based on $LiPF_6$ and organic solvents, consequently the flammability issue is present. In both cases, in case of fire, the production of HF, CO and CO_2 cannot be excluded [85, 86].

Table 5.2.   Chemical composition of the components of the two batteries used to perform the tests [85, 86]

Component	ICR18650-26H	INR18650-29E
Anode	Graphite	Graphite
Cathode	NMC	NMC
Electrolyte	$LiPF_6$, organic carbonates	$LiPF_6$, cyclic and linear carbonates
Separator	Polyvinylidene fluoride (PVdF)	Polyethilene (PE)

5.1.2   Experimental setup

The nail penetration tests have been performed using the Thermal Hazard Technology EV+ Accelerating Rate Calorimeter (ARC) provided with the auxiliary option called Nail Penetration and Crush Option (NPCO) present at the Energy Center facility[1]. The EV+ ARC is composed by two parts as represented in Figure 5.1 on the following page:

1. Blast box

    (a) Calorimetry assembly where the sample is tested. It is made of a thick aluminium jacket that grants near perfect adiabatic conditions. It contains a series of heaters and thermocouples.

    (b) Optional equipment if needed.

    (c) Containment vessel made of steel and designed to prevent any external effect in case of explosion within the calorimeter. In addition, it has a built-in fume extraction system, to allow an automatic exhaustive gas neutralization and flushing of the pressure line after the test.

---

[1]Energy Center - Politecnico di Torino, Via Paolo Borsellino 38/16, Torino

2. Electronic cabinet

   (d) PC workstation where the software (windows based) allows the user to run the test. It is provided of monitor, keyboard and mouse for user interface.

   (e) Option support unit for the data acquisition from the calorimeter.

   (f) Power supply unit that provides power to the calorimeter.
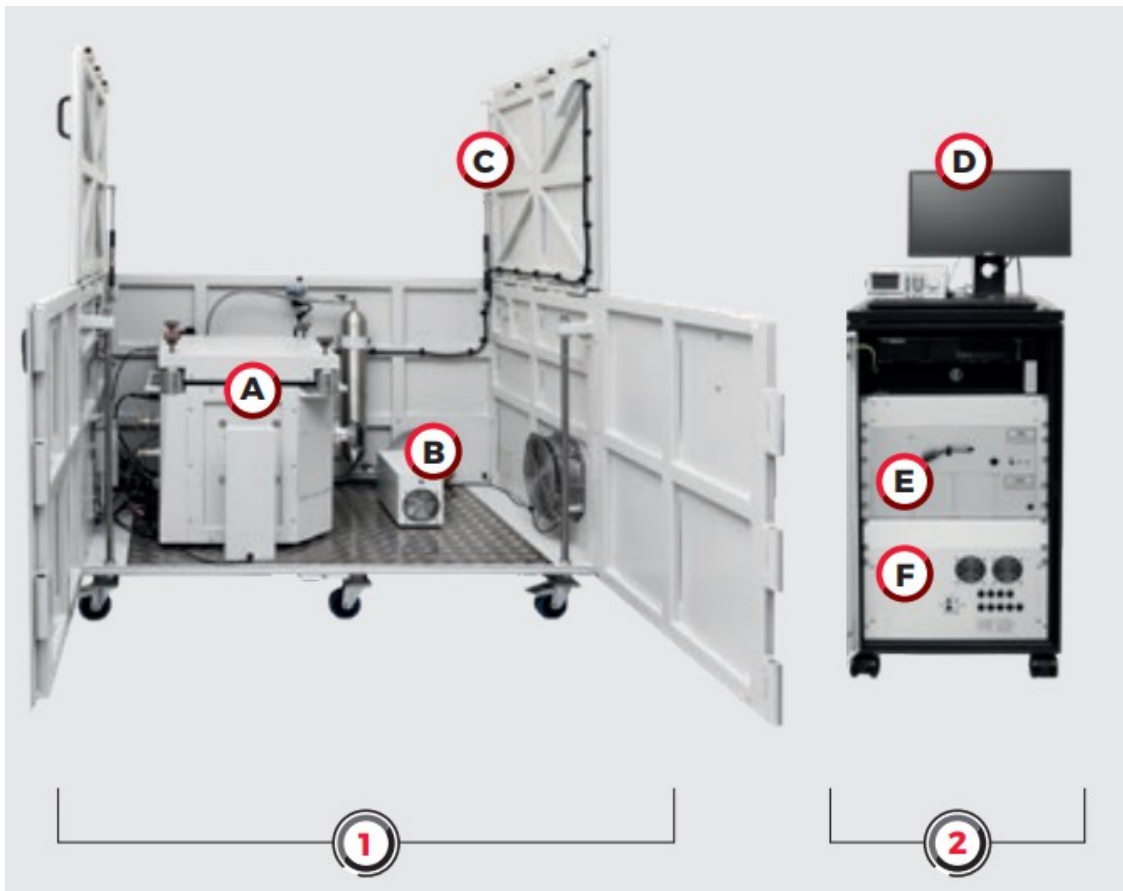
Figure 5.1.   Thermal Hazard Technology EV+ equipment [87]

Being of modular design, it is possible to introduce optional components such as the NPCO as done for this experiment. The NPCO allows users to perform nail penetration and crush tests on prismatic and cylindrical cells within the ARC. This is done using the nail penetration pneumatic cylinder assembly that is possible to see in Figure 5.2 on the next page.
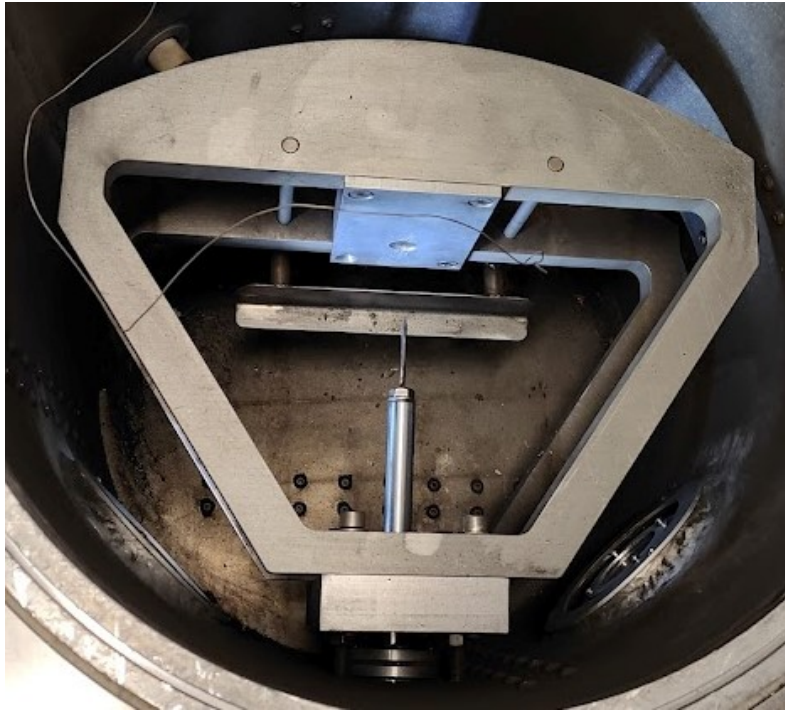
Figure 5.2.   NPCO at the Energy Center facility

5.1.3   Experimental procedure

All batteries used to perform the nail penetration tests have been firstly charged to reach full charge (State Of Charge (SOC) equal to 100%) using che CC-CV (constant current - constant voltage) method. Before starting the actual test, the ARC has been manually and automatically initialized. The battery is then positioned in and secured to the support of the NPCO reported in Figure 5.2. The battery is placed so that the penetration happens near its geometric centre in a radial direction. All tests have been performed using an AISI 316 stainless steel nail, with a diameter equal to 4 mm that penetrate the battery at a nail speed equal to 80 mm/s starting 35 mm from the battery. The battery is completely penetrated and, once the nail fully penetrates the battery, it remains in that position.

Once the battery is correctly secured in the NPCO and the ARC is closed, it is possible to set the starting temperature (Abuse Temperature) of the test (15 °C or 20 °C) using the workstation. This sets the temperature from which the experiment begins (the nail starts moving). The ARC follows the following procedure: a small heat step is given, after which the ARC enters the so called "wait time" to give isothermal equilibration. This is followed by a seek period where the system measures temperature variation in the system. If the temperature of the sample is not rising at a rate greater than the set sensitivity (0.02 °C/min) a new small

heat step is programmed. This heat-wait-seek procedure continues until during a seek period there is temperature rise measured at the sample thermocouple which is above the chosen sensitivity. At this point an exothermic reaction is detected and the exothermic mode is entered. In the case of nail penetration, after the penetration, Internal Short Circuit (ISC) is induced and heat is released and so the exothermic mode is entered.

The battery is kept in the ARC until a small enough temperature is reached (Cool temperature equal to 35 °C), after which it is possible to open the calorimeter with precaution.

The test is repeated two times for model 26H and three for model 29E as reported in Table 5.3.

Table 5.3.   Tests performed

Test name	Date	Battery used
Test1_26H	11-10	26H
Test2_26H	30-11	26H
Test3_29E	5-12	29E
Test4_29E	16-12	29E
Test5_29E	21-12	29E

5.2   Experimental result

During the tests temperature and pressure of the sample and their change rate are recorded against time. The data obtained for all the tests are here analysed and compared.

5.2.1   Temperature

One of the most important and meaningful parameter is the variation of temperature over time. Through this plot, in fact, it is possible to detect the Thermal Runaway (TR) trigger due to the rapid increase of temperature.

The two tests performed with the model 26H, Test1_26H and Test2_26H, are represented in blue and red respectively in Figure 5.3 on the following page.

In both tests the abuse temperature was set to be 20 °C and, as the samples were already at that temperature, the tests started immediately. From Figure 5.3 on the next page is possible to evidence that in both test the temperature increase sharply in a very limited time. In particular during Test1_26H the temperature reached the maximum value of 37.5 °C in 1.7 min, while in Test2_26H the maximum
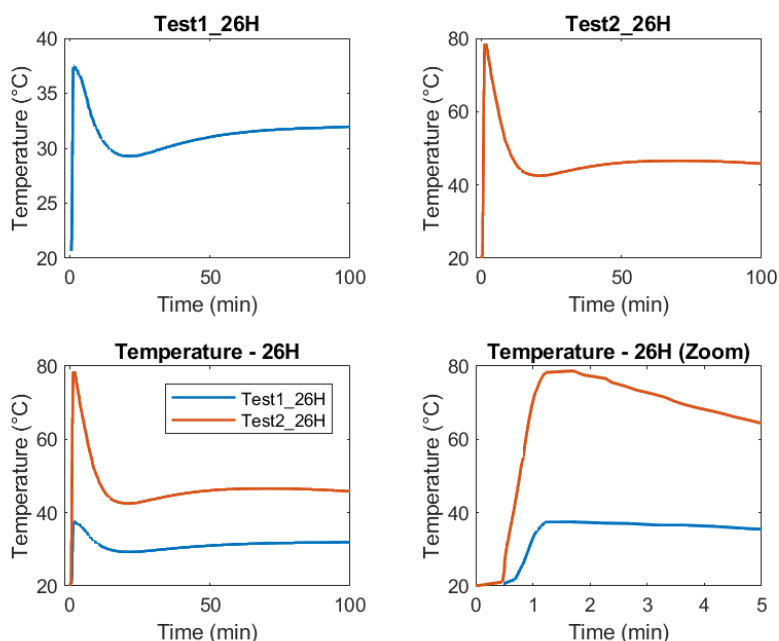
Figure 5.3.   Battery 26H results in terms of temperature. The cumulative plot are plotted with two different zoom states to better analyse the differences

temperature was higher, about 78.7 °C, reached in the same time. In both cases the battery has not exploded and TR is not detected, just Joule heat due to the ISC. After the peak is reached, the battery starts to cool down and the temperature decreases. However, as the ARC does not perceive any reactions, it enters again in the "heat-wait-seek" mode and the temperature increases due to the heat step produced by the ARC. It is important to notice that this is not linked to the test performed but only to the operation mode of the equipment.

Same graph has been plotted for the three tests performed with the battery 29E in Figure 5.4 on the following page. With respect to the results obtained with the battery 26H, the maximum temperatures achieved in these tests are one order of magnitude higher: 469 °C, 584.3 °C and 753.5 °C for Test3_29, Test4_29, and Test5_29E respectively. The plots show a sharp increase after about a second, followed by a rapid decrease until a plateau is reached. In particular, Test3_29E and Test4_29E (blue and red respectively in the plot) are very similar in shape: temperature increases sharply, then seems to slow down but then increases rapidly again reaching its peak in about 1 min. On the other hand, temperature growth in Test5_29E is slightly faster and more severe, with no slowdown reaching its peak in 0.8 min.

It is clear that using the battery 29E, TR is detected and it caused the explosion of the battery in all three tests. The battery used in Test3_29E is reported in
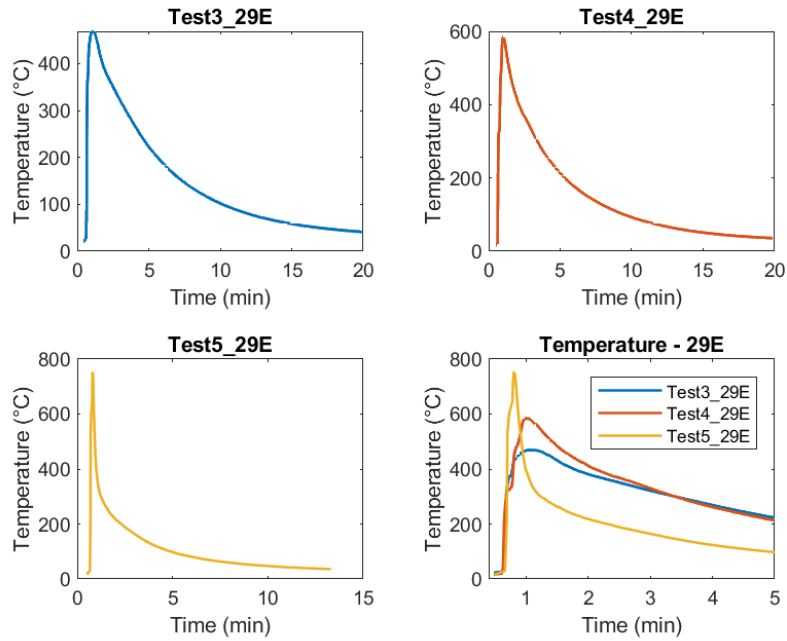
Figure 5.4.   Battery 29E results in terms of temperature

Figure 5.5 on the next page where it is possible to see the effects of the explosion and the high temperature reached. In particular, the external cover is not present and, around the penetration location, clear signs of explosion are present.

Comparing all the tests as done in Figure 5.6, it is clear that the temperatures reached by the 26H model (Test1_26H and Test2_26H in blue and red respectively) are lower than the one reached by the 29E. This is probably linked to the lower capacity of the 26H battery and to the safer separator.

Figure 5.5.   Photo of the battery 29E after nail penetration test was performed
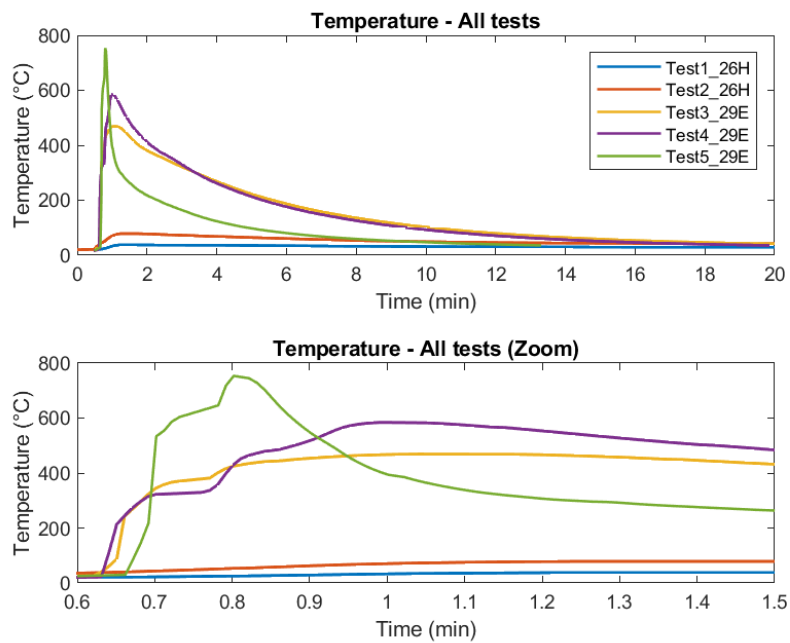
Figure 5.6.   Comparison of the temperature evolution in all the tests performed

5.2.2 Heat generated

It can be useful to analyse the presence of TR also evaluating the heat generated (W) during the test. This can be evaluated as:

$$Q = c_p \cdot \rho \cdot T_{rate} \cdot V \tag{5.1}$$

where T_{rate} is is the temperature rate expressed in K/s, the heat capacity c_p in J/kg/K, the density ρ in kg/m^3 and the volume V (m^3), calculated knowing that the batteries belong to the 18650 standard. The battery properties, heat capacity and density, are evaluated knowing the volume percentages of each component as done for evaluating the bulk properties in the model (see Chapter 7 on page 67 for more details). As the exact composition is known only for the 29E battery, same properties are considered for both batteries.

In Figure 5.7, the heat exchanged during the tests performed with the battery 26H are reported. As for the temperature plot, the heat generated rapidly increase right after the penetration. However, more fluctuations are present with respect to the temperature plots.
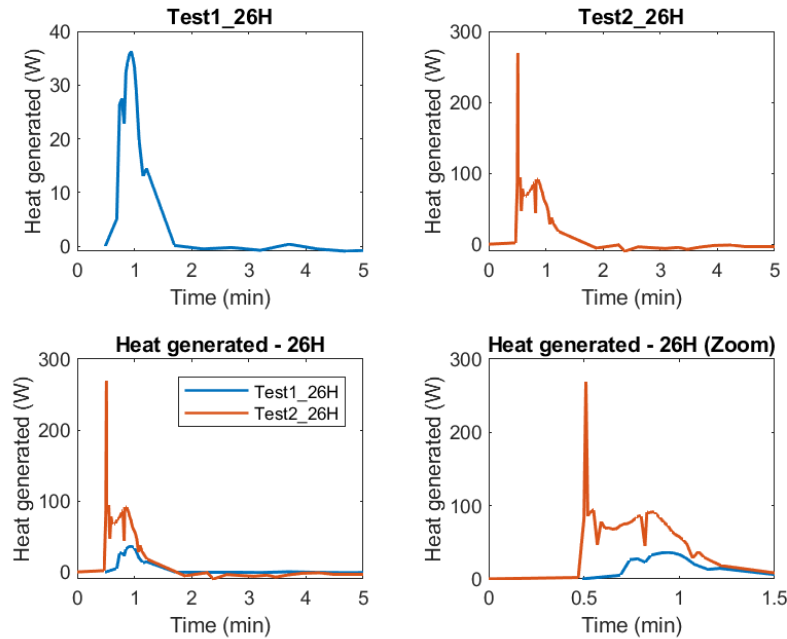
Figure 5.7.   Heat generated during the two tests performed with battery 26H

The heat generated by the battery 29E are obviously much higher, but similar in shape as reported in Figure 5.8 on the following page.
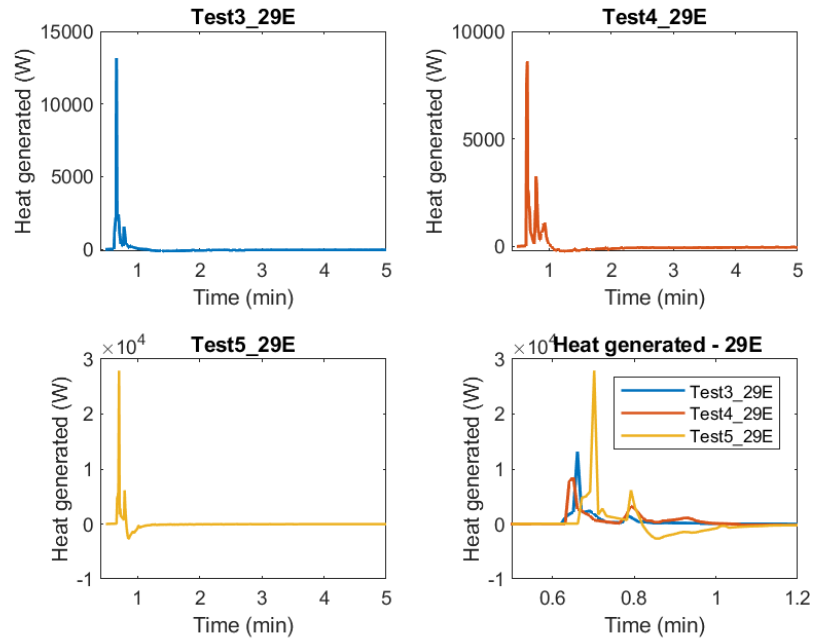
Figure 5.8. Heat generated using te battery 29E

5.2.3 Pressure

The results in terms of pressure, they are very diverse, both among the batteries in among the tests. In fact, while in the case of temperature the curves' trend is similar, representing the trend of pressure over time, strong fluctuations can be observed in both batteries as shown in Figure 5.9 and Figure 5.10 on the next page.

In particular, analysing battery 26H (Figure 5.9), the plot shows a pick after the penetration around 2 bar in the first test, and 3 bar in the second one, followed by a fluctuation. Comparing the timing of the peaks with the temperature trend, it is possible to notice that both pressure peaks are present when the temperature starts rising.

Differently in the battery 29E, tests Test3_29E and Test5_29E present rapid changes followed by an almost stable state. On the other hand, test Test4_29E shows a dramatic increase of pressure to a maximum value of 3.57 bar. However, looking at the zoomed image the behaviour of the cell seems to be strange due to to the constant value for three successive time steps (from 0.701 min to 0.771 minute).

56
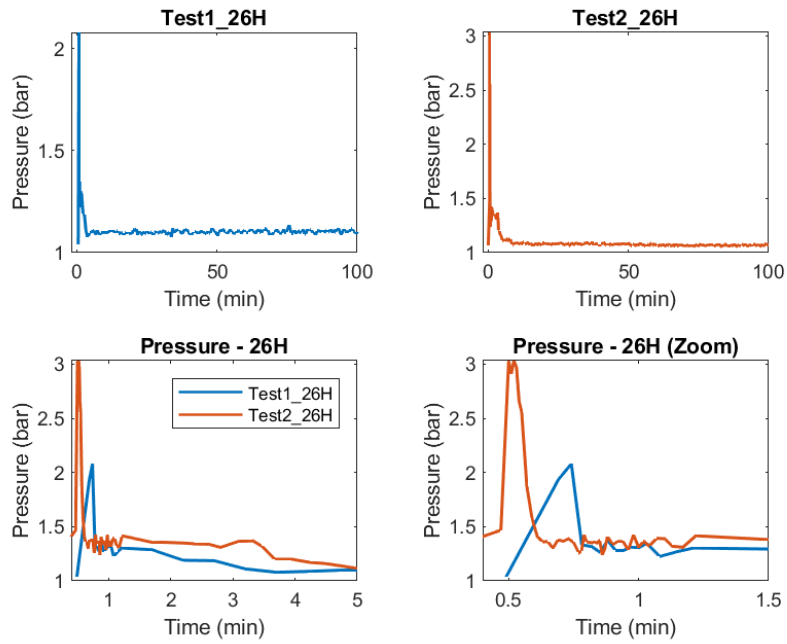
Figure 5.9.   Pressure over time in the different tests performed with battery 26H
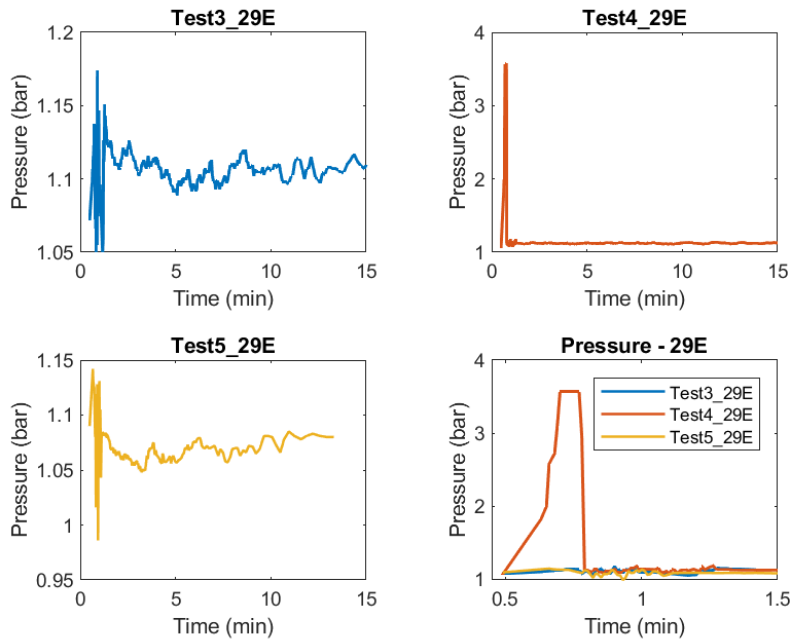
Figure 5.10.   Plot of pressure over time in the case of battery 29E

Part III

Nail penetration modeling

Chapter 6

Model theory

6.1 Governing equations

6.1.1 P2D equations and boundary conditions

The Pseudo-two-dimensional (P2D) model is based on the porous electrode theory: the electrodes active materials (solid phase) are modelled as spherical particles, and both electrodes and separator are wetted by electrolyte (liquid phase). The equations in the electrolyte are based on the concentrated solution theory. Consequently, the governing equations for each electrode are:

- Mass conservation in both solid and liquid phase,

- Charge conservation in both phases,

- Charge transfer reaction at the interphase.

On the other hand, the separator is represented by the mass and charge conservation in the liquid phase, but still taking into account its porosity. Consequently, the model is described by a total of twelve fully coupled partial differential equations.

The model dependent variables are:

- the electrolyte potential ϕ_l (V),

- the electric potential $\phi_{s,i}$ (V),

- the electrolyte salt concentration c_l ($\mathrm{mol\,m^{-3}}$) and,

- the concentration of lithium in the electrode particles $c_{s,i}$ ($\mathrm{mol\,m^{-3}}$).

Mass conservation in the solid phase

Mass conservation in the solid electrodes is described by second Fick's law for spherical particles as reported in Equation 6.1:

$$\frac{\partial c_{s,i}}{\partial t} = \frac{D_{s,i}}{r_{p,i}^2} \frac{\partial}{\partial r_{p,i}} \left(r_{p,i}^2 \frac{\partial c_{s,i}}{\partial r_{p,i}} \right) \tag{6.1}$$

where

- $c_{s,i}$ $(\mathrm{mol\,m^{-3}})$ correspond to the concentration of solid particles in the electrode i, where $i = p, n$ specifying whether the positive (p) or negative (n) one,

- $D_{s,i}$ $(\mathrm{m^2\,s^{-1}})$ is the solid phase diffusion coefficient,

- $r_{p,i}$ (m) is the positive or negative electrode particle radius.

In order to solve the different partial derivative equations, boundary conditions are necessary. In particular, to solve Equation 6.1, the following boundary conditions should be applied:

- Initial concentration set to solve the time dependent problem

$$c_{s,i}(t = t_0) = c_{s,i,0} \tag{6.2}$$

- Null net flux through the center of the particle, due to radial symmetry in the lithium concentration in the particles

$$\left. \frac{\partial c_{s,i}}{\partial r} \right|_{r=0} = 0 \tag{6.3}$$

- Mass flux at the outer surface of the particle equal to j_i by definition:

$$\left. D_{s,i} \frac{\partial c_{s,i}}{\partial r} \right|_{r=r_{p,i}} = -j_i \tag{6.4}$$

where j_i $(\mathrm{mol\,m^{-2}\,s^{-1}})$ is the pore wall mass flux, caused by the electrochemical insertion reactions. This is evaluated through the Butler-Volmer kinetics equation (see Equation 6.16 on page 63). The pore-wall flux can also be found in literature expressed as reaction current j^{Li} $(\mathrm{A\,m^{-3}})$ evaluated as

$$j^{Li} = \frac{\partial i_l}{\partial x} = a_{s,i} F j_i \tag{6.5}$$

where $a_{s,i}$ $(\mathrm{m^2\,m^{-3}})$ is the surface area per unit coefficient (or specific interfacial area) that is evaluated for spherical particle as

$$a_{s,i} = \frac{3\varepsilon_{s,i}}{r_{p,i}} \tag{6.6}$$

where $\varepsilon_{s,i}$ is the solid phase volume fraction.

Mass conservation in the electrolyte

A different equation is necessary to express the mass conservation in the electrolyte. In particular, as reported in Equation 6.7:

$$\varepsilon_{l,i}\frac{\partial c_l}{\partial t} = D_{l,eff}\frac{\partial}{\partial x}\left(\varepsilon_{l,i}\frac{\partial c_l}{\partial x}\right) + \frac{1-t_+}{F}j^{Li} \tag{6.7}$$

where

- $\varepsilon_{l,i}$ (-) is the electrolyte phase volume fraction or porosity, $i = p, n, s$ to indicate the positive (p) and negative (n) electrodes and the separator (s),

- c_l ($\mathrm{mol\,m^{-3}}$) is the electrolyte salt concentration,

- $D_{l,eff}$ ($\mathrm{m^2\,s^{-1}}$) is the effective electrolyte diffusivity, that is used instead of the bulk value to account for tortuosity. It is evaluated from the bulk diffusivity using Bruggeman correlation:

$$D_{l,eff} = D_l\varepsilon_{l,i}{}^{brug} \tag{6.8}$$

where *brug* is the Bruggeman's exponent, usually assumed to be equal to 1.5,

- t_+ (-) transport number that describe the fraction of the total current carried by electrolyte positive ions ($\mathrm{Li^+}$),

- F is the Faraday constant equal to $96\,485\,\mathrm{C\,mol^{-1}}$.

The boundary condition for the mass conservation in the electrolyte (Equation 6.7) is to ensure no mass flux of lithium ions through the electrolyte at cell boundaries (at the boundary of the electrolyte domain, which means in the contact between electrodes and current collectors):

$$\left.\frac{\partial c_l}{\partial x}\right|_{x=L_{neg,cc}} = \left.\frac{\partial c_l}{\partial x}\right|_{x=L_{cell}-L_{pos,cc}} = 0 \tag{6.9}$$

and to set an initial value for the electrolyte salt concentration to solve for the time dependent problem:

$$c_l(t=t_0) = c_{l,0} \tag{6.10}$$

Charge conservation in the solid phase

The charge conservation in the electrode (solid phase) is expressed as:

$$\varepsilon_{s,i}\sigma_{s,i,eff}\frac{\partial^2\phi_{s,i}}{\partial x^2} = -j^{Li} \tag{6.11}$$

where

- $\phi_{s,i}$ (V) is the electric potential,

- $\sigma_{s,i,eff}$ (S m^{-1}) is the effective conductivity, that takes into account the porosity of the medium. This is calculated through the Bruggeman correlation as done for the diffusivity:

$$\sigma_{s,i,eff} = \sigma_s \varepsilon_s^{brug} \tag{6.12}$$

where σ_s (S m^{-1}) is the bulk conductivity, $\varepsilon_{s,i}$ (-) is the solid phase volume fraction and *brug* is the Bruggeman exponent, even in this case usually assumed to be equal to 1.5.

To solve the charge conservation in the solid phase different boundary conditions are necessary [60]:

- As the electron movement is possible only between the electrodes and the current collectors, and not between electrodes and separator (that only support ionic conductivity), the current at that interface is equal to the total current. Which means for negative and positive interface:

$$\left.\frac{\partial \phi_{s,i}}{\partial x}\right|_{x=L_{neg,cc}} = \left.\frac{\partial \phi_{s,i}}{\partial x}\right|_{x=L_{cell}-L_{pos,cc}} = -\frac{i_{app}}{A_{cell}\sigma_{s,i,eff}} \tag{6.13}$$

- For the same reasoning, it is null at the interface with the separator:

$$\left.\frac{\partial \phi_{s,i}}{\partial x}\right|_{x=L_{neg,cc}+L_{neg}} = \left.\frac{\partial \phi_{s,i}}{\partial x}\right|_{x=L_{cell}-L_{pos,cc}-L_{pos}} = 0 \tag{6.14}$$

Charge conservation in the liquid phase

Charge conservation in the electrolyte, instead, is expressed as:

$$i_l = -\sigma_{l,eff} \cdot \nabla \phi_l + \frac{2\sigma_{l,eff}RT}{F} \cdot \left(1 + \frac{\partial ln f_i}{\partial ln c_l}\right) \cdot (1 - t_+) \cdot \nabla ln c_l \tag{6.15}$$

where

- i_l (A m^{-2}) current density in the liquid phase,

- $\sigma_{l,eff}$ (S m^{-1}) is the effective electrolyte conductivity avaluated through the Bruggeman correlation,

- ϕ_l (V) is the electrolyte potential,

- R is the ideal gas constant equal to $8.314 \, \text{J K}^{-1} \, \text{mol}^{-1}$,

- T (K) is the absolute temperature,

- f_i (-) is the mean molar activity coefficient, and $\frac{\partial ln f_i}{\partial ln c_l}$ is called activity dependence and it is used to modify the ion activity.

For the boundary conditions the reasoning is opposite to what done for the charge conservation in the solid, as it considers the ionic conductivity instead of the electric one. Therefore, the ionic current is null at the boundary between electrode and current collectors, and equal to the total current at the interface with the separator.

Charge transfer reaction

The electrochemical reactions take place at the interphase between solid and liquid phases, as described by the Butler-Volmer kinetic equation (Equation 6.16).

$$j^{Li} = a_{s,i} i_0 \left[exp \left(\frac{\alpha_a \cdot F \cdot \eta}{RT} \right) \right] - \left[exp \left(\frac{\alpha_c \cdot F \cdot \eta}{RT} \right) \right] \tag{6.16}$$

where

- α (-) is the charge transfer coefficient assumed to be equal to 0.5 for both anode (a) and cathode (c), as $\alpha_a = 1 - \alpha_c$,

- η (V) is the surface overpotential, evaluated as:

$$\eta = \phi_{s,i} - \phi_l - E_{eq} \tag{6.17}$$

  - $\phi_{s,i}$ (V) is the electrode potential,
  - ϕ_l is the potential in the electrolyte,
  - E_{eq} represent the equilibrium potential (often named U).

- i_0 (A m^{-2}) is the exchange current density, evaluated as

$$i_0 = i_{0,i,ref} \left(\frac{c_{s,i}}{c_{s,i,ref}} \right)^{\alpha_c} \left(\frac{c_{s,i,max} - c_{s,i}}{c_{s,i,max} - c_{s,i,ref}} \right)^{\alpha_a} \left(\frac{c_l}{c_{l,ref}} \right)^{\alpha_a} \tag{6.18}$$

  where

  - $i_{0,i,ref}$ (A m^{-2}) is the reference exchange current density,
  - $c_{s,i}$ (mol m^{-3}) correspond to the concentration of solid particles in the electrode i, where $i = p, n$ specifying whether the positive (p) or negative (n) one,
  - c_l (mol m^{-3}) corresponds to the concentration of lithium ion in the electrolyte solution,
  - $c_{s,i,max}$ (mol m^{-3}) is the maximum concentration in the solid phase, which means that ($c_{s,i,max} - c_{s,i}$) expresses the variation of unoccupied sites [61],
  - $c_{s,ref}$ is the reference concentration evaluated as half of the maximum ($0.5 c_{s,i,max}$),
  - $c_{l,ref}$ is the reference value in the liquid phase, setted as input.

6.1.2   Thermal equations

The governing equation for the thermal model can be written as

$$\rho_i c_{p,i} \frac{\partial T}{\partial t} = \nabla \cdot (k_i \nabla T) + q_{gen} + q_{TR} \tag{6.19}$$

where ρ_i ($\mathrm{kg\,m^{-3}}$) is the density, $c_{p,i}$ ($\mathrm{J\,kg^{-1}\,K^{-1}}$)the specific heat capacity, T (kelvin) the temperature and k_i ($\mathrm{W\,m^{-2}\,K^{-1}}$) the thermal conductivity of the material. As the material is defined as a bulk material (lumped) these properties are volume averaged as will be described in the next chapter.

The first term at the right side of Equation 6.19 represents the heat conduction in the battery, while the generic term q_{gen} ($\mathrm{W\,m^{-3}}$) represents the heat generation rate inside the battery. This term comprises different components:

$$q_{gen} = q_{react} + q_j + q_{mix} \tag{6.20}$$

To better understand, each component is analysed separately:

- Heat of reaction q_{react} ($\mathrm{W\,m^{-3}}$): it is the heat generated at the interface between solid and liquid due to the intercalation and de-intercalation processes. It can be divided into a reversible q_{rev} and an irreversible contributions q_{irrev}.

  - Irreversible reaction heat q_{irrev} ($\mathrm{W\,m^{-3}}$): it represents the deviation of the cell potential from its equilibrium value due to electrochemical processes. It is often also called activation heat.

  $$q_{irrev} = j^{Li} \cdot \eta = j^{Li} \cdot (\phi_{s,i} - \phi_l - E_{eq}) \tag{6.21}$$

  - Reversible heat q_{rev} ($\mathrm{W\,m^{-3}}$): it is also called entropy heat as it is caused by entropy changes during the intercalation and de-intercalation precesses.

  $$q_{rev} = j^{Li} \left(T \frac{\partial U}{\partial T} \right) \tag{6.22}$$

- Joule heat q_j ($\mathrm{W\,m^{-3}}$): it is caused by charge transport in the solid and liquid phase

$$q_j = -(i_s \cdot \nabla \phi_{s,i} + i_l \cdot \nabla \phi_l) \tag{6.23}$$

- Heat of mixing q_{mix} ($\mathrm{W\,m^{-3}}$): it is associated with concentration gradients. This is usually negligible, but it has been in included and calculated as:

$$q_{mix} = -j_i \cdot \left(-F \frac{E_{eq,therm}}{dc_{s,i} \nabla c_{s,i}} \right) \tag{6.24}$$

$E_{eq,therm}$ is the thermoneautral voltage (V) that is defined as:

$$E_{eq,therm} = E_{eq} - T \frac{dE_{eq}}{dT} \tag{6.25}$$

6.1.3 Thermal runaway equations

In order to simulate the exothermic reaction generated by the increase of temperature, then leading to TR, the mathematical theory of combustion is used [88]. In particular the *Constant fuel model*: it is a simplification *Solid fuel model* obtained by neglecting the spatial variations. This approach has been used in a variety of studies in literature [88, 89, 90, 91] and even for nail penetration as done by Chiu et al. [92] and Shelke et al. [93]. The volumetric heat is evaluated according to an Arrhenius-type law:

$$q_i = H_i W_i R_i \tag{6.26}$$

where q_i is the volumetric heat generated by the i-th reaction, H $(\mathrm{J\,kg^{-1}})$ is the specific heat release, W $(\mathrm{kg\,m^{-3}})$ is the volume-specific active material content and R $(\mathrm{s^{-1}})$ is the rate of reaction.

The following reactions are considered according to literature [88, 89, 90, 91, 92, 93]:

- **SEI decomposition**: the Solid Electrolyte Interface (SEI) layer is a protective layer that prevents the direct contact between anode and electrolyte. As temperature increases, it decompose exothermically, as expressed by the following equations.

$$q_{SEI} = H_{SEI} W_c R_{SEI} \tag{6.27}$$

$$R_{SEI} = A_{SEI} exp\left[-\frac{E_{SEI}}{RT}\right] c^*_{SEI} \tag{6.28}$$

$$\frac{dc^*_{SEI}}{dt} = -R_{SEI} \tag{6.29}$$

  where W_c $(\mathrm{kg\,m^{-3}})$ is the volume-specific carbon content in the anode, A $(\mathrm{s^{-1}})$ is the frequency factor, E $(\mathrm{J\,mol^{-1}})$ is the activation energy, R is the gas constant and T (K) is the battery temperature.

- **Anode-electrolyte reaction**: at elevated temperatures, an exothermic reaction between intercalated lithium and electrolyte can causes the formation of a secondary SEI layer.

$$q_{ne} = H_{ne} W_c R_{ne} \tag{6.30}$$

$$R_{ne} = -A_{ne} exp\left[-\frac{E_{ne}}{RT}\right] exp\left[-\frac{z}{z_0}\right] c^*_{ne} \tag{6.31}$$

$$\frac{dc^*_{ne}}{dt} = -R_{ne} \tag{6.32}$$

z is the SEI layer dimensionless thickness and z_0 is the initial thickness of the SEI layer. Its temporal change is expressed as:

$$R_{ne} = \frac{dz}{dt} \tag{6.33}$$

- **Cathode-electrolyte reaction**: is an auto-catalytic reaction [91]. In the oxidized state, the positive material reacts directly with the electrolyte. Or, the positive active material can decompose exothermically and emit oxygen that can react exothermically with the electrolyte. In any case, the chemical reduction of the positive active material with the electrolyte is highly exothermic [90].

$$q_{pe} = H_{pe}W_p R_{pe} \tag{6.34}$$

$$R_{pe} = -A_{pe}exp\left[-\frac{E_{ne}}{RT}\right] \cdot \alpha_r(1 - \alpha_r) \tag{6.35}$$

$$R_{pe} = \frac{d\alpha_r}{dt} \tag{6.36}$$

- **Electrolyte decomposition**: at even higher temperatures, the electrolyte starts decomposing exothermically.

$$q_e = H_e W_e R_e \tag{6.37}$$

$$R_e = -A_e exp\left[-\frac{E_e}{RT}\right] c^*_e \tag{6.38}$$

$$R_e = -\frac{dc^*_e}{dt} \tag{6.39}$$

Accordingly, the term q_{TR} in Equation is evaluated as the sum of the previous contributions:

$$q_{TR} = q_{SEI} + q_{ne} + q_{pe} + q_e \tag{6.40}$$

Chapter 7

COMSOL Multiphysics® model implementation

7.1 Model structure

The aim of the model is to simulate a nail penetration test and the consequent TR reactions happening in a NMC cylindrical cell, with the purpose of matching the experimental results from Chapter . In particular, the battery INR18650-29E results as it is the one where TR is detected. The model has been implemented into COMSOL Multiphysics® software v6.0 using the Battery Design Module functionalities coupled to the Heat Transfer in Solids interface.

The model consists of a coupled P2D electrochemical-3D thermal.
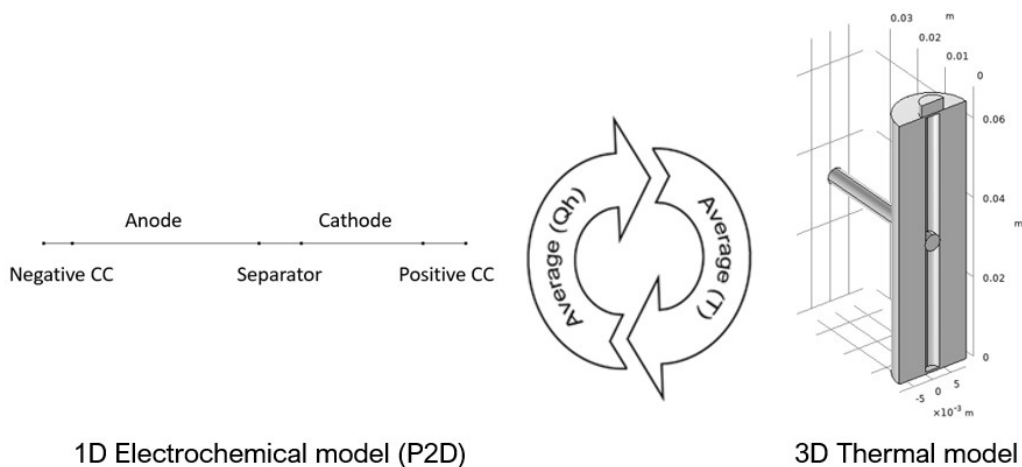
Figure 7.1. Schematic representation of the model structure, the two components and how they are coupled

As reported in Figure 7.1 on the previous page 1D component is used to solve the P2D model, while a 3D component solves for the thermal equations. This separation between electrochemical and thermal equations is carried out to obtain faster computational times with lower CPU requirements with respect to a fully 3D electrochemical-thermal model. The two components are coupled using the average heat generation rate from the 1D model as input in the 3D model. Whilr, average temperature from the 3D thermal model is used as input in the 1D model as temperature influences different properties.

The presence of the two components is translated in COMSOL as reported in Figure 7.2. *Component 1 (comp1)* is the 1D component where theP2D model is represented by the *Lithium-Ion Battery (liion1)* physics interface. In this component the nail penetration is simulated through a rapid decrease of the potential at the positive terminal, from the maximum charging value to ground. The *Component 2 (comp2)* is the 3D component used to simulate heat propagation in the battery through *Heat Transfer in Solid and Fluids (ht)*. Half of the battery is modelled to reduce the computational burden.

The study is carried out with a first current initialization step followed by the transient (time dependent) step.
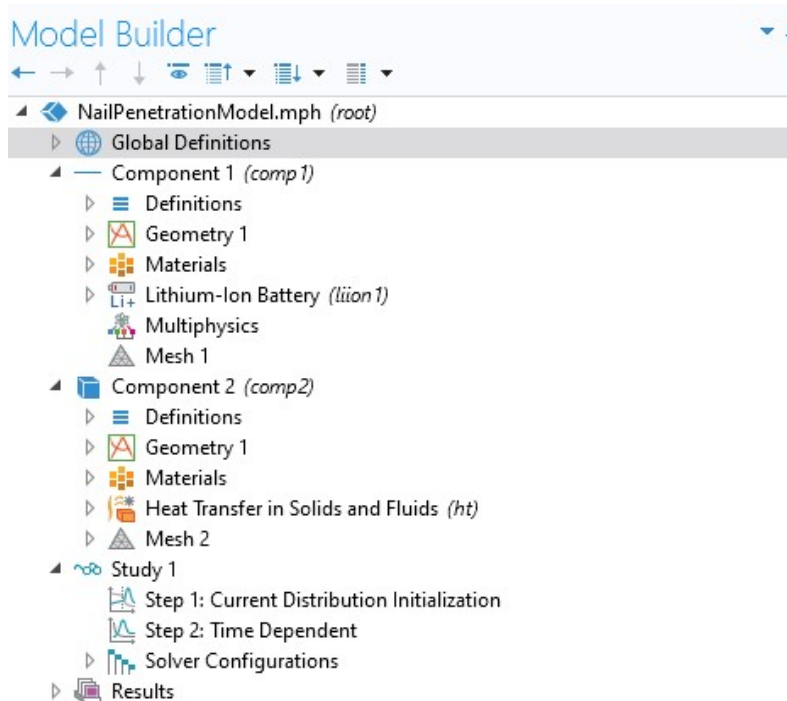
Figure 7.2. COMSOL model builder. The two components and the physics they solve for

In this chapter, the implementation details will be carried out, considering all the

input data, in terms of geometry and material properties. As seen in Chapter 4.2 on page 40, many input parameters are required in the P2D model, and here the selection will be presented.

7.2 Component 1 - 1D

7.2.1 Geometry

The 1D electrochemical model is composed of two current collectors, two electrodes and the separator. The geometry parameters are shown in Table 7.1. These values have been taken from Park et al. [94] as they simulate the same Samsung battery as in this model (Samsung INR18650-29E).

Table 7.1. 1D geometry parameters

Parameter	Description	Value	Unit
$L_{neg,cc}$	Negative current collector thickness	10×10^{-6}	m
L_{neg}	Negative electrode thickness	66×10^{-6}	m
L_{sep}	Separator thickness	15×10^{-6}	m
L_{pos}	Positive electrode thickness	43×10^{-6}	m
$L_{pos,cc}$	Positive current collector thickness	15×10^{-6}	m

According to this the length of the cell L_{cell}, equal to the sum of the lenght of each component is equal to 149×10^{-6} m

7.2.2 Cell materials

As it is possible to see in Table 5.2 on page 48, the cell is made of graphite anode, NMC cathode, $LiPF_6$ salt in different organic carbonates solvents as electrolyte, and the two current collector in copper the negative one and in aluminium the positive. These materials are implemented in the model using COMSOL Multiphysics® material library, as it is possible to see in Figure 7.3 on the following page. The anode is included as standard Li_xC_6 graphite anode present in the material library. The positive electrode is assumed to be NMC 111 ($LiNi_{1/3}Mn_{1/3}Co_{1/3}O_2$). It is an assumption because in the material safety data-sheet of the battery [86], the cathode is generically expressed as $LiNi_aMn_bCo_cO_2$ with $0 < a < 1$, $0 < b < 1$ and $c = 1 - a - b$, and so the precise proportion between nickel, manganese and cobalt are unknown. Moreover, as different battery manufacturers use different binders and additive to improve the cathode performance, it is not possible to now the exact composition of the cell and so the proper properties. The liquid electrolyte is represented by $LiPF_6$ in a 3:7 mixture of EC and EMC. This is again

an assumption, as the exact organic solvents used are not known. The current collectors are implemented using the built-in material in COMSOL Multiphysics® library of copper and aluminium.

▲ 🔲 Materials
  ▷ 🔲 LiPF6 in 3:7 EC:EMC (Liquid, Li-ion Battery) *(mat1)*
  ▷ 🔲 Graphite, LixC6 MCMB (Negative, Li-ion Battery) *(mat2)*
  ▷ 🔲 NMC 111, LiNi0.33Mn0.33Co0.33O2 (Positive, Li-ion Battery) *(mat3)*
  ▷ 🔲 Aluminum *(mat9)*
  ▷ 🔲 Copper *(mat10)*
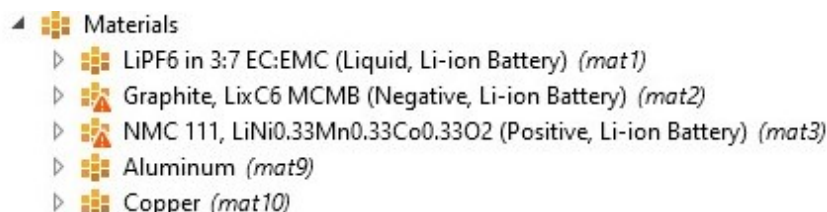
Figure 7.3. Material tab in COMSOL Multiphysics®

7.2.3 Electrochemical parameters

As seen in Capter 4.2 on page 40 about the required parameters of the P2D model, there are different property that are necessary for the model computation, that are reported in Table 7.2 on the following page. These properties and parameters are obtained from different sources, both from literature and COMSOL Multiphysics® material library. The values are chosen by comparing different sources and taking into account different aspects. A precise analysis is reported in the following:

Electric conductivity graphite conductivity is assumed to be $100\,\mathrm{S\,m^{-1}}$ as done in multiple references [50, 95, 96, 97]. Regarding the cathode, again the same value is considered as done in the different studies [95, 96]. Moreover Sacchetti [61] in his work tested different lower values with no significant changes. Electrical conductivities of aluminum and copper domains are straightforwardly obtained by the property of the material added from COMSOL Multiphysics® material library.

Electrolyte phase volume fraction (porosity) This value is really dependent on the battery chemistry and, even considering the same active material, binders and manufacturer production can play a considerable role. For this reason, a proper experimental analysis should be carried out. Not having this possibility, literature has been analysed [50, 94, 95, 96, 98]. The values from Park et al. [94] have been chosen as the same battery is modelled.

Electrode phase volume fraction This value has been obtained from the previous one considering:

$$\varepsilon_{s,i} = 1 - \varepsilon_{l,i} - \varepsilon_{b,i} \tag{7.1}$$

where $\varepsilon_{b,i}$ is added to take into account the presence of binders. This value has been assumed, due to lack of other data, as equal to 0.02.

Particle radius The particle radius in the electrodes is assumed to be constant in this model, as done in the majority of the studies [50, 88, 94, 95, 96]. The values however are quite different ranging from 2 to 12.5 μm for the graphite anode, and from 1 to 5.5 for the NMC cathode. Again, Park et al. [94] data is chosen.

A summary of the values chosen is reported in Table 7.2.

Table 7.2. Electrochemical properties

Property	Negative CC	Anode	Separator	Cathode	Positive CC
σ_i (S m^{-1})	5.99×10^7	100	–	100	3.77×10^7
$\varepsilon_{s,i}$ (-)	–	0.72	–	0.76	–
$\varepsilon_{l,i}$ (-)	–	0.26	0.39	0.22	–
i_{0ref} (A m^{-2})	–	36	-	26	–
$r_{p,i}$ (m)	–	8×10^{-6}	–	5.5×10^{-6}	–

7.2.4   P2D model implementation

In order to implement the P2D model in COMSOL Multiphysics® the Lithium-ion battery interface of the Battery design module is used as reported in Figure 7.4 on the following page.

In particular the following nodes are exploited:

- No Flux: it is a boundary condition added by default for all external boundaries to an electrolyte domain. In fact, it is set in the contact point with electrodes and current collectors, as it is possible to see in Figure 7.6 on page 73.

- Insulation: other boundary condition set by default that describes the boundaries of the cell that do not face a conductor, which means in this case the external boundaries of the current collectors.

- Initial Values: it sets the initial values for the electrolyte potential (ϕ_l), the electric potential ($\phi_{s,i}$), and the electrolyte salt concentration (c_l). The initial value for the electrolyte potential is set equal to minus the of the negative electrode material (graphite). The electrolyte salt concentration is set to a conventional value of $1000\,\mathrm{mol\,m^{-3}}$. The value for the electric potential differs for the anode and the cathode as they are set according to their boundary conditions: ground for the anode, initial voltage for the cathode.

- Porous Electrode: it is used to simulate the behaviour of both the anode and the cathode. The sub node *Particle intercalation* solves for the mass conservation,
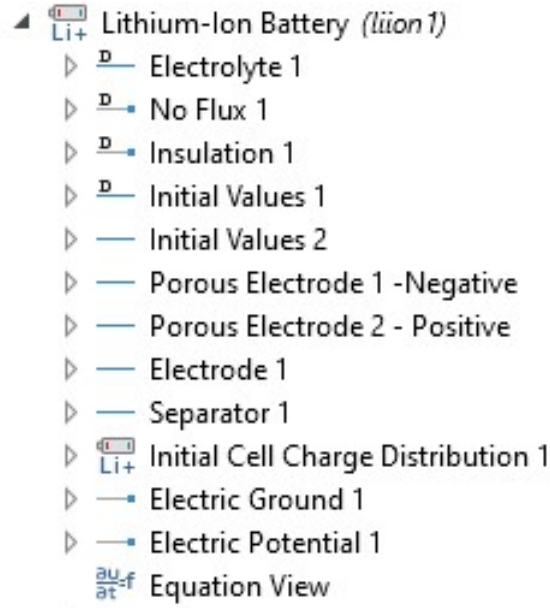
Figure 7.4. Model builder of the Lithium Ion Battery (liion1) interface

while *Porous Electrode Reaction* defines the electrode kinetics at the interface between the pore electrolyte and the electrode matrix.

- Electrode: is used to define an electrode domain that only conducts current in the electron conducting phase. For this reason, it is used to simulate both the negative and positive current collectors.

- Separator: it overrides the electrolyte domain. It is used to account for the lowered diffusion coefficients in the electrolyte and the lowered conductivities of the electrode, due to the lower volume fractions of each phase and the tortuosity of the porous matrix.

- Initial Cell Charge Distribution: it is a global node used to define the initial SOC of the battery.

- Electric ground: it sets the electric potential to zero at the negative terminal.

- Electric potential: this node is used to set the variation of the voltage at the positive terminal to simulate the nail penetration. The following function is used:

$$V_{sc} = E_{cell} \cdot \left[1 - max \left(step1 \left(\frac{t}{t_{ramp}} \right) \right) \right] \tag{7.2}$$

where *step1* is a smoothed step function from 0 to 1. The function V_{sc} is reported in Figure 7.5 on the following page
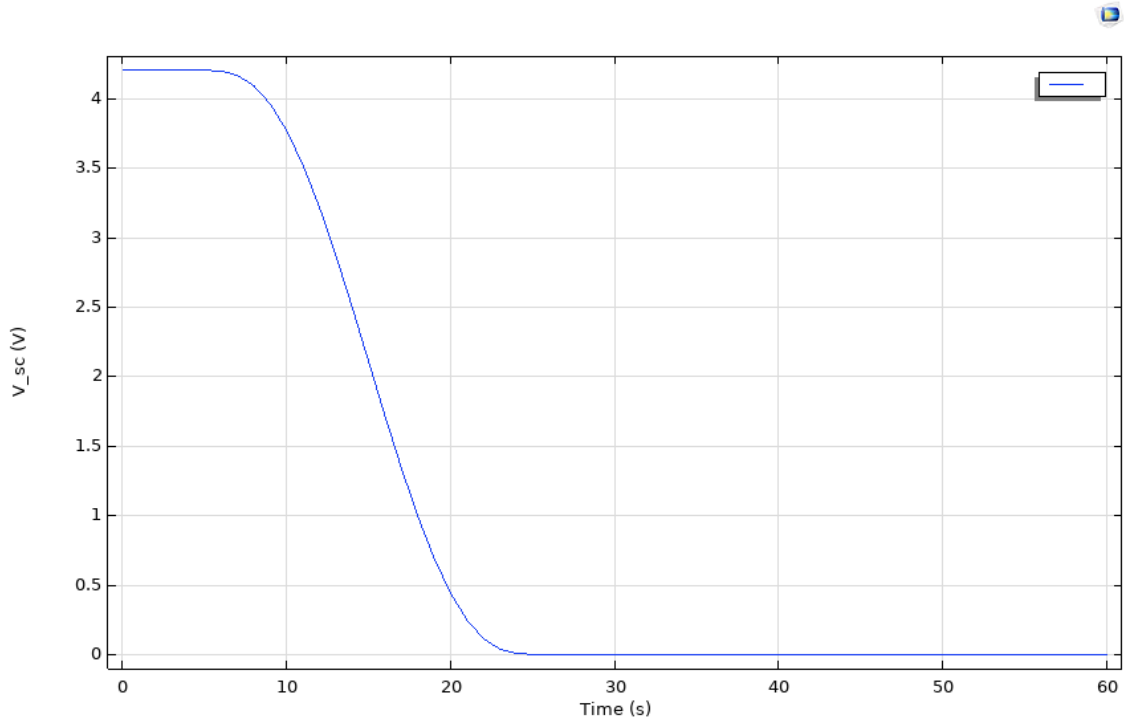
Figure 7.5.   Plot of the function used for the simulation of the nail penetration test

A summary of the boundary conditions and the initial values is reported in Figure 7.6.
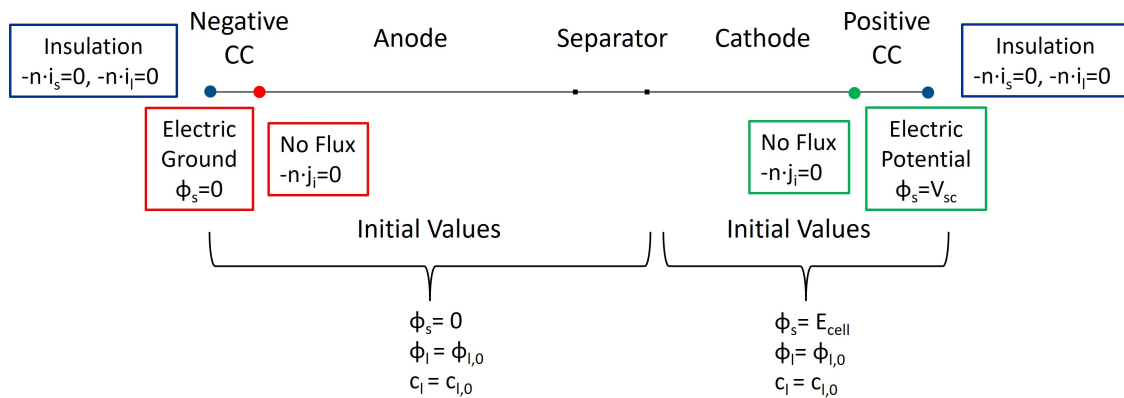
Figure 7.6.   Boundary conditions and initial values for the 1D electrochemical model

7.3 Component 2 - 3D

7.3.1 Geometry

To predict the thermal behaviour of the battery during the nail penetration test, a three-dimensional axisymmetric cylindrical battery model was constructed. As modeling a 3D multilayer model is computationally expensive, some assumption and simplification have been made. Firstly, only half of the battery has been simulated. Then, the cell was assumed to be a homogeneous bulk material.

The 3D battery model is composed of the active battery material, the can, the connector and the penetrated nail as reported in Figure 7.7
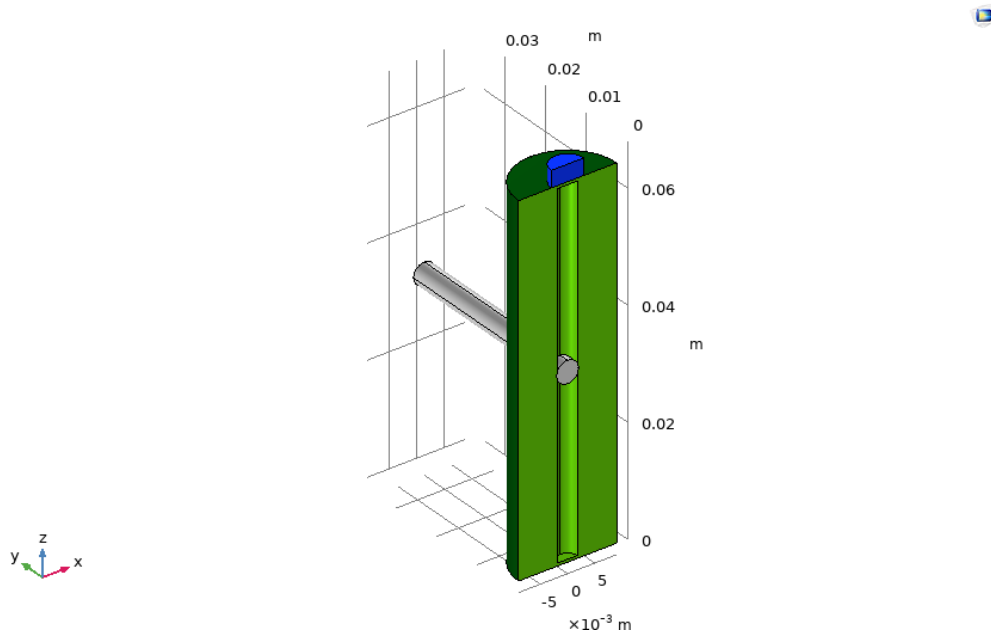
Figure 7.7. 3D Geometry. In green the active battery material, dark green the can, in blue the connector and in grey the nail

It is important to remark that in this model the nail does not have a direct role in the occurrence of the ISC, as this is only simulated in the 1D component. However, the nail can have role in the heat dissipation, and so it has been included for this reason.

7.3.2 Materials and properties

To evaluate the properties of the bulk material required to solve the thermal problem, it is necessary to firstly evaluate those properties for each component (ρ_i, $c_{p,i}$ and k_i).

For both current collectors, all properties have been assumed as equal to the values present in the COMSOL Multiphysics® material library as the differences with literature where minimal [50, 95, 96, 99, 100].

For the electrolyte properties only in [104, 105] the value is specified and this value is chosen even though it is different from the electrolyte chosen from the material library in the 1D component.

On the other hand, for anode, cathode, and separator, the values found in literature are quite diverse, so a detailed analysis is reported:

Density the value for the anode varies from 1200 to 2500 kg/m³ in literature [96, 99, 100, 69]. The value of 1220 $kg\,m^{-3}$ is present in two sources [50, 95], but it is way lower than the one reported in other sources that is around $2300\,kg\,m^{-3}$. For this reason this mean value has been chosen. For the cathode, it is not easy to find uniform values in literature. Disparity in the value is find due to the different proportion of nickel, manganese and cobalt not always specified and also due to the different synthesis method. For this reason is been decided to keep the value obtained from COMSOL Multiphysics® material library as done by other literature articles [95, 101]. For the separator the same problem occurs: not in all sources the composition is specified. Most of the sources agrees on a value of $900\,kg\,m^{-3}$ [99, 69, 102].

Heat capacity The values for graphite anodes heat capacity are very different among the various sources ranging from 623 to 1437.4 J/kg/K [50, 95, 96, 99, 100, 69, 55]. However in study [95], Wang et al. performed an experimental analysis so their value has been set. For the cathode, scarce literature is present, so COMSOL Multiphysics® the same reasoning as for the density is done. For the separator, the value ranges from 1978 to 2050 J/kg/K. As the difference is lower than for other cases, a mean value of $1971.5\,J\,kg^{-1}\,K^{-1}$ is set.

Thermal conductivity The values of thermal conductivity are those on which there is most disagreement among sources, either for anode, cathode and separator. For graphite two values are present: $6.5\,W\,m^{-1}\,K$ [99, 102] and $1.04\,W\,m^{-1}\,K$ [95, 69, 55, 88, 101]. The latter is set as it it the most used in more recent studies. Same reasoning is performed for the adoption of the value for the NMC cathode and the separator.

The cell homogeneous bulk material has an overall isotropic density and specific capacity determined by the volume composition of the battery simulated reported in Table 7.3 on the next page.

On the other hand, given the layered structure of the jelly roll in a cylindrical battery, anisotropic thermal conductivity is adopted. Its radial and angular values can be derived by the following equations [61, 90, 101]:

Table 7.3. Volume % of each component, excluding the contribution of unknown materials and the can. Data from [86]

Component	%
NMC cathode	44
Graphite anode	26
Separator	3
Aluminium	4
Copper	9
Electrolyte	14

$$k_{i,r} = \frac{L_{cell}}{\sum_i \frac{L_i}{k_i}} \tag{7.3}$$

$$k_{i,ang} = \frac{\sum_i L_i k_i}{L_{cell}} \tag{7.4}$$

The nail is made of AISI 316 stainless steel. As this is not implemented natively in the COMSOL Multiphysics® materials library, this is added as blank material to which the needed property are added manually from [103].

A summary of all the properties used for the evaluation, the nail and the final homogenous bulk material properties are reported in Table 7.4.

Table 7.4. Thermal properties

Component	ρ_i (kg m^{-3})	$c_{p,i}$ (J kg^{-1} K^{-1})	k_i (W m^{-2} K^{-1})
Negative CC	8960	385	400
Anode	2300	881	1.04
Separator	900	1971.5	0.334
Electrolyte	1290	133.9	0.45
Cathode	2500	1000	3.4
Positive CC	2700	900	238
Homogeneous bulk material	2828.7	810.79	$k_r = 54$ $k_{ang} = 4$
Nail	8000	500	16.3

7.4 Thermal runaway implementation

To implement the TR equations seen in the previous section, a *Domain ODEs and DAEs (dode)* interface is added. The parameters used are reported in Table 7.5 and the respective initial values in Table 7.6. The values for the cathode reactions are taken from sources where a NMC cathode is specified [104, 105]. For all the other values, accordance among sources is present [88, 89, 106, 101, 104, 105].

Table 7.5.   Exothermic reactions parameters

Reaction	H $(\mathrm{J\,kg^{-1}})$	W $(\mathrm{kg\,m^{-3}})$	A $(\mathrm{s^{-1}})$	E $(\mathrm{J\,mol^{-1}})$
SEI decomposition	2.57×10^5	610	1.14×10^{14}	1.35×10^5
Anode-Electrolyte	1.714×10^6	610	7.18×10^{13}	1.35×10^5
Cathode-Electrolyte	3.14×10^5	1120	6.66×10^{13}	1.41×10^5
Electrolyte decomposition	1.55×10^5	406.9	5.12×10^{15}	1.75×10^5

Table 7.6.   Exothermic reactions parameters

Variable	Initial Value
$c^*_{SEI,0}$ (-)	0.15
$c^*_{e,0}$ (-)	1
$c^*_{ne,0}$ (-)	0.75
z_0 (-)	0.033
α_{r0} (-)	0.04

7.5 Coupling implementation

In order to evaluate the heat sources from the 1D electrochemical model and use them as heat sources in the *Component 2*, it is necessary to use a *nonlocal coupling operator*. Thanks to that, it is possible to establish a connection between different parts of a model component or between different model components, as in this case. In particular, a scalar average operator (*aveop*) is used that computes the average of an expression over the source (the selected geometric entity or entities). For a generic quantity x:

$$x_{average} = \frac{\int x dl}{l} \qquad (7.5)$$

where l is the characteristic dimension.

Applying this to the specific case, a variable Qh is set in the second component as:

$$Qh = q_{gen} = nojac(comp1.aveop1(comp1.liion.Qh)) \tag{7.6}$$

where

- *aveop*1 is the average operator evaluated on the whole battery (L_{cell} as source),

- *comp*1.*liion*.*Qh* is the variable name of the heat generation rate (evaluated considering all the contribution listed in Equation 6.20 on page 64).

- *nojac* is an operator that prevent the fill-in of the Jacobian matrix due to the introduction of the nonlocal coupling operator, that would cause a considerable increase of CPU required to solve the problem. Using the [nojac] operator can slow down the convergence of the solution. For further explanation of this operator see the *Comsol Multiphysycs Reference Manual* [107].

Given the heat sources, the heat transfer module computes the heat balance, thus leading to the temperature distribution on the battery volume (*Component 2*). Its average value is used as model input, in the shared properties of the *Component 1* as:

$$T_{input} = nojac(comp2.aveop2(comp2.T)) \tag{7.7}$$

where *aveop*2 is the average operator over the active cell material.

On the other hand, once the temperature in the jell-roll exceeds the material decomposition triggering value, TR probably occurs [92]. For this reason, the maximum temperature value in the whole 3D component is used to probe for any temperature that can activate the thermal abuse reactions.

7.5.1 Second simulation

Another model is done and compared to the previous one (later called simulation1). The aim is to simulate the hotspot around the nail. To obtain this, the averaged heat generation rate from the 1D is given as input in the 3D model as boundary heat flux applied to the shorting area that is the contact area between the nail and the active battery homogenous material. In this case, the full battery is considered. The heat flux is evaluated considering that the volume heat rate is generated in the volume occupied by the nail, but is exchanged through the contact area [69].

$$q^{sc} = N_{st} \cdot \frac{\pi r_{nail}^2 l_{nail}}{2\pi r_{nail} l_{nail}} = \frac{1}{2} r_{nail} q_{gen} \ N_{St} \tag{7.8}$$

where N_{st} is evaluated as [69]:

$$N_{st} = 1 + \frac{v_{pn}t}{L_{cell}} \tag{7.9}$$

where v_{pn} is the penetration velocity, $v_{pn}t$ the displacement and L_{cell} the total length of the cell.

The thermal runaway equations are added in the same way as the previous.

7.6 Results and discussion

In Figure 7.8 it is reported the comparison of the temperature variation among the three tests done with the battery INR1865029E and the two simulated curve using COMSOL. In particular, *Simulation1* is the one that only considers volumetric heat generation rates, while in *Simulation2* the heat generation is exchanged as boundary heat flux. It is important to point out that, in order to properly compare the results, the simulation results have been plotted considering the same latency that is present in the experimental procedure. Moreover, only the first minute is plotted as the focus is on the peak temperature.
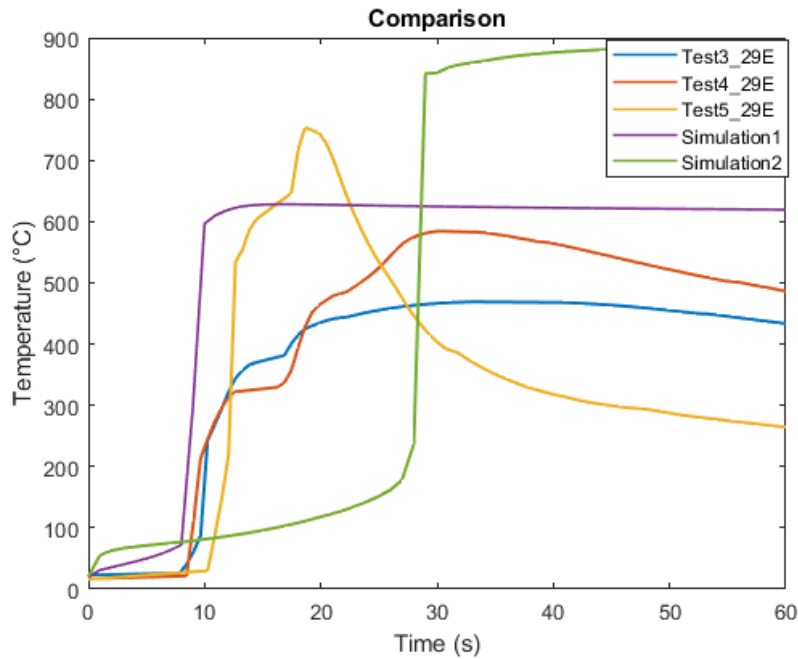
Figure 7.8. Comparison of the experimental data and the simulated temperature variation. *Simulation1* only considers volumetric heat generation rates, while in *Simulation2* the heat generation is exchanged as boundary heat flux.

Figure 7.8 on the preceding page shows that the *Simulation1* is in good agreement with the testing results in terms of predicting the starting time of the thermal runaway, around 7 s. However, it is less accurate in predicting the temperature trend and the maximum temperatures at the assigned locations. Nevertheless, the peak temperature is in the range achieved by the experimental tests.

On the other hand, *Simulation2* predicts the peak temperature timing of Test4 and Test5 (Test3 as already seen in the experimental part is faster). However, the peak temperature reached by this simulation, is higher than the experimental ones. This can be due to meshing problems (thin layers can increase border effects) and also due to the parameters used for the thermal abuse equations. In fact, looking at Figure 7.9 where the heat generation contributions are plotted, it is possible to see that the first 30 seconds are dominated by the heat flux, then thermal runaway reactions are predominant causing the spike in temperature. As a result, fitting the thermal abuse parameters can improve the accuracy.
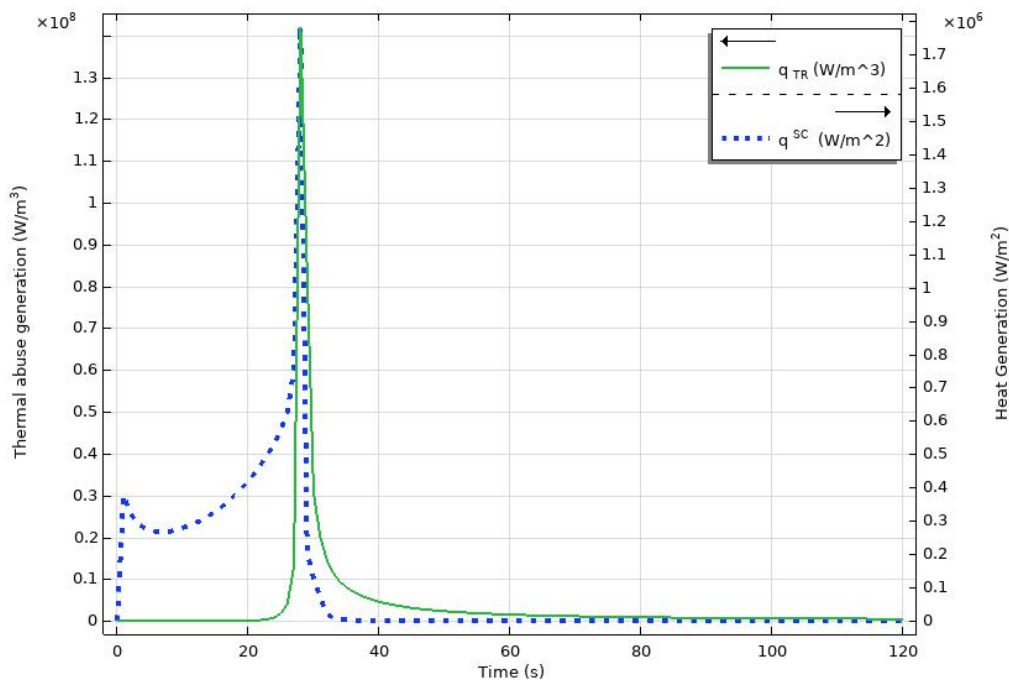
Figure 7.9. Heat generation in *Simulation2*, considering both contributions

The way this second simulation is formulated, a thermal gradient is present in the 3D model, as shown in Figure 7.10 on the following page. The temperature start increasing around the nail generating a hotspot. At around 30 s from the beginning time, the temperature is almost homogenous.
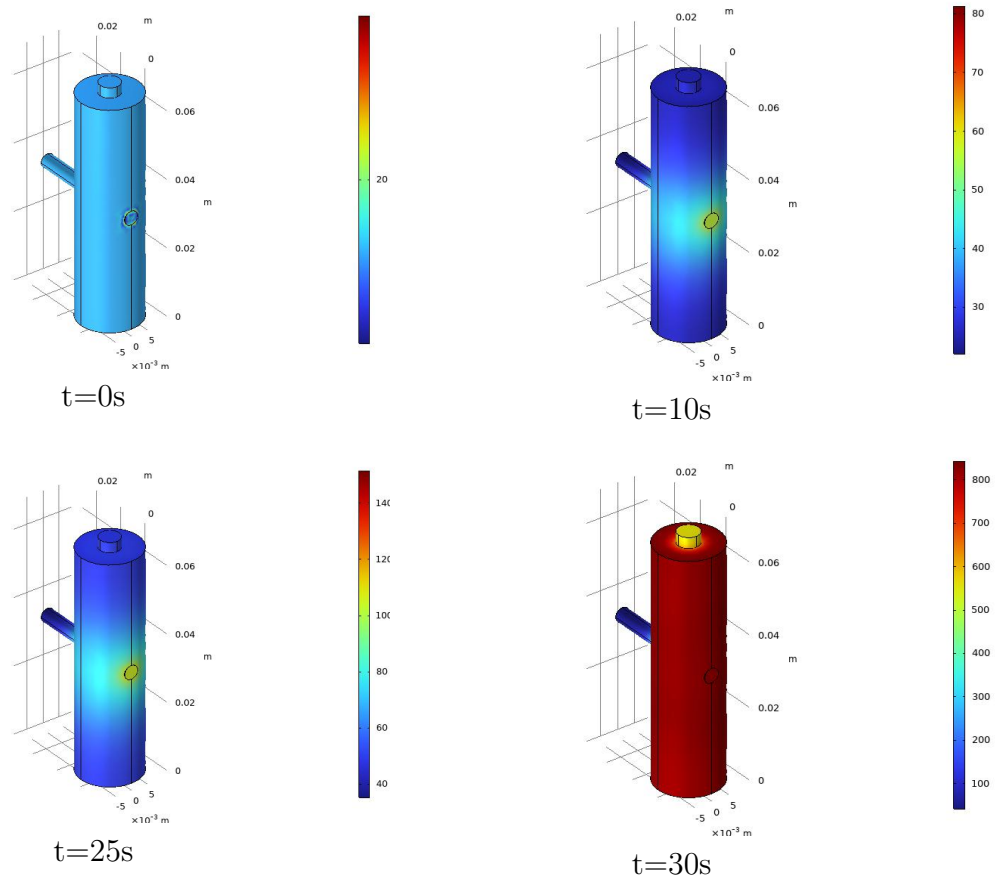
Figure 7.10.   Spatial temperature variation at different time steps

7.6.1   Possible improvements

A few limiting factors have impacted on the result of the presented study. First of all, some data is taken from datasheet that are not always complete. In fact, manufacturers don't share the complete composition of their batteries to protect their know-how. Materials research is a big investment and any improvement is kept secret. To obtain a better model, an experimental composition analysis is suggested to set the proper data in the model. For the same reason, some electrochemical parameters used as input for the P2D model could be investigated experimentally. Clearly, this approach would require more time and effort. Another possibility consists in using Neural Networks or other algorithms to set the values from experimental curves. In this case, knowledge in the field is required.

Another aspect that strongly influence the result is the function used for the simulation of the voltage drop. This is often measured during the nail penetration test, but the EV+ ARC provided by the Energy Center facility is not equipped with

this feature. Having the experimental curve and fitting would help in increasing the accuracy of the obtained results.

Finally, computational problems can be reduce by a proper user-controlled mesh and by using a higher computational memory device.

Chapter 8

Conclusions

Lithium Ion Batteries (LIBs) are expected to be the main energy source for many applications, and in particular for Electric Vehicles (EVs) (Battery Electric Vehicles (BEVs)). However, safety concern are present, especially in the event of external mechanical stress and the possible consequent TR. For this reason, many compulsory testing standards are required before assembling LIBs in cars, each including different abuse tests. Those tests are divided into mechanical, electrical and thermal.

Abuse testing is expensive as it requires proper equipment to be carried out. Moreover, most of them are destructive with the consequent waste of the battery tested that can be expensive in case of bigger battery packs. For this reason, development of mathematical models to better understand the behaviour of the batteries are a very important topic of literature research.

As nail penetration test is a common mechanical test used to obtain valuable information on the mechanical and thermal stability of the battery, the modeling of this test has been carried out in this work. In particular, the first simulation (*Simulation1*) only considers volumetric heat generation rates, both for chemical generation and thermal runaway reactions. In *Simulation2*, instead, the heat generation is exchanged as boundary heat flux at the shorting area, which means at the contact area between the nail and the homogenous bulk material.

Both simulations have been validated against experimental data, showing that is of paramount importance to model both electrochemical and thermal nature of the battery together, as they influence each other. The first simulation shows great accordance in predicting the starting time of the thermal runaway process. The trend of temperature variation is similar to the experimental results, but the model is less accurate in predicting the peaking point. The second one, is accurate in predicting the peak time, but a higher temperature is reached.

This work can be a starting point to develop a more accurate model (i.e., fully 3D model) using a suitable computational power. Future work should also focus on module and pack simulation to evaluate TR propagation.

Bibliography

[1] Liang, Yeru et al. «A review of rechargeable batteries for portable electronic devices». In: *InfoMat* 1.1 (2019), pp. 6–32. DOI: https://doi.org/10.1002/inf2.12000. eprint: https://onlinelibrary.wiley.com/doi/pdf/10.1002/inf2.12000.

[2] *Smartphone Ownership and Internet Usage Continues to Climb in Emerging Economies.* Pew Research Center. [Online; accessed 15-December-2022]. Feb. 2016. URL: https://www.pewresearch.org/global/2016/02/22/smartphone-ownership-and-internet-usage-continues-to-climb-in-emerging-economies/.

[3] *BS EN IEC 61851-1:2019 Electric vehicle conductive charging system. General requirements.* Standard. International Electrotechnical Commission, 2019.

[4] Yadlapalli, Ravindranath Tagore et al. «A review on energy efficient technologies for electric vehicle applications». In: *Journal of Energy Storage* 50 (2022), p. 104212. ISSN: 2352-152X. DOI: https://doi.org/10.1016/j.est.2022.104212.

[5] BloombergNEF. *Global Energy Storage Market Set to Hit One Terawatt-Hour by 2030.* Nov. 2021. URL: https://about.bnef.com/blog/global-energy-storage-market-set-to-hit-one-terawatt-hour-by-2030/.

[6] Zubi, Ghassan et al. «The lithium-ion battery: State of the art and future perspectives». In: *Renewable and Sustainable Energy Reviews* 89 (2018), pp. 292–308. ISSN: 1364-0321. DOI: https://doi.org/10.1016/j.rser.2018.03.002.

[7] BloombergNEF. *Lithium-ion Battery Pack Prices Rise for First Time to an Average of 151$/kWh.* Dec. 2022. URL: https://about.bnef.com/blog/lithium-ion-battery-pack-prices-rise-for-first-time-to-an-average-of-151-kwh/.

[8] Diouf, Boucar and Pode, Ramchandra. «Potential of lithium-ion batteries in renewable energy». In: *Renewable Energy* 76 (2015), pp. 375–380. ISSN: 0960-1481. DOI: https://doi.org/10.1016/j.renene.2014.11.058.

[9]   Wieboldt, Dick, Hahn, Matthias, and Ruff, Ines. «Techniques for Raman Analysis of Lithium-Ion Batteries». In: (2015). URL: www.spectroscopyonline.com/view/techniques-raman-analysis-lithium-ion-batteries.

[10] Tarascon, J.M. and Armand, Michel. «Issues and Challenges Facing Rechargeable Lithium Batteries». In: *Nature* 414 (2001), pp. 359–67. DOI: 10.1038/35104644.

[11] *BU-205: Types of Lithium-ion.* [Online; accessed 5-December-2022]. Oct. 2021. URL: https://batteryuniversity.com/article/bu-205-types-of-lithium-ion.

[12] Iskandar Radzi, Z. et al. «Review of spinel LiMn2O4 cathode materials under high cut-off voltage in lithium-ion batteries: Challenges and strategies». In: *Journal of Electroanalytical Chemistry* 920 (2022), p. 116623. ISSN: 1572-6657. DOI: https://doi.org/10.1016/j.jelechem.2022.116623.

[13] Porzio, Jason and Scown, Corinne D. «Life-Cycle Assessment Considerations for Batteries and Battery Materials». In: *Advanced Energy Materials* 11.33 (2021), p. 2100771. DOI: https://doi.org/10.1002/aenm.202100771. eprint: https://onlinelibrary.wiley.com/doi/pdf/10.1002/aenm.202100771.

[14] Nitta, Naoki et al. «Li-ion battery materials: present and future». In: *Materials Today* 18.5 (2015), pp. 252–264. ISSN: 1369-7021. DOI: https://doi.org/10.1016/j.mattod.2014.10.040.

[15] Liu, Yi-Hung and Tsai, Tsung-Yu. «Improving electrochemical performance of lithium ion batteries using a binder-free carbon fiber-based LiNi0.5(1-x)Mn1.5(1-x/3)CrxO4 cathode with a conventional electrolyte». In: *Journal of Power Sources* 484 (2021), p. 229262. ISSN: 0378-7753. DOI: https://doi.org/10.1016/j.jpowsour.2020.229262.

[16] SAT. *Battery Material - Binder.* [Online; accessed 8-january-2023]. URL: http://sateng.co.kr/en/business/battery.php.

[17] Nzereogu, P.U. et al. «Anode materials for lithium-ion batteries: A review». In: *Applied Surface Science Advances* 9 (2022), p. 100233. ISSN: 2666-5239. DOI: 10.1016/j.apsadv.2022.100233.

[18] Wang, Renheng et al. «Lithium metal anodes: Present and future». In: *Journal of Energy Chemistry* 48 (2020), pp. 145–159. ISSN: 2095-4956. DOI: https://doi.org/10.1016/j.jechem.2019.12.024.

[19] Mahmud, Saifullah et al. «Recent advances in lithium-ion battery materials for improved electrochemical performance: A review». In: *Results in Engineering* 15 (2022), p. 100472. ISSN: 2590-1230. DOI: https://doi.org/10.1016/j.rineng.2022.100472.

[20] Hassoun, Jusef and Scrosati, Bruno. «Review—Advances in Anode and Electrolyte Materials for the Progress of Lithium-Ion and beyond Lithium-Ion Batteries». In: *Journal of The Electrochemical Society* 162.14 (2015), A2582. DOI: 10.1149/2.0191514jes.

[21] Varzi, Alberto et al. «Challenges and prospects of the role of solid electrolytes in the revitalization of lithium metal batteries». In: *Journal of Materials Chemistry A* 4.44 (2016), pp. 17251–17259. DOI: https://doi.org/10.1039/C6TA07384K.

[22] Hartnig, Christoph and Schmidt, Michael. «Electrolytes and conducting salts». In: *Lithium-Ion Batteries: Basics and Applications*. Ed. by Reiner Korthauer. Berlin, Heidelberg: Springer Berlin Heidelberg, 2018, pp. 59–74. ISBN: 978-3-662-53071-9. DOI: 10.1007/978-3-662-53071-9_6.

[23] Baskoro, Febri, Wong, Hui Qi, and Yen, Hung-Ju. «Strategic Structural Design of a Gel Polymer Electrolyte toward a High Efficiency Lithium-Ion Battery». In: *ACS Applied Energy Materials* 2.6 (2019), pp. 3937–3971. DOI: 10.1021/acsaem.9b00295.

[24] Duan, Jian et al. «Building Safe Lithium-Ion Batteries for Electric Vehicles: A Review». In: *Electrochemical Energy Reviews* 3 (Dec. 2019). DOI: 10.1007/s41918-019-00060-4.

[25] Zhang, Shichao, Li, Siyuan, and Lu, Yingying. «Designing safer lithium-based batteries with nonflammable electrolytes: A review». In: *eScience* 1.2 (2021), pp. 163–177. ISSN: 2667-1417. DOI: https://doi.org/10.1016/j.esci.2021.12.003.

[26] Quartarone, Eliana and Mustarelli, Piercarlo. «Electrolytes for solid-state lithium rechargeable batteries: recent advances and perspectives». In: *Chem. Soc. Rev.* 40 (5 2011), pp. 2525–2540. DOI: 10.1039/C0CS00081G.

[27] Wang, Zhe et al. «Ionic Liquids as "Green Solvent and/or Electrolyte" for Energy Interface». In: *Engineered Science* 11 (2020), pp. 3–18. ISSN: 2576-9898. DOI: 10.30919/es8d0013.

[28] Weber, Christoph J. and Roth, Michael. «Separators». In: *Lithium-Ion Batteries: Basics and Applications*. Ed. by Reiner Korthauer. Berlin, Heidelberg: Springer Berlin Heidelberg, 2018, pp. 75–88. ISBN: 978-3-662-53071-9. DOI: 10.1007/978-3-662-53071-9_7.

[29] Lee, Hun et al. «A review of recent developments in membrane separators for rechargeable lithium-ion batteries». In: *Energy Environ. Sci.* 7 (12 2014), pp. 3857–3886. DOI: 10.1039/C4EE01432D.

[30] Zhang, Xingyi et al. «Recent progress in flame-retardant separators for safe lithium-ion batteries». In: *Energy Storage Materials* 37 (2021), pp. 628–647. ISSN: 2405-8297. DOI: https://doi.org/10.1016/j.ensm.2021.02.042.

[31] Woehrle, Thomas. «Lithium-ion cell». In: *Lithium-Ion Batteries: Basics and Applications*. Ed. by Reiner Korthauer. Berlin, Heidelberg: Springer Berlin Heidelberg, 2018. Chap. 9, pp. 101–111. ISBN: 978-3-662-53071-9. DOI: `10.1007/978-3-662-53071-9_9`.

[32] Zhu, Feng et al. «Failure behavior of prismatic Li-ion battery cells under abuse loading condition - A combined experimental and computational study». In: *Journal of Energy Storage* 48 (2022), p. 103969. ISSN: 2352-152X. DOI: `https://doi.org/10.1016/j.est.2022.103969`.

[33] *BU-301a: Types of Battery Cells*. [Online; accessed 2-February-2023]. Apr. 2019. URL: `https://batteryuniversity.com/article/bu-205-types-of-lithium-ion`.

[34] Waldmann, Thomas et al. «18650 vs. 21700 Li-ion cells – A direct comparison of electrochemical, thermal, and geometrical properties». In: *Journal of Power Sources* 472 (2020), p. 228614. ISSN: 0378-7753. DOI: `https://doi.org/10.1016/j.jpowsour.2020.228614`.

[35] Mikolajczak, Celina et al. *Lithium-ion batteries hazard and use assessment*. Springer Science, 2012. DOI: `https://doi.org/10.1007/978-1-4614-3486-3`.

[36] Bubbico, Roberto, Greco, Viviana, and Menale, Carla. «Hazardous scenarios identification for Li-ion secondary batteries». In: *Safety Science* 108 (2018), pp. 72–88. ISSN: 0925-7535. DOI: `https://doi.org/10.1016/j.ssci.2018.04.024`.

[37] Chen, Yuqing et al. «A review of lithium-ion battery safety concerns: The issues, strategies, and testing standards». In: *Journal of Energy Chemistry* 59 (2021), pp. 83–99. ISSN: 2095-4956. DOI: `https://doi.org/10.1016/j.jechem.2020.10.017`.

[38] Chombo, Pius Victor and Laoonual, Yossapong. «A review of safety strategies of a Li-ion battery». In: *Journal of Power Sources* 478 (2020), p. 228649. ISSN: 0378-7753. DOI: `https://doi.org/10.1016/j.jpowsour.2020.228649`.

[39] Feng, Xuning et al. «Thermal runaway mechanism of lithium ion battery for electric vehicles: A review». In: *Energy Storage Materials* 10 (2018), pp. 246–267. ISSN: 2405-8297. DOI: `https://doi.org/10.1016/j.ensm.2017.05.013`.

[40] Baird, Austin R. et al. «Explosion hazards from lithium-ion battery vent gas». In: *Journal of Power Sources* 446 (2020), p. 227257. ISSN: 0378-7753. DOI: `https://doi.org/10.1016/j.jpowsour.2019.227257`.

[41] Königseder, Alexander. «Investigation of the Thermal Runaway in Lithium Ion batteries». MA thesis. Technischen Universität Graz, Mar. 2017.

[42] Held, Marcel et al. «Thermal runaway and fire of electric vehicle lithium-ion battery and contamination of infrastructure facility». In: *Renewable and Sustainable Energy Reviews* 165 (2022), p. 112474. ISSN: 1364-0321. DOI: https://doi.org/10.1016/j.rser.2022.112474.

[43] Sturm, Peter et al. «Fire tests with lithium-ion battery electric vehicles in road tunnels». In: *Fire Safety Journal* 134 (2022), p. 103695. ISSN: 0379-7112. DOI: https://doi.org/10.1016/j.firesaf.2022.103695.

[44] Mellert, L. et al. *Risk minimisation of electric vehicle fires in underground traffic infrastructures.* Tech. rep. Research project AGT 2018/006 petitioned by the Tunnel Research Work-ing Group (Arbeitsgruppe Tunnelforschung, AGT). Schweizerischer Verband der Strassen- und Verkehrsfachleute (VSS), 2020.

[45] Mellert, Lars Derek et al. «Electric mobility and road tunnel safety – Hazards of electric vehicle fires». In: 2018.

[46] Yao, Xingyan, Kong, Lingxi, and Pecht, Michael. «Reliability of Cylindrical Li-ion Battery Safety Vents». In: *IEEE Access* PP (May 2020), pp. 1–1. DOI: 10.1109/ACCESS.2020.2997792.

[47] Huang, Zonghou et al. «Thermal Runaway Behavior of Lithium Iron Phosphate Battery During Penetration». In: *Fire Technology* 56 (Feb. 2020). DOI: 10.1007/s10694-020-00967-1.

[48] Mao, Binbin et al. «Failure mechanism of the lithium ion battery during nail penetration». In: *International Journal of Heat and Mass Transfer* 122 (2018), pp. 1103–1115. ISSN: 0017-9310. DOI: https://doi.org/10.1016/j.ijheatmasstransfer.2018.02.036.

[49] Perea, Alexis et al. «State of charge influence on thermal reactions and abuse tests in commercial lithium-ion cells». In: *Journal of Power Sources* 399 (Sept. 2018), pp. 392–397. DOI: 10.1016/j.jpowsour.2018.07.112.

[50] Wang, Jionggeng et al. «Investigation of the thermal performance in lithium-ion cells during polyformaldehyde nail penetration». In: *Journal of Thermal Analysis and Calorimetry* 145 (June 2020). DOI: 10.1007/s10973-020-09853-y.

[51] Santhanagopalan, Shriram, Ramadass, Premanand, and Zhang, John (Zhengming). «Analysis of internal short-circuit in a lithium ion cell». In: *Journal of Power Sources* 194.1 (2009). XIth Polish Conference on Fast Ionic Conductors 2008, pp. 550–557. ISSN: 0378-7753. DOI: https://doi.org/10.1016/j.jpowsour.2009.05.002.

[52] Xu, Jun, Wu, Yijing, and Yin, Sha. «Investigation of effects of design parameters on the internal short-circuit in cylindrical lithium-ion batteries». In: *RSC Adv.* 7 (24 2017), pp. 14360–14371. DOI: 10.1039/C6RA27892B.

[53] Zhang, Guangxu et al. «Internal short circuit mechanisms, experimental approaches and detection methods of lithium-ion batteries for electric vehicles: A review». In: *Renewable and Sustainable Energy Reviews* 141 (2021), p. 110790. ISSN: 1364-0321. DOI: https://doi.org/10.1016/j.rser.2021.110790.

[54] Zhang, Zhengming John, Ramadass, Premanand, and Fang, Weifeng. «18 - Safety of Lithium-Ion Batteries». In: *Lithium-Ion Batteries*. Ed. by Gianfranco Pistoia. Amsterdam: Elsevier, 2014, pp. 409–435. ISBN: 978-0-444-59513-3. DOI: https://doi.org/10.1016/B978-0-444-59513-3.00018-2.

[55] Liu, Binghe et al. «Safety issues and mechanisms of lithium-ion battery cell upon mechanical abusive loading: A review». In: *Energy Storage Materials* 24 (2020), pp. 85–112. ISSN: 2405-8297. DOI: https://doi.org/10.1016/j.ensm.2019.06.036.

[56] Howey, David et al. «Free Radicals: Making a Case for Battery Modeling». In: *Electrochemical Society Interface* 29 (Dec. 2020), p. 30. DOI: 10.1149/2.F03204IF.

[57] F, Brosa Panella et al. «A continuum of physics-based lithium-ion battery models reviewed». In: *Progress in Energy* 4.4 (July 2022), p. 042003. DOI: 10.1088/2516-1083/ac7d31.

[58] Vyroubal, Petr and Kazda, Tomáš. «Finite element model of nail penetration into lithium ion battery». In: *Journal of Energy Storage* 20 (2018), pp. 451–458. ISSN: 2352-152X. DOI: https://doi.org/10.1016/j.est.2018.10.008.

[59] Abada, S. et al. «Safety focused modeling of lithium-ion batteries: A review». In: *Journal of Power Sources* 306 (2016), pp. 178–192. ISSN: 0378-7753. DOI: https://doi.org/10.1016/j.jpowsour.2015.11.100.

[60] Prett, Gregory L. «Battery management systems, Volume I: Battery modeling». In: Artech House, 2015.

[61] Sacchetti, Luigi. «Electrochemical-thermal Analysis of High Capacity Li-ion Pouch Cell for Automotive Applications». MA thesis. Politecnico di Torino, Oct. 2020.

[62] Jokar, Ali et al. «Review of simplified Pseudo-two-Dimensional models of lithium-ion batteries». In: *Journal of Power Sources* 327 (2016), pp. 44–55. ISSN: 0378-7753. DOI: https://doi.org/10.1016/j.jpowsour.2016.07.036.

[63] Wang, Kai et al. «State of Charge (SOC) Estimation of Lithium-ion Battery Based on Adaptive Square Root Unscented Kalman Filter». In: *International Journal of Electrochemical Science* 15 (Jan. 2020), pp. 9499–9516.

[64] Almeida, Gabriel, Souza, Antonio, and Ribeiro, Paulo. «A Neural Network Application for a Lithium-Ion Battery Pack State-of-Charge Estimator with Enhanced Accuracy». In: *Proceedings* 58 (Sept. 2020). DOI: `10.3390/WEF-06915`.

[65] Attanayaka, Shehani, Karunadasa, J.P., and Hemapala, K T M U. «Estimation of state of charge for lithium-ion batteries - A Review». In: *AIMS Energy* 7 (Apr. 2019), pp. 186–210. DOI: `10.3934/energy.2019.2.186`.

[66] Wetton, Rachel Han; Colin Macdonald; Brian. «A fast solver for the pseudo-two-dimensional model of lithium-ion batteries». PhD thesis. University of British Columbia, 2021. DOI: `http://dx.doi.org/10.14288/1.0401885`.

[67] Fuller, Thomas F., Doyle, Marc, and Newman, John. «Simulation and Optimization of the Dual Lithium Ion Insertion Cell». In: *Journal of The Electrochemical Society* 141.1 (Jan. 1994), p. 1. DOI: `10.1149/1.2054684`.

[68] Ramadesigan, Venkatasailanathan et al. «Modeling and Simulation of Lithium-Ion Batteries from a Systems Engineering Perspective». In: *Journal of The Electrochemical Society* 159.3 (Jan. 2012), R31. DOI: `10.1149/2.018203jes`.

[69] Liu, Binghe, Yin, Sha, and Xu, Jun. «Integrated computation model of lithium-ion battery subject to nail penetration». In: *Applied Energy* 183 (2016), pp. 278–289. ISSN: 0306-2619. DOI: `https://doi.org/10.1016/j.apenergy.2016.08.101`.

[70] Morgan, Lucy M et al. «Pushing the boundaries of lithium battery research with atomistic modelling on different scales». In: *Progress in Energy* 4.1 (Dec. 2021), p. 012002. DOI: `10.1088/2516-1083/ac3894`.

[71] Gavilán-Arriazu, Edgardo et al. «Kinetic Monte Carlo simulations applied to Li-ion and post Li-ion batteries: a key link in the multi-scale chain». In: *Progress in Energy* 3 (Aug. 2021). DOI: `10.1088/2516-1083/ac1a65`.

[72] Chen, Chang-Hui et al. «Development of Experimental Techniques for Parameterization of Multi-scale Lithium-ion Battery Models». In: *Journal of the Electrochemical Society* 167 (May 2020). DOI: `10.1149/1945-7111/ab9050`.

[73] Falconi, Andrea. «Electrochemical Li-Ion battery modeling for electricvehicles». PhD thesis. COMMUNAUTE UNIVERSITE GRENOBLE ALPES, 2017. DOI: `https://hal.science/tel-01676976`.

[74] Xu, Le et al. «Enabling high-fidelity electrochemical P2D modeling of lithium-ion batteries via fast and non-destructive parameter identification». In: *Energy Storage Materials* 45 (2022), pp. 952–968. ISSN: 2405-8297. DOI: `https://doi.org/10.1016/j.ensm.2021.12.044`.

[75] Park, Saehong et al. «Optimal Experimental Design for Parameterization of an Electrochemical Lithium-Ion Battery Model». In: *Journal of The Electrochemical Society* 165 (Jan. 2018), A1309–A1323. DOI: `10.1149/2.0421807jes`.

[76] Rajabloo, Barzin et al. «An Inverse Method for Estimating the Electrochemical Parameters of Lithium-Ion Batteries». In: *Journal of The Electrochemical Society* 163.14 (Oct. 2016), A2876. DOI: `10.1149/2.0191614jes`.

[77] Kim, Minho et al. «Data-efficient parameter identification of electrochemical lithium-ion battery model using deep Bayesian harmony search». In: *Applied Energy* 254 (2019), p. 113644. ISSN: 0306-2619. DOI: `https://doi.org/10.1016/j.apenergy.2019.113644`.

[78] Chun, Huiyong et al. «Real-Time Parameter Estimation of an Electrochemical Lithium-Ion Battery Model Using a Long Short-Term Memory Network». In: *IEEE Access* 8 (2020), pp. 81789–81799. DOI: `10.1109/ACCESS.2020.2991124`.

[79] Laue, Vincent, Röder, Fridolin, and Krewer, Ulrike. «Practical identifiability of electrochemical P2D models for lithium-ion batteries». In: *Journal of Applied Electrochemistry* 51 (Sept. 2021). DOI: `10.1007/s10800-021-01579-5`.

[80] Vazquez-Arenas, Jorge et al. «A rapid estimation and sensitivity analysis of parameters describing the behavior of commercial Li-ion batteries including thermal analysis». In: *Energy Conversion and Management* 87 (2014), pp. 472–482. ISSN: 0196-8904. DOI: `https://doi.org/10.1016/j.enconman.2014.06.076`.

[81] Masoudi, Ramin, Uchida, Thomas, and McPhee, John. «Parameter estimation of an electrochemistry-based lithium-ion battery model». In: *Journal of Power Sources* 291 (2015), pp. 215–224. ISSN: 0378-7753. DOI: `https://doi.org/10.1016/j.jpowsour.2015.04.154`.

[82] Jin, Ning et al. «Parameter estimation of an electrochemistry-based lithium-ion battery model using a two-step procedure and a parameter sensitivity analysis». In: *International Journal of Energy Research* 42.7 (2018), pp. 2417–2430. DOI: `https://doi.org/10.1002/er.4022`. eprint: `https://onlinelibrary.wiley.com/doi/pdf/10.1002/er.4022`.

[83] Li, Weihan et al. «Data-driven systematic parameter identification of an electrochemical model for lithium-ion batteries with artificial intelligence». In: *Energy Storage Materials* 44 (2022), pp. 557–570. ISSN: 2405-8297. DOI: `https://doi.org/10.1016/j.ensm.2021.10.023`.

[84] SamsungSdi. *Small-Sized Li-ion Battery Business*. [Online; accessed 4-January-2023]. URL: `https://www.samsungsdi.com/lithium-ion-battery/index.html`.

[85] *Material Safety Data Sheet (IcR18650-26H)*. Tech. rep. Samsung SDI, 2015.

[86] *Material Safety Data Sheet (INR18650-29E)*. Tech. rep. Samsung SDI, 2015.

[87] THT. *ARC- Accelerating Rate Calorimeter*. URL: https://www.thermalhazardtechnology.com/contentfiles/downloads/38.pdf.

[88] Melcher, Andreas et al. «Modeling and Simulation the Thermal Runaway Behavior of Cylindrical Li-Ion Cells—Computing of Critical Parameter». In: *Energies* 9 (Apr. 2016), p. 292. DOI: 10.3390/en9040292.

[89] Spotnitz, R. and Franklin, J. «Abuse behavior of high-power, lithium-ion cells». In: *Journal of Power Sources* 113.1 (2003), pp. 81–100. ISSN: 0378-7753. DOI: https://doi.org/10.1016/S0378-7753(02)00488-3.

[90] Kim, Gi-Heon, Pesaran, Ahmad, and Spotnitz, Robert. «A three-dimensional thermal abuse model for lithium-ion cells». In: *Journal of Power Sources* 170.2 (2007), pp. 476–489. ISSN: 0378-7753. DOI: https://doi.org/10.1016/j.jpowsour.2007.04.018.

[91] Md Said, Mohamad Syazarudin and Mohd Tohir, Mohd Zahirasri. «Prediction of Lithium-ion Battery Thermal Runaway Propagation for Large Scale Applications Fire Hazard Quantification». In: *Processes* 7.10 (2019). ISSN: 2227-9717. DOI: 10.3390/pr7100703.

[92] Chiu, Kuan-Cheng et al. «An electrochemical modeling of lithium-ion battery nail penetration». In: *Journal of Power Sources* 251 (2014), pp. 254–263. ISSN: 0378-7753. DOI: https://doi.org/10.1016/j.jpowsour.2013.11.069.

[93] Shelke, Ashish V. et al. «Characterizing and predicting 21700 NMC lithium-ion battery thermal runaway induced by nail penetration». In: *Applied Thermal Engineering* 209 (2022), p. 118278. ISSN: 1359-4311. DOI: https://doi.org/10.1016/j.applthermaleng.2022.118278.

[94] Park, Sun Ho et al. «A microcrack propagation-based life prediction model for lithium-ion batteries with Ni-rich cathode materials». In: *Journal of Energy Storage* 58 (2023), p. 106420. ISSN: 2352-152X. DOI: https://doi.org/10.1016/j.est.2022.106420.

[95] Wang, Jionggeng et al. «Experimental and numerical study on penetration-induced internal short-circuit of lithium-ion cell». In: *Applied Thermal Engineering* 171 (2020), p. 115082. ISSN: 1359-4311. DOI: https://doi.org/10.1016/j.applthermaleng.2020.115082.

[96] Zhao, Wei, Luo, Gang, and Wang, Chao-Yang. «Modeling Nail Penetration Process in Large-Format Li-Ion Cells». In: *Journal of the Electrochemical Society* 162 (Jan. 2015), A207–A217. DOI: 10.1149/2.1071501jes.

[97] Maheshwari, A. «Modelling, aging and optimal operation of lithium-ion batteries». PhD thesis. Technische Universiteit Eindhoven, 2018.

[98] Dickinson, Edmund. «How to Model Short Circuits in Lithium-Ion Batteries». In: *COMSOL Blog* (2016).

[99] Wu, Wei, Xiao, Xinran, and Huang, Xiaosong. «The effect of battery design parameters on heat generation and utilization in a Li-ion cell». In: *Electrochimica Acta* 83 (2012), pp. 227–240. ISSN: 0013-4686. DOI: https://doi.org/10.1016/j.electacta.2012.07.081.

[100] Zhao, Rui, Liu, Jie, and Gu, Junjie. «A comprehensive study on Li-ion battery nail penetrations and the possible solutions». In: *Energy* 123 (2017), pp. 392–401. ISSN: 0360-5442. DOI: https://doi.org/10.1016/j.energy.2017.02.017.

[101] Cianciullo, Martina et al. «Simulation of the Thermal Runaway Onset in Li-Ion Cells - Influence of Cathode Materials and Operating Conditions». In: *Energies* 15.11 (2022). ISSN: 1996-1073. DOI: 10.3390/en15114169.

[102] Shi, Danghe et al. «Modeling stresses in the separator of a pouch lithium-ion cell». In: *Journal of Power Sources* 196.19 (2011), pp. 8129–8139. ISSN: 0378-7753. DOI: https://doi.org/10.1016/j.jpowsour.2011.05.026.

[103] *AISI Type 316 Stainless Steel, annealed sheet.* ASM Specification Aerospace Metals. [Online; accessed 9-March-2023]. URL: https://asm.matweb.com/search/SpecificMaterial.asp?bassnum=mq316a.

[104] Peng, Peng and Jiang, Fangming. «Thermal safety of lithium-ion batteries with various cathode materials: A numerical study». In: *International Journal of Heat and Mass Transfer* 103 (2016), pp. 1008–1016. ISSN: 0017-9310. DOI: https://doi.org/10.1016/j.ijheatmasstransfer.2016.07.088.

[105] Kong, Depeng et al. «Numerical investigation of thermal runaway behavior of lithium-ion batteries with different battery materials and heating conditions». In: *Applied Thermal Engineering* 189 (2021), p. 116661. ISSN: 1359-4311. DOI: https://doi.org/10.1016/j.applthermaleng.2021.116661.

[106] Lopez, Carlos F., Jeevarajan, Judith A., and Mukherjee, Partha P. «Characterization of Lithium-Ion Battery Thermal Abuse Behavior Using Experimental and Computational Analysis». In: *Journal of The Electrochemical Society* 162.10 (Aug. 2015), A2163. DOI: 10.1149/2.0751510jes.

[107] COMSOL AB. *Comsol Multiphysycs Reference Manual.* URL: https://doc.comsol.com/6.0/doc/com.comsol.help.comsol/COMSOL_ReferenceManual.pdf.

[108] Benito van der Zander, Jan Sundermeyer, Daniel Braun, Tim Hoffmann. *TeXstudio - an integrated writing environment for creating LaTeX documents.* Version 4.5.2. 2022. URL: https://www.texstudio.org/.

[109] JabRef Development Team. *JabRef — An open-source, cross-platform citation and reference management software.* Version 5.3. 2021. URL: https://www.jabref.org/.

[110]   COMSOL AB. *COMSOL Multiphysics®*. Version 6.0. 2022. URL: www.comsol. com.